CARBON NANOTUBES

AS

ELECTROMECHANICAL RESONATORS

SINGLE-ELECTRON TUNNELING, NONLINEARITY, AND HIGH-BANDWIDTH READOUT

CARBON NANOTUBES
AS
ELECTROMECHANICAL RESONATORS
SINGLE-ELECTRON TUNNELING, NONLINEARITY, AND HIGH-BANDWIDTH READOUT

Proefschrift

ter verkrijging van de graad van doctor
aan de Technische Universiteit Delft,
op gezag van de Rector Magnificus prof. ir. K. C. A. M. Luyben,
voorzitter van het College voor Promoties,
in het openbaar te verdedigen op woensdag 3 april 2013 om 12:30 uur

door

Harold Boudewijn MEERWALDT

natuurkundig doctorandus
geboren te Vlaardingen, Nederland.

Dit proefschrift is goedgekeurd door de promotor:

Prof. dr. ir. H. S. J. van der Zant

Samenstelling promotiecommissie:

Rector Magnificus,	voorzitter
Prof. dr. ir. H. S. J. van der Zant,	Technische Universiteit Delft, promotor
Dr. G. A. Steele,	Technische Universiteit Delft, copromotor
Prof. dr. Ya. M. Blanter,	Technische Universiteit Delft
Prof. dr. P. G. Steeneken,	NXP Semiconductors/Technische Universiteit Delft
Prof. dr. D. Iannuzzi,	Vrije Universiteit Amsterdam
Dr. M. M. Deshmukh,	Tata Institute of Fundamental Research, India
Prof. dr. E. M. Weig,	Universität Konstanz, Duitsland

Dr. G. A. Steele heeft als begeleider in belangrijke mate aan de totstandkoming van het proefschrift bijgedragen.

Keywords:	carbon nanotubes · nano-electromechanical systems (NEMS) · single-electron tunneling · nonlinearity · high-bandwidth readout
Printed by:	Proefschriftmaken.nl
Front & Back:	A Fender Sonoran semi-acoustic guitar. Photograph by Michele Buscema. Artwork by Harold Meerwaldt.

Casimir PhD Series, Delft-Leiden 2013-8

ISBN 978-90-8593-151-5

An electronic version of this dissertation is available at
http://repository.tudelft.nl/ and at www.narcis.nl.

The external links to all references and the internal links to chapters, (sub)sections, tables, and figures are all clickable in the electronic version.

CONTENTS

1

INTRODUCTION

Electromechanical systems transduce an electrical signal (a voltage or current) into a mechanical signal (a displacement) or vice versa. They can be found all around us. An example of an electromechanical system is an electric motor (Fig. 1.1a). Here, a magnetic field interacts with an electrical current and a force is induced between them. By varying either the magnetic field or the electric current, an oscillating force arises, which sets a rotor into motion. A turbine (Fig. 1.1b) uses the reverse transduction as the displacement of the blades is transduced into electricity.

The first person to find a qualitative relationship between electric charge and force was Charles-Augustin de Coulomb (1736-1806). Figure 1.1c shows the device he used, called a torsion balance, which consists of a horizontal insulating rod, suspended at its center by a thin, easily twistable wire and containing a charged metal sphere on one end and a counter weight at the other end. When he approached the metal sphere with another charged metal sphere, at a right angle to the rod, the spheres would repel or attract each other and he could read the resulting force from the angle over which the rod had rotated. Now known as Coulomb's Law, he found that the electrostatic force depends on the product of the charges on the spheres, $q_1 q_2$, and the inverse square of their distance, r:

$$F_{el} \propto \frac{q_1 q_2}{r^2}. \tag{1.1}$$

Parts of this Chapter have been published in "Fluctuating nonlinear oscillators" (Oxford University Press, 2012), ed. Mark Dykman [1].

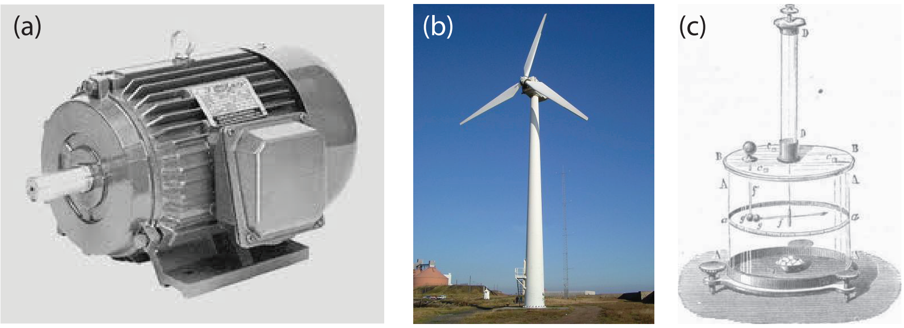

FIGURE 1.1: Macroscopic electromechanical systems: a) An electric motor, converting electricity into motion, b) a wind turbine, converting motion into electricity, and c) a torsion balance, measuring the electric force between two charged metal spheres from the angle of rotation.

Nano-electromechanical systems (NEMS) employ electromechanical forces, while having dimensions at the nanoscale. They can be fabricated top-down by applying dry or wet etch techniques to remove material and create a suspended structure, or bottom-up through processes such as chemical vapour deposition. Figure 1.2 shows that the different geometries of NEMS can be one-, two-, or three-dimensional; there are beams, strings, cantilevers, sheets, and drums. Looking for macroscopic equivalents for these geometries leads to bridges, guitar strings, diving boards, flat rubber bands, and trampolines respectively.

One of the most frequent uses of NEMS is as a resonator. A resonator displays an oscillating motion, but only when excited at a certain frequency, called the eigenfrequency or the resonance frequency. Figure 1.3 shows the different modes in which the resonance can take place, depending on the direction of the oscillation: flexural (bending) modes, longitudinal (stretching), radial (breathing) modes, and torsional (twisting) modes.

NEMS are studied for novel applications and for insights into fundamental phenomena. From an applied point of view, NEMS are very precise sensors of mass [6–10], charge [11], and displacement [12]. In a mass detection experiment, the resonance frequency, f_0, decreases, when a mass Δm attaches to the resonator with mass m, by Δf_0:

$$\Delta f_0 = -\frac{\Delta m}{2m} f_0. \tag{1.2}$$

Because of the small mass of the resonator, the shift in resonance frequency is large and can be readily detected. At this moment, a carbon nanotube acts as the ultimate low-mass resonator, with a mass resolution corresponding to a single proton [10].

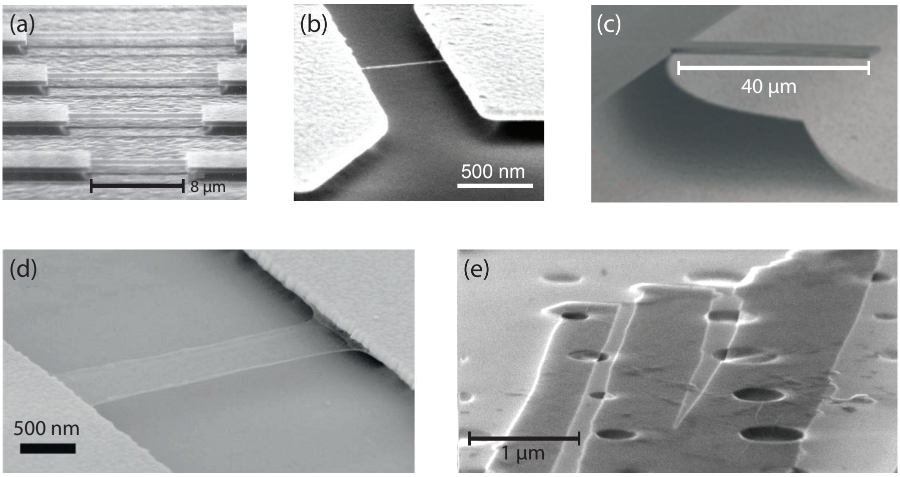

FIGURE 1.2: Different geometries of nano-electromechanical systems: a) A doubly-clamped SiC beam [2], b) a carbon nanotube [3], which can act as a beam or a string, c) a SiN cantilever [4], d) a graphene sheet [5], and e) few-layer graphene drums (image courtesy A. Castellanos-Gomez)

.

From a fundamental point of view, NEMS allow the investigation of quantum mechanical phenomena of a macroscopic object. As Schrödinger's Cat gedankenexperiment hinted at, quantum mechanics becomes counterintuitive when dealing with objects we consider macroscopic. A nanomechanical resonator allows experiments that better define the barrier between the quantum and the classical world, when an object of a considerable number of atoms is shown to possess quantum properties. In order to look at quantum effects, the first step to be taken is reaching the quantum ground state of the resonator. From statistical mechanics,

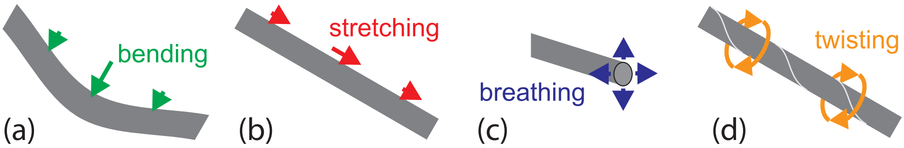

FIGURE 1.3: Different modes of vibration: a) bending, b) stretching, c) breathing, and d) twisting modes (image adapted from [3]).

the potential energy of a harmonic oscillator at temperature T is found to be:

$$\frac{1}{2} m\omega_0^2 \langle u^2 \rangle = \frac{\hbar\omega_0}{2}\left(\frac{1}{2} + \frac{1}{e^{\frac{\hbar\omega_0}{k_B T}} - 1}\right). \tag{1.3}$$

Here ω_0 is the angular resonance frequency, $\langle u^2 \rangle$ is the mean-squared displacement, $\hbar$ is the reduced Planck's constant, and k_B is Boltzmann's constant. Thermal motion comes about from the temperature-driven Brownian motion of atoms. At temperatures where the thermal energy greatly exceeds the energy of a phonon ($\hbar\omega_0 \ll k_B T$), the root-mean-squared amplitude of a vibrational mode due to thermal motion is given by:

$$u_{th} = \sqrt{\frac{k_B T}{m\omega_0^2}}. \tag{1.4}$$

The zero-point motion is the motion due to quantum fluctuations, when the resonator is in its ground state with an energy of half a phonon. At temperatures where the energy of a phonon is much larger than the thermal energy ($\hbar\omega_0 \gg k_B T$), the root-mean-squared amplitude of the zero-point motion is given by:

$$u_{zpm} = \sqrt{\frac{\hbar}{2m\omega_0}}. \tag{1.5}$$

Several different methods have shown to achieve the quantum ground state experimentally. In the group of Andrew Cleland [13], a bulk dilatational resonator (Fig. 1.4a) reaches the quantum ground state through passive cryogenic cooling. By coupling it to a superconducting phase qubit, the exchange of a phonon of the

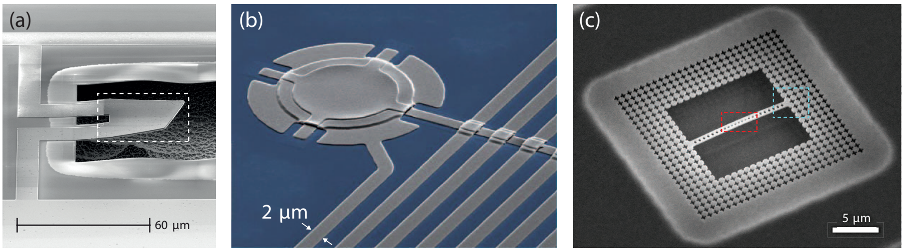

FIGURE 1.4: Geometries with which the quantum ground state of a mechanical resonator has been reached: a) A bulk dilatational resonator coupled to a superconducting phase qubit [13], b) an aluminium nanodrum in a superconducting LC electrical resonator [14], and c) a patterned silicon nanobeam, surrounded by an external phononic bandgap shield [15].

mechanical resonator into a photon of the qubit, and vice versa, has been demonstrated. In the group of Konrad Lehnert [14], an aluminium nanodrum, embedded into a superconducting LC electrical resonator, (Fig. 1.4b) reaches the quantum ground state through the use of sideband cooling. In the group of Oskar Painter [15], a patterned silicon nanobeam, surrounded by an external phononic bandgap shield, (Fig. 1.4c) is laser cooled into its quantum ground state.

1.1 THE DAMPED DRIVEN HARMONIC OSCILLATOR

The standard model to describe a resonator is the damped driven harmonic oscillator. The process of oscillation can be explained as follows. Oscillation occurs when a body is forced away from its rest or equilibrium position and a restoring force causes it to return to this position. The inertial force, $F_{inertial} = md^2u/dt^2$, causes the body to move past the equilibrium position, until the restoring force makes it move back again. This repeating sequence of moving towards and away from the equilibrium position is called oscillation. The oscillation is said to be harmonic when the restoring force is proportional to the displacement of the body as $F_{restoring} = -ku$, with $k = m\omega_0^2$ the spring constant.

Besides the inertial force and the restoring force, there are also forces acting on the resonator that dampen its motion. One of the most common damping mechanisms is through viscous damping, where the moving resonator loses energy as it pushes a gas or a liquid away to make room for itself. The damping force is described as a viscous force, $F_{damping} = -m(\omega_0/Q)du/dt$. The number of oscillations that a resonator can perform, while being damped, is reflected in the quality factor, Q:

$$Q = 2\pi \times \frac{\text{Energy stored}}{\text{Energy dissipated per cycle}}. \tag{1.6}$$

A resonator is said to be overdamped, when the damping is so strong that a single oscillation cannot be performed. It is critically damped when one oscillation can take place, and it is underdamped when more than one oscillation can take place. This corresponds to the following values for the quality factor, as illustrated in figure 1.5:

$$Q \begin{cases} < \frac{1}{2} & \text{overdamped} \\ = \frac{1}{2} & \text{critically damped}\,. \\ > \frac{1}{2} & \text{underdamped} \end{cases} \tag{1.7}$$

For underdamped systems, Q/π can be described as the number of oscillations it takes before the amplitude ($\propto e^{-\omega_0 t/2Q}$) is decreased by a factor of $1/e$. In general, NEMS are underdamped resonators, as they are fabricated from low-defect

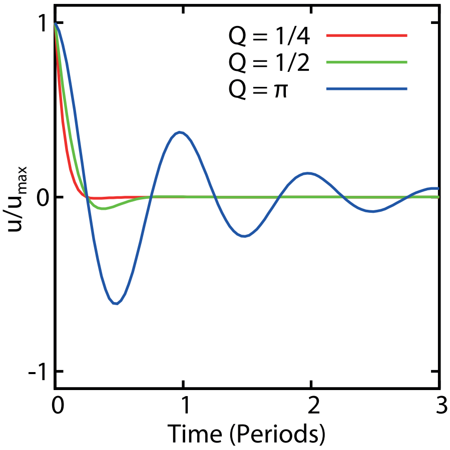

FIGURE 1.5: Oscillation of a mechanical resonator that is overdamped ($Q = 1/4$), critically damped ($Q = 1/2$), or underdamped ($Q = \pi$).

crystalline or bottom-up materials. To prevent the damping present from extinguishing the oscillation after a number of periods, an excitation or driving force can be applied to the resonator. This can be a coherent force, $F(t) = F_{ac}\cos(\omega_d t)$, at a drive frequency, ω_d, or a stochastic force due to thermal motion or (applied) noise. In electromechanical systems, a coherent driving force is often applied capacitively through an oscillating gate voltage that attracts and repels the charged electromechanical resonator.

The four forces acting on the resonator (the inertial force, the damping force, the restoring force, and the driving force) lead to the equation of motion for what is called the damped driven harmonic oscillator:

$$\frac{d^2u}{dt^2} + \frac{\omega_0}{Q}\frac{du}{dt} + \omega_0^2 u = \frac{F(t)}{m}. \tag{1.8}$$

For a coherent driving force, the amplitude, $u_{ac}(\omega_d)$, and the phase, $\phi(\omega_d)$, of the oscillation, $u(t) = u_{ac}(\omega_d)\cos(\omega_d t - \phi(\omega_d))$, at ω_d, are then given by:

$$u_{ac}(\omega_d) = \frac{F_{ac}/m}{\sqrt{\left(\omega_0^2 - \omega_d^2\right)^2 + \frac{\omega_0^2\omega_d^2}{Q^2}}}, \tag{1.9}$$

$$\phi(\omega_d) = \arctan\left(\frac{\omega_0\omega_d}{Q(\omega_0^2 - \omega_d^2)}\right). \tag{1.10}$$

The amplitude is maximum at the resonance frequency, ω_0, with a value of $u_{ac}^{max} = F_{ac}Q/k$, which summarizes the balance between the driving force, the damping force, and the restoring force. The full width at half maximum, ω_{FWHM}, of the resonance peak can be calculated to correspond to the quality factor as $Q = \omega_0/\omega_{FWHM}$. The phase of the resonator with respect to the drive shows a shift of 180 degrees around the resonance frequency, meaning that above the resonance frequency the resonator is lagging, being unable to keep up with the drive.

In Chapter 6 of this Thesis, nonlinear restoring forces will be discussed. When the amplitude of motion becomes large, Hooke's law, which states that the restoring force is proportional to the displacement, breaks down. The simplest model describing nonlinear restoring forces is the Duffing model, which uses a restoring force that depends on the displacement cubed. The equation of motion then reads:

$$\frac{d^2u}{dt^2} + \frac{\omega_0}{Q}\frac{du}{dt} + \omega_0^2 u + \alpha u^3 = \frac{F(t)}{m}, \tag{1.11}$$

where α is the nonlinear Duffing parameter with units of $\mathrm{Hz}^2/\mathrm{m}^2$. Solving this equation leads to implicit functions for the amplitude and the phase of the resonator:

$$u_{ac}(\omega_d) = \frac{F_{ac}/m}{\sqrt{\left(\omega_0^2 + \frac{3}{4}\alpha\,(u_{ac}(\omega_d))^2 - \omega_d^2\right)^2 + \frac{\omega_0^2\omega_d^2}{Q^2}}}, \tag{1.12}$$

$$\phi(\omega_d) = \arctan\left(\frac{\omega_0\omega_d}{Q(\omega_0^2 + \frac{3}{4}\alpha\,(u_{ac}(\omega_d))^2 - \omega_d^2)}\right). \tag{1.13}$$

Figure 1.6 illustrates the nonlinear amplitude and phase response of a damped driven harmonic oscillator. At low drive power, this results in an amplitude response with increased amplitude around the resonance frequency, just as the linear damped driven harmonic oscillator. At higher drive powers however, the resonance peak starts to tilt towards higher or lower frequencies, depending on the sign of the cubic Duffing parameter α. Now, at certain frequencies, there are three solutions to the equation of motion. While the solution with intermediate amplitude is unstable, the resonator can now stably oscillate with two different amplitudes, making it bistable. The amplitude response exhibits hysteresis; depending on the direction the drive frequency is changed, the resonator ends up in either the high or the low amplitude state. The phase response goes from 0 to 180 degrees as the drive frequency succeeds the resonance frequency and also exhibits bistability and hysteresis at high drive powers.

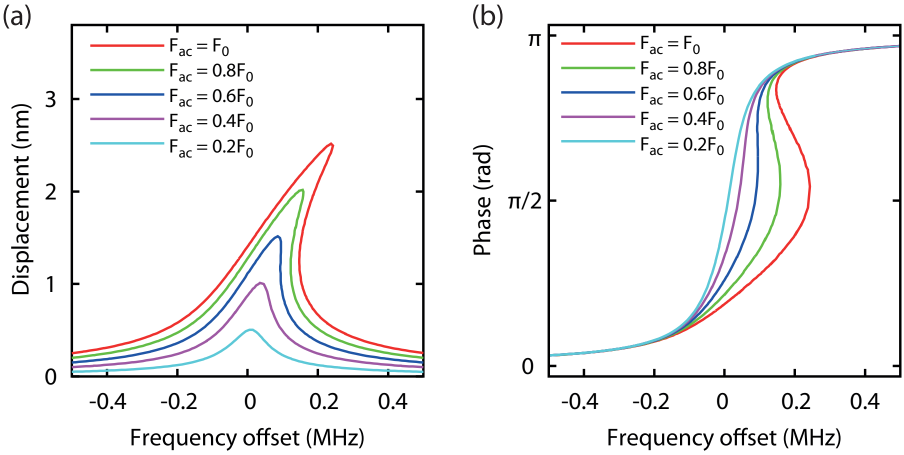

FIGURE 1.6: Amplitude and phase response of a mechanical resonator for increasing driving force, relative to an arbitrary F_0, showing a) an increased amplitude when the drive frequency matches the resonance frequency, where the maximum amplitude tilts to higher frequency at increased driving, giving rise to a bistable regime for certain frequencies ($\alpha > 0$), and b) a shift in the phase between the drive and the oscillation of 180 degrees, also showing bistability at higher powers.

1.2 SINGLE-ELECTRON TUNNELING AND QUANTUM DOTS

In this Thesis, the electromechanical resonator is treated in the three-terminal layout, where the resonator acts as a charged island, weakly coupled to a source and drain electrode. Weakly coupled implies here that there are sufficiently high potential barriers between the island and the leads, so that electrons can only reach the island through the process of tunneling. The third, gate electrode is far enough from the island to prevent electrons from tunneling on, but close enough to change its electrostatic potential. Figure 1.7 illustrates the island that is investigated in this Thesis, a suspended CNT quantum dot, which is weakly coupled to the leads through tunnel junctions.

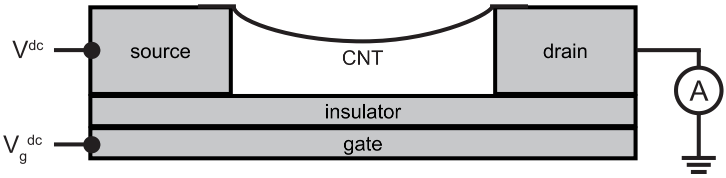

FIGURE 1.7: Three-terminal device with an island in the form of a suspended CNT quantum dot. Voltages are applied to the source and gate terminal. The current is measured at the drain terminal.

Whether an electron can tunnel between the source, island, and drain depends on the relative chemical potential between them. The chemical potential of the source and drain is determined by the Fermi energy of the metal and the applied bias voltage. The chemical potential of the island depends on several energies: the Fermi energy of the island, the electrostatic energy, the quantum mechanical confinement energy, and, for a suspended island, the elastic energy. The electrostatic energy, W_{est}, of an island is given by:

$$W_{est} = \frac{q^2}{2C_{tot}}\text{ , with } q = C_g V_g + C_s V_s + C_d V_d - eN, \tag{1.14}$$

where the charge, q, induced onto the island, depends on the number of electrons on the island, N, the capacitances, C_g, C_s, C_d, of the island to the gate, source, and drain, and the voltages, V_g, V_s, V_d, applied to the gate, source, and drain. The energy needed to add an extra electron to the island is given by twice the charging energy, E_c:

$$E_C = \frac{e^2}{2C_{tot}}, \tag{1.15}$$

where C_{tot} is the total capacitance of the island to the source, drain, and gate electrodes.

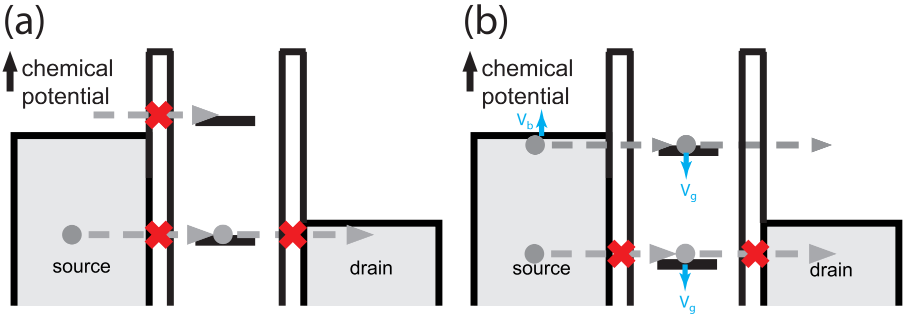

FIGURE 1.8: Energy diagrams showing the density of states (light grey) in the source, drain, and island, which are separated by potential barriers, at cryogenic temperatures for a nano-size island, resulting in a) Coulomb blockade, and b) single-electron tunneling.

Equation 1.15 shows that it does not take much energy to add an electron to islands with a large capacitance, but that it becomes an important factor for nanosized islands. At cryogenic temperatures with $k_B T \ll E_c$, the charging energy can no longer be supplied thermally (cf C_{tot} = 10 aF ∼ E_C = 8 meV, T = 1 K ∼ $k_B T$ = 90 μeV), and the island becomes a single-electron transistor. Also, as the islands become nano-sized, the quantum mechanical confinement energy starts to play a role. For a CNT, the confinement energy, ΔE, is giving by:

$$\Delta E = \frac{\hbar v_F}{2L}, \tag{1.16}$$

with $v_F = \sqrt{E_F/2m} = 8.1 \cdot 10^5$ m/s the Fermi velocity of an electron on a CNT (cf $L = 1\ \mu$m $\sim \Delta E = 1.7$ meV). When also the quantum mechanical confinement energy exceeds the thermal energy, $k_B T \ll \Delta E$, the island becomes a quantum dot. Figure 1.8 demonstrates the phenomena of Coulomb blockade and single-electron tunneling for a quantum dot, when there are respectively zero and one states on the quantum dot available for transport. In figure 1.9, the bias and gate voltage are varied, resulting in Coulomb diamonds (fig 1.9a, both bias and gate voltage), a Coulomb staircase (fig 1.9b, bias voltage only), and Coulomb peaks (fig 1.9c, gate voltage only). For simplicity, a quantum dot with non-degenerate states is displayed, where the addition energy for each electron consists of the charging energy and the confinement energy. For a CNT quantum dot with fourfold degeneracy, only the addition energy of each fourth electron contains the confinement energy, increasing the size of the corresponding Coulomb diamond.

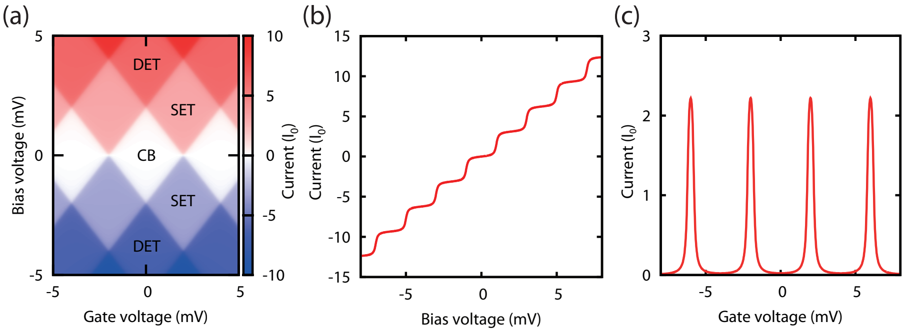

FIGURE 1.9: Transport through a quantum dot with non-degenerate states: a) Stability diagram, showing Coulomb diamonds with Coulomb blockade (CB), single-electron tunneling (SET), and double-electron tunneling (DET), b) Coulomb staircase at $V_g = 2$ mV, where the current increases in steps as another level enters the bias window, and c) Coulomb peaks at $V_b = 0.2$ mV, where the current increases as levels pass through the bias window.

The elastic energy [16], W_{ela}, for the flexural motion of a CNT depends on the bending rigidity, EI, and the tension, T, either residual (T_0) or resulting from elongation due to an applied gate voltage:

$$W_{ela}(u(z)) = \int_0^L \left\{ \frac{EI}{2}\left(u''(z)\right)^2 + \left(\frac{T_0}{2} + \frac{EA}{4L}\int_0^L \left(u'(z)\right)^2\right)\left(u'(z)\right)^2 \right\} dz. \tag{1.17}$$

Here, E is the Young's modulus; $I = \pi r^4/4$ is the second moment of area of a hollow cylinder, with r the radius; T_0 is the residual stress at $V_g = 0\,\mathrm{V}$; $A = \pi r^2$ is the cross-section; and $u(z)$ is the displacement of the CNT at a position z along the direction of the length with value L.

For a suspended CNT quantum dot, electronic-vibrational coupling (to be discussed in subsection 1.4.1) arises through two mechanisms. First, the elastic energy influences the chemical potential of the island and thereby causes vibrational excitations, which can be measured using tunnel spectroscopy. Secondly, in a suspended island, the gate capacitance depends on the distance of the island to the gate. Using a capacitive model of an infinite cylinder above a plate [17], the gate capacitance, $C_g = \int_0^L c_g(z)dz$, of a CNT depends on the position-dependent gate capacitance per unit length, $c_g(z)$, given by:

$$c_g(z) = \frac{2\pi\epsilon_0}{\operatorname{arccosh}(h_0/r)} + \frac{dc_g}{du}u(z)\text{ , with } \frac{dc_g}{du} = \frac{2\pi\epsilon_0}{h_0\operatorname{arccosh}(h_0/r)}. \tag{1.18}$$

The expression is given to first order in the limit of $u(z) \ll h_0$, with h_0 the distance between the CNT and the gate electrode. Both the electrostatic energy (through the displacement-dependent gate capacitance) and the elastic energy (through the chemical potential of the island) couple the charge and the displacement of the CNT, as their values are determined through the minimization of the total energy. For the modes of quantum dot mechanical resonators with a small resonance frequency, the contribution to the elastic energy becomes less relevant. For quantum dot mechanical resonators with a small value of dc_g/du, the contribution to the electrostatic energy becomes less relevant.

1.3 ELECTROMECHANICAL PROPERTIES OF CARBON NANOTUBES

A carbon nanotube is a remarkable material, which consists of only carbon atoms and can be thought of as a graphene sheet rolled up into a cylinder with the ends capped off with a buckyball sliced in half. This is called a single-walled CNT and, depending on how the graphene sheet is rolled up, CNTs are either semiconducting or metallic. At low temperatures, CNTs contacted by two electrodes become quantum dots, and Coulomb blockade and single-electron tunneling occurs. When more graphene sheets are wrapped up concentrically a multiwalled CNT is formed.

CNTs are fabricated using various methods. These include arc discharge [18], laser ablation [19], chemical vapor deposition (CVD) [20], and the use of high pressure carbon monoxide [21]. There are two ways to make doubly-clamped CNT resonators. The first method starts with growing CNTs on an oxidized silicon wafer and then underetching them with a trench so that they become suspended. This method exposes the CNT to resist, the electron beam, and acid, and may give rise to defects in and residues on the CNT. In the ultraclean method [22], processing on the CNT is avoided by first making the contacts and the trench and in the final step growing the CNTs. A suspended CNT resonator can be fabricated without defects, thus reducing damping which results in quality factors for the flexural modes above 100,000 [23].

The fact that a single-walled CNT is basically a hollow cylinder leads to a very low mass density. Starting with the two-dimensional density of graphene [24] of $\rho_{2D} = 7.7 \cdot 10^{-7}$ kg/m^2, a typical single-walled CNT with a radius of 1.5 nm has a mass density of ρ =1350 kg/m^3. This is considerably lower than top-down fabricated nano-electromechanical beams made for example of silicon (2330 kg/m^3), SiN [25] (2800 kg/m^3), or gold [26] (19300 kg/m^3). Combining the smaller mass density with the small dimensions results in a range of $10^{-22} - 10^{-20}$ kg for CNT resonators with lengths up to 2 μm. This is several orders smaller than the mass of a typical top-down fabricated nano- or microsized device [26], ranging $10^{-17} - 10^{-4}$ kg.

The Young's modulus, E, of a material is the ratio of the applied uniaxial stress to the resulting uniaxial strain and is a measure for the stiffness of a material. For a CNT, the Young's modulus of 1.3 TPa is high compared to silicon [26] (0.13 TPa), SiN [25] (0.16 TPa), and gold [26] (0.043 TPa). The small radius of a CNT leads to a small second moment of area, $I = \pi r^4/4$. However, the large Young's modulus still causes the bending rigidity, $D = EI$, of a CNT mechanical resonator to be large, preventing the CNT to behave as a chain. The resonance frequency of the fundamental bending mode of a CNT resonator under no tension can now be calculated using the bending rigidity:

$$f_0 = \frac{22.4}{2\pi L^2}\sqrt{\frac{EI}{\rho A}}. \tag{1.19}$$

By fabricating CNTs with a short length, the mechanical resonance frequency has been shown to reach 1.3 GHz [27] or 4.2 GHz [28] for the fundamental mode , and 39 GHz for a higher harmonic [29].

The aspect ratio of a CNT, L/r, can be of the order of hundreds or thousands. A macroscopic analogy of a 1 μm long CNT mechanical resonator, would be a ~10 m long fencing blade. Like a CNT, a fencing blade is stiff and is difficult to compress at its ends. Its large aspect ratio makes it difficult to remain completely straight, and any small force (gravity for the fencing blade, and van der Waals or capacitive forces for a CNT) will make it bend into a curved shape. Because of its bending rigidity, this is not the slack you would see in a hanging chain. It is often buckled, but whereas a large force is needed to move a doubly-clamped beam with a rectangular cross section out of the plane of buckling, a CNT could be made to swing with considerably less force because of its cross section with near-unity height-to-width ratio. The large aspect ratio allows the CNT to resonate with an amplitude that is larger than its radius, making nonlinear restoring forces appear readily (see also chapter 6)

Electrical, self-detecting readout schemes are based on the change in capacitance of the resonator to the gate electrode, as the resonator is set into motion. The low mass of the CNT combined with the large aspect ratio causes the CNT to have a large change in capacitance per unit mass with displacement, $(1/m)dC_g/du$. This means that only small ac voltages need to be applied to reach a sufficient capacitive force, $F_{ac} = (dC_g/du)V_g^{dc}V_g^{ac}$, to excite the CNT into large motion (cf $u_{ac}^{max} = (F_{ac}/m)(Q/\omega_0^2)$). This is useful in electrical readout schemes where the mechanical motion is read out at the drive frequency, and a low ac gate voltage results in less crosstalk obscuring the mechanical signal. Furthermore, because of a high dC_g/du, the mechanical motion results in a large change in the induced charge on the CNT, $\delta q_c = V_g(dC_g/du)\delta u$. Combined with a high value of dI/dq_c or d^2I/dq_c^2, this leads to a large change in the current flowing through the CNT due to mechanical motion.

A CNT is one of the strongest known materials; the maximum strain before plastic deformation occurs, has been found [30] to be at least 6% for a rope of CNTs, and the critical stress before the CNT tears has been determined [31] to be as high as 63 GPa for a multiwalled CNT. Similarly to the ac capacitive force mentioned previously, the high dC_g/du makes it possible to use a relatively low dc gate voltage and apply a significant dc capacitive force $F_{dc} = (1/2)(dC_g/du)\left(V_g^{dc}\right)^2$ to the CNT. Because of the large strength of the CNT, a large tension can be induced through gate voltage without breaking it. This combination makes the CNT one of a few materials with which it is possible to go from the so-called bending or beam-like regime, where the restoring force is dominated by the bending rigidity, to the tension or string-like regime, where the restoring force is dominated by the tension in the CNT. In the tension-dominated regime, the fundamental resonance frequency is dependent on gate voltage through the tension:

$$f_0(V_g) = \frac{1}{2L}\sqrt{\frac{T(V_g)}{\rho A}}. \tag{1.20}$$

1.4 PHYSICS OF CARBON NANOTUBE MECHANICAL RESONATORS

Many different phenomena have been observed in CNT mechanical resonators, because of their unique properties. In this section, we focus on the more fundamental phenomena, and leave out the studies of CNT resonators that are related more towards applications or determining its unique properties. The phenomena are discussed in three subsections: strong electron-vibron coupling, damping, and nonlinearity. The different detection methods used to observe these phenomena are described in detail in Chapter 2.

1.4.1 STRONG ELECTRON-VIBRON COUPLING

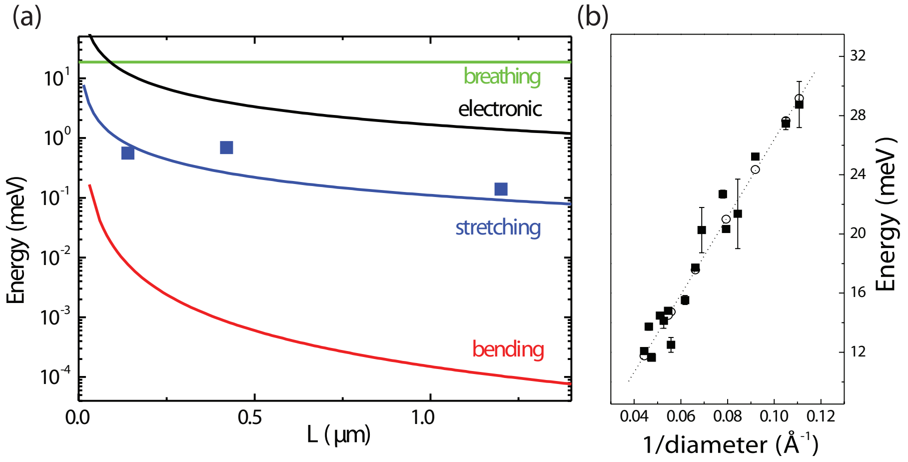

FIGURE 1.10: a) Comparison of the energies belonging to vibrational and electronic excitations with experimental data for stretching modes [3, 32]. b) Relation between vibrational energy and radius of a CNT, proving the vibrations to arise from breathing modes [33].

In CNT quantum dots, the mechanical motion is found to couple strongly to single-electron tunneling. The different modes of vibration can be distinguished by looking at their vibrational energies [32]. Figure 1.10a shows the dependence of the energy of the modes on the length of the CNT, where the radial (breathing) mode is the highest in energy and is independent of length (but proportional to $1/r$). The electronic excitation and the stretching mode are lower in energy, proportional to $1/L$, and the bending mode has a considerably lower energy, proportional to $1/L^2$. In radial and longitudinal modes, with their high energy (resonance frequency), the charge and the displacement are coupled through the chemical potential of the island due to the change in the elastic energy. In flexural (bending) modes, electron-vibron coupling mainly takes place through the displacement-dependent gate capacitance as it changes the electrostatic energy.

Radial modes were investigated [33, 34] using the STM spectroscopy measurement technique, through the measurement of the spectrum of a CNT at different positions along its axis. As visible in figure 1.10b, the relation between the phonon energy and the radius of the CNT confirms the phonon to arise from a radial mode. Because the direction of the tunneling electrons coincides with the direction of the radial motion, coupling takes place between the electrons and the radial modes.

Longitudinal (stretching) modes were investigated [32, 35, 36] using the three-terminal spectroscopy measurement technique. Coupling of longitudinal vibrational modes to electrons takes place through the Franck-Condon principle, where transitions between electronic states with a large overlap in their vibrational wavefunction are highly favoured. Figure 1.11a shows Franck-Condon blockade of current, which is clearly visible in CNT quantum dots with an electron-vibron coupling of $g = 3.3$ [35]. The population of the longitudinal phonons can be determined by looking at the amplitudes of the tunneling currents between the different excitations [32], shown in figure 1.11b. Also, second-order tunneling processes involving longitudinal phonons have been observed [36].

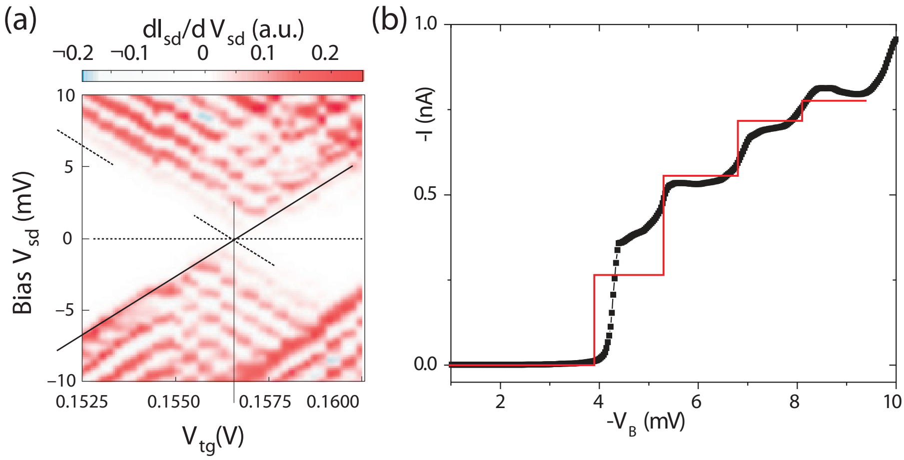

FIGURE 1.11: a) Stability diagram of a CNT, showing Franck-Condon blockade at low bias voltage, and longitudinal vibrational excitations [35]. b) Current through a CNT expressing the population of longitudinal phonons [32].

The large electron-vibron coupling in the case of flexural motion gives rise to a softening of the CNT spring, increased damping (for both see [37, 38] and Chs. 3 and 4), nonlinear restoring forces at high driving powers (Ch. 3), and mode coupling (Ch. 5). Under certain conditions, single-electron tunneling does not cause damping in the CNT quantum dot resonator, but leads to pumping of energy into the mechanical resonance, resulting in self-sustained oscillation. These single-electron effects arise from the large modulation of the average charge on the CNT quantum dot during its mechanical oscillation and are described in Chapters 3-5 in far greater detail.

1.4.2 DAMPING

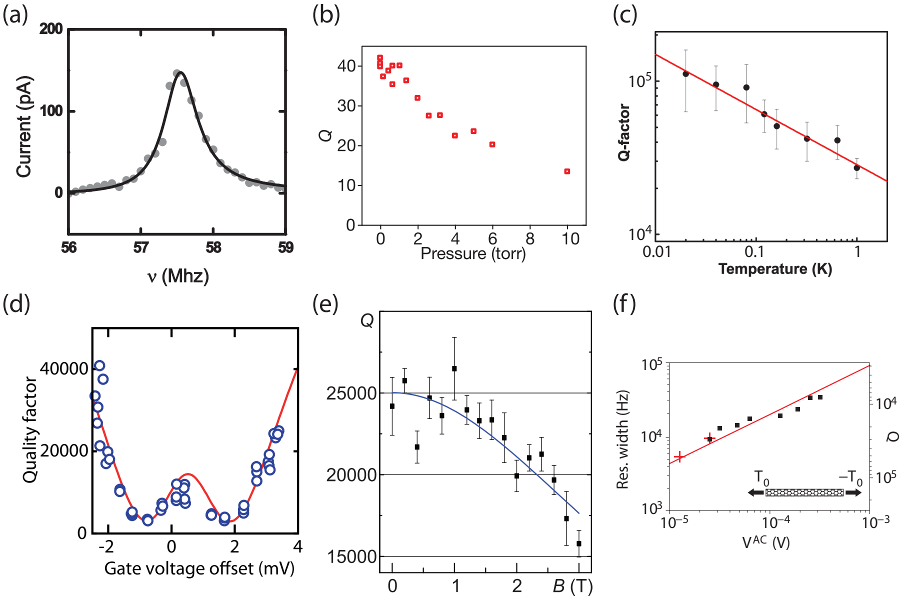

FIGURE 1.12: a) Amplitude response of a CNT mechanical resonator at room temperature showing a quality factor of 100 [39]. b-f) Damping in CNT mechanical resonators: b) Room-temperature gas damping, showing negligible damping below 1 Torr [40], c) temperature-dependent damping, fitted with $Q \propto T^{-0.36}$ [23], d) single-electron damping, showing a double Q-factor dip at higher bias voltage (Chapter 4), e) magnetic damping at cryogenic temperature [41], f) nonlinear damping of a CNT under tensile stress [5].

Because of the pristine single-atom nature of CNTs, damping due to impurities is not expected in CNT mechanical resonators. In practice however, considerable damping has been observed in room-temperature CNT resonators, with quality factors of 80 [40], 15 [27], and 100 [39] (see Fig. 1.12a). Gas damping [42] has been shown (see Fig. 1.12b) to be negligible at pressures below 1 Torr [40], becoming irrelevant at cryogenic temperatures. A theoretical investigation [43] suggests that, through tensile coupling, the thermal motion of higher flexural modes leads to frequency instability and therefore increased quality factors at room temperature, but not per se energy relaxation. Experimentally, the quality factor has been found to depend on temperature as $Q \propto T^{-0.36}$ [23] (see Fig. 1.12c) and as $Q \propto T^{-1}$ [38]. At cryogenic temperatures, quality factors as high as 140,000 have been observed [23]. Then, the dominant sources of damping are single-electron damping (Fig. 1.12d), magnetic damping (Fig. 1.12e), and nonlinear damping (Fig. 1.12f). Single-electron damping is discussed at length in Chapters 3 and 4. Magnetic damping [41] arises as oscillating eddy currents, brought about as the mechanical motion of the CNT changes the magnetic flux through the loop area, cause out-of-phase Lorentz forces acting on the CNT resonator. Nonlinear damping [5] is increased damping as the amplitude of oscillation increases. Suggested physical origins are coupling between linear damping and a nonlinear restoring force, clamping losses, sliding, and nonlinearities in phonon-phonon interactions.

1.4.3 NONLINEARITY

Because of its large aspect ratio, a CNT resonator is easily perturbed into the nonlinear regime, where the restoring force is no longer linear in displacement. In this subsection, we focus on the experimental results involving the Duffing nonlinearity, parametric excitation, and mode coupling. A theoretical framework can be found in chapter 6.

The Duffing nonlinearity is given by a restoring force that is cubic in displacement, and has been observed experimentally in CNT resonators through two mechanisms: geometry and the single-electron force. A simple argument (see Ch. 6) for geometric nonlinearity explains how the increased length of the CNT at high drive powers causes a stiffening nonlinear restoring force as tension increases with oscillation amplitude. In [40], a geometric Duffing nonlinearity is found, as the frequency response curve starts to tilt to higher frequencies as the drive power is increased (shown in Fig. 1.13a).

For the Duffing nonlinearity due to single-electron forces, the Duffing parameter, α_{SET}, is found (see Chapters 3, 4, and 6) to be either positive or negative, depending on the change of the average charge to third order in displacement during the mechanical motion. Across a Coulomb peak, the single-electron Duffing parameter can be made to change from negative, to positive, to negative again, in only millivolts of gate voltage. When the drive power is increased further, single-electron forces, combined with a (more) nonlinear detection, cause an intricate amplitude lineshape that can no longer be described by the Duffing model, and can even have tristable states.

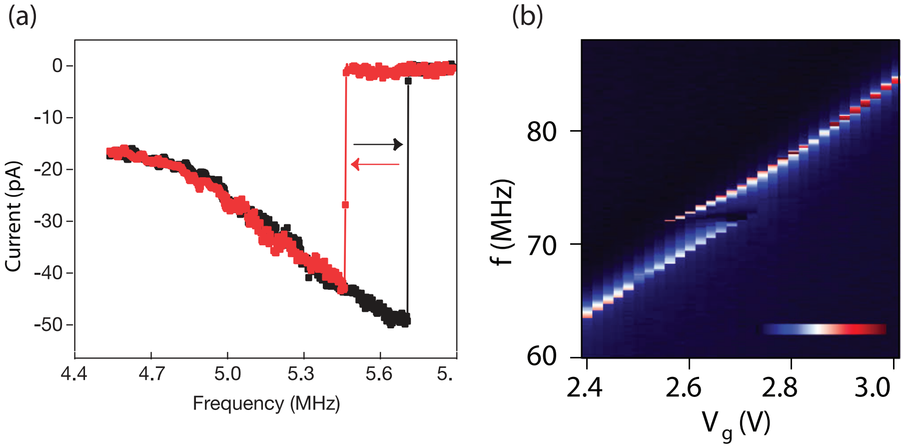

FIGURE 1.13: Nonlinearity in CNT mechanical resonators: a) forward and reverse amplitude response showing bistability and hysteresis due to geometrical Duffing nonlinearity [40], b) tension-induced mode coupling, leading to an avoided crossing in the lower mode [45].

Parametric excitation involves the modulation of one of the parameters of the system, in the case of [44] the spring constant, resulting in a nonlinear restoring force. The gain due to parametric excitation depends on the phase difference between the undriven or directly driven motion and the parametric excitation. When directly driven at the resonance frequency, the largest gain is found at a phase difference of ~-45 degrees between the direct and the parametric excitation. At a certain level of parametric excitation, the CNT sustains a certain amplitude without the necessity of a direct drive, resulting in self-oscillation. The high value of dk/dV_g, due to the large frequency dependence on gate voltage, makes CNT resonators ideal candidates for parametric excitation.

Flexural mode coupling, i.e. coupling between different harmonics of the flexural mode, in CNT resonators has origins analogous to the Duffing nonlinearity, arising due to tension [45] and due to single-electron forces (Chapter 5 of this Thesis). Nonlinearity due to tension is shown in Fig. 1.13b, occurring when the frequencies of two modes become commensurate and the tension of the higher mode causes parametric excitation of the lower mode, which results in an avoided crossing in the resonance frequency curve of the lower mode. For single-electron forces, the modulation of the average charge due to the motion of one mode leads to a change in the spring constant of the other mode. As with the single-electron Duffing nonlinearity, this mode coupling causes softening or stiffening in the other mode, depending on where on the Coulomb peak the frequency response is taken.

1.5 THIS THESIS

This Thesis consists of seven chapters. In **Chapter 2**, a review is given of the various experimental methods that have been used to detect the mechanical motion of a CNT, followed by a comparison of the different electrical methods. **Chapters 3-5** show experimental results linking single-electron tunneling through the CNT quantum dot with mechanical properties such as the resonance frequency, the quality factor, the Duffing nonlinearity parameter, and mode coupling. Here, **Chapter 4** provides a quantitative comparison between the experiment and a devised theoretical model and **Chapter 5** shows single-electron mode coupling. **Chapter 6** discusses the different contributions to nonlinear restoring forces in CNT mechanical resonators in a theoretical treatment. Finally, **Chapter 7** contains a detailed description of a novel electrical high-bandwidth readout scheme, using a close-proximity high-impedance HEMT amplifier, along with experimental results.

REFERENCES

[1] H. B. Meerwaldt, G. A. Steele, and H. S. J. van der Zant, *Fluctuating Nonlinear Oscillators* (Oxford University Press, 2012), chap. Carbon nanotubes: Nonlinear high-Q resonators with strong coupling to single-electron tunneling, pp. 312–340, URL `http://arxiv.org/abs/1205.4921`.

[2] Y. T. Yang, K. L. Ekinci, X. M. H. Huang, L. M. Schiavone, M. L. Roukes, C. A. Zorman, and M. Mehregany, *Monocrystalline silicon carbide nanoelectromechanical systems*, Applied Physics Letters **78**, 162 (2001).

[3] A. K. Hüttel, M. Poot, B. Witkamp, and H. S. J. Van der Zant, *Nanoelectromechanics of suspended carbon nanotubes*, New Journal of Physics **10**, 095003 (2008).

[4] W. J. Venstra, H. J. R. Westra, and H. S. J. van der Zant, *Mechanical stiffening, bistability, and bit operations in a microcantilever*, Applied Physics Letters **97**, 193107 (2010).

[5] A. Eichler, J. Moser, J. Chaste, M. Zdrojek, I. Wilson-Rae, and A. Bachtold, *Nonlinear damping in mechanical resonators made from carbon nanotubes and graphene*, Nature Nanotechnology **6**, 339 (2011).

[6] K. L. Ekinci, X. M. H. Huang, and M. L. Roukes, *Ultrasensitive nanoelectromechanical mass detection*, Applied Physics Letters **84**, 4469 (2004).

[7] H.-Y. Chiu, P. Hung, H. W. C. Postma, and M. Bockrath, *Atomic-Scale Mass Sensing Using Carbon Nanotube Resonators*, Nano Letters **8**, 4342 (2008).

[8] K. Jensen, K. Kim, and A. Zettl, *An atomic-resolution nanomechanical mass sensor*, Nature Nanotechnology **3**, 533 (2008).

[9] B. Lassagne, D. Garcia-Sanchez, A. Aguasca, and A. Bachtold, *Ultrasensitive mass sensing with a nanotube electromechanical resonator*, Nano Letters **8(11)**, 3735 (2008).

[10] J. Chaste, A. Eichler, J. Moser, G. Ceballos, R. Rurali, and A. Bachtold, *A nanomechanical mass sensor with yoctogram resolution*, Nature Nanotechnology **7**, 301 (2012).

[11] A. N. Cleland and M. L. Roukes, *A nanometre-scale mechanical electrometer*, Nature **392**, 160 (1998).

[12] R. G. Knobel and A. N. Cleland, *Nanometre-scale displacement sensing using a single electron transistor*, Nature **424**, 291 (2003).

[13] A. D. O'Connell, M. Hofheinz, M. Ansmann, R. C. Bialczak, M. Lenander, E. Lucero, M. Neeley, D. Sank, H. Wang, M. Weides, et al., *Quantum ground state and single-phonon control of a mechanical resonator*, Nature **464**, 697 (2010).

[14] J. D. Teufel, T. Donner, D. Li, J. W. Harlow, M. S. Allman, K. Cicak, A. J. Sirois, J. D. Whittaker, K. W. Lehnert, and R. W. Simmonds, *Sideband cooling of micromechanical motion to the quantum ground state*, Nature **475**, 359 (2011).

[15] J. Chan, T. P. Mayer Alegre, A. H. Safavi-Naeini, J. T. Hill, A. Krause, S. Groeblacher, M. Aspelmeyer, and O. Painter, *Laser cooling of a nanomechanical oscillator into its quantum ground state*, Nature **478**, 89 (2011).

[16] S. Sapmaz, Y. M. Blanter, L. Gurevich, and H. S. J. van der Zant, *Carbon nanotubes as nanoelectromechanical systems*, Physical Review B **67**, 235414 (2003).

[17] M. Poot, B. Witkamp, M. A. Otte, and H. S. J. Van der Zant, *Modelling suspended carbon nanotube resonators*, Physica Status Solidi (b) **244**, 4252 (2007).

[18] C. Journet, W. K. Maser, P. Bernier, A. Loiseau, M. L. delaChapelle, S. Lefrant, P. Deniard, R. Lee, and J. E. Fischer, *Large-scale production of single-walled carbon nanotubes by the electric-arc technique*, Nature **388**, 756 (1997).

[19] A. Thess, R. Lee, P. Nikolaev, H. J. Dai, P. Petit, J. Robert, C. H. Xu, Y. H. Lee, S. G. Kim, A. G. Rinzler, et al., *Crystalline ropes of metallic carbon nanotubes*, Science **273**, 483 (1996).

[20] J. Kong, H. T. Soh, A. M. Cassell, C. F. Quate, and H. J. Dai, *Synthesis of individual single-walled carbon nanotubes on patterned silicon wafers*, Nature **395**, 878 (1998).

[21] P. Nikolaev, M. J. Bronikowski, R. K. Bradley, F. Rohmund, D. T. Colbert, K. A. Smith, and R. E. Smalley, *Gas-phase catalytic growth of single-walled carbon nanotubes from carbon monoxide*, Chemical Physics Letters **313**, 91 (1999).

[22] J. Cao, Q. Wang, and H. Dai, *Electron transport in very clean, as-grown suspended carbon nanotubes*, Nature Materials **4**, 745 (2005).

[23] A. K. Hüttel, G. A. Steele, B. Witkamp, M. Poot, L. P. Kouwenhoven, and H. S. J. van der Zant, *Carbon Nanotubes as Ultrahigh Quality Factor Mechanical Resonators*, Nano Letters **9**, 2547 (2009).

[24] *Scientific background on the nobel prize in physics 2010, graphene*, URL `http://bitly.com/XFBSn4`.

[25] Q. P. Unterreithmeier, T. Faust, and J. P. Kotthaus, *Damping of nanomechanical resonators*, Physical Review Letters **105**, 27205 (2010).

[26] M. Poot and H. S. J. van der Zant, *Mechanical systems in the quantum regime*, Physics Reports-Review Section of Physics Letters **511**, 273 (2012).

[27] H. B. Peng, C. W. Chang, S. Aloni, T. D. Yuzvinsky, and A. Zettl, *Ultrahigh frequency nanotube resonators.*, Physical Review Letters **97**, 087203 (2006).

[28] J. Chaste, M. Sledzinska, M. Zdrojek, J. Moser, and A. Bachtold, *High-frequency nanotube mechanical resonators*, Applied Physics Letters **99**, 213502 (2011).

[29] E. A. Laird, F. Pei, W. Tang, G. A. Steele, and L. P. Kouwenhoven, *A High Quality Factor Carbon Nanotube Mechanical Resonator at 39 GHz*, Nano Letters **12**, 193 (2011).

[30] D. A. Walters, L. M. Ericson, M. J. Casavant, J. Liu, D. T. Colbert, K. A. Smith, and R. E. Smalley, *Elastic strain of freely suspended single-wall carbon nanotube ropes*, Applied Physics Letters **74**, 3803 (1999).

[31] M. F. Yu, O. Lourie, M. J. Dyer, K. Moloni, T. F. Kelly, and R. S. Ruoff, *Strength and breaking mechanism of multiwalled carbon nanotubes under tensile load*, Science **287**, 637 (2000).

[32] S. Sapmaz, J. P. Herrero, Y. M. Blanter, C. Dekker, and H. S. J. van der Zant, *Tunneling in Suspended Carbon Nanotubes Assisted by Longitudinal Phonons*, Physical Review Letters **96**, 026801 (2006).

[33] L. Vitali, M. Burghard, M. A. Schneider, L. Liu, S. Y. Wu, C. S. Jayanthi, and K. Kern, *Phonon spectromicroscopy of carbon nanostructures with atomic resolution*, Physical Review Letters **93**, 136103 (2004).

[34] B. J. LeRoy, S. G. Lemay, J. Kong, and C. Dekker, *Electrical generation and absorption of phonons in carbon nanotubes*, Nature **432**, 371 (2004).

[35] R. Leturcq, C. Stampfer, K. Inderbitzin, L. Durrer, C. Hierold, E. Mariani, M. G. Schultz, F. von Oppen, and K. Ensslin, *Franck-Condon blockade in suspended carbon nanotube quantum dots*, Nature Physics **5**, 327 (2009).

[36] A. K. Hüttel, B. Witkamp, M. Leijnse, M. R. Wegewijs, and H. S. J. van der Zant, *Pumping of Vibrational Excitations in the Coulomb-Blockade Regime in a Suspended Carbon Nanotube*, Physical Review Letters **102**, 225501 (2009).

[37] B. Lassagne, Y. Tarakanov, J. Kinaret, D. Garcia-Sanchez, and A. Bachtold, *Coupling Mechanics to Charge Transport in Carbon Nanotube Mechanical Resonators*, Science **325**, 1107 (2009).

[38] M. Ganzhorn and W. Wernsdorfer, *Dynamics and Dissipation Induced by Single-Electron Tunneling in Carbon Nanotube Nanoelectromechanical Systems*, Physical Review Letters **108**, 175502 (2012).

[39] B. Witkamp, M. Poot, and H. S. J. van der Zant, *Bending-mode vibration of a suspended nanotube resonator*, Nano Letters **6**, 2904 (2006).

[40] V. Sazonova, Y. Yaish, H. Ustunel, D. Roundy, T. A. Arias, and P. L. McEuen, *A tunable carbon nanotube electromechanical oscillator*, Nature **431**, 284 (2004).

[41] D. R. Schmid, P. L. Stiller, C. Strunk, and A. K. Hüttel, *Magnetic damping of a carbon nanotube nano-electromechanical resonator*, New Journal of Physics **14**, 083024 (2012).

[42] M. J. Martin and B. H. Houston, *Gas damping of carbon nanotube oscillators*, Applied Physics Letters **91**, 103116 (2007).

[43] A. W. Barnard, V. Sazonova, A. M. van der Zande, and P. L. McEuen, *Fluctuation broadening in carbon nanotube resonators*, Proceedings of the National Academy of Sciences **109**, 19093 (2012).

[44] A. Eichler, J. Chaste, J. Moser, and A. Bachtold, *Parametric Amplification and Self-Oscillation in a Nanotube Mechanical Resonator*, Nano Letters **11**, 2699 (2011).

[45] A. Eichler, M. del Álamo Ruiz, J. A. Plaza, and A. Bachtold, *Strong coupling between mechanical modes in a nanotube resonator*, Physical Review Letters **109**, 25503 (2012).

2

DETECTION OF CARBON NANOTUBE MECHANICAL MOTION

2.1 DETECTION METHODS FOR CARBON NANOTUBE MECHANICAL RESONATORS

In this Chapter, we discuss different methods to detect the motion of CNT resonators. First, we look at the detection of radial and longitudinal modes using the method of spectroscopy. Next, we consider the use of optical, microscopy, and electrical methods for the detection of flexural motion. Optical methods involve the use of an optical cavity. Microscopy methods can be divided into scanning force microscopy, transmission electron microscopy, and field emission microscopy. We describe the electrical methods of mechanically-induced heating, the two-source mixing technique, the FM mixing technique, the so-called rectification technique, and the use of a superconducting quantum interference device. The electrical methods are self-detecting, because the CNT is both the mechanical resonator studied and the detector.

The amplitudes of radial and longitudinal modes are too small to be imaged by the microscopy readout schemes and couple too weakly to the gate electrode to be

---

Parts of this Chapter have been published in "Fluctuating nonlinear oscillators" (Oxford University Press, 2012), ed. Mark Dykman [1].

measured by the electrical readout schemes. In order to detect these modes, the technique of tunneling spectroscopy has been performed on CNT resonators, using a three-terminal setup for the longitudinal modes [2–4], and a scanning tunneling microscope (STM) for the radial modes [5, 6]. Spectroscopy involves probing the energy levels of the CNT, as it becomes a quantum dot at cryogenic temperatures. Tunneling of electrons or holes through the CNT quantum dot takes place when the chemical potential of the level of the CNT is between the chemical potentials of the source and the drain, or of the STM tip and the drain (see figure 2.1a). The chemical potential of the level is then discerned as a peak in the differential conductance, dI/dV_b. Besides having electronic excited states, the CNT quantum dot exhibits vibrational excited states, caused by the longitudinal and radial modes (see figure 2.1b). The energy, E_{vib}, and the resonance frequency, ω_0, of these vibrational modes are determined by looking at the difference in bias voltage, ΔV_b, between the peaks in differential conductance using $E_{vib} = e\Delta V_b = \hbar\omega_0$. The vibrational modes are distinguished between longitudinal or radial modes, by comparing the obtained resonance frequency with theoretical predictions.

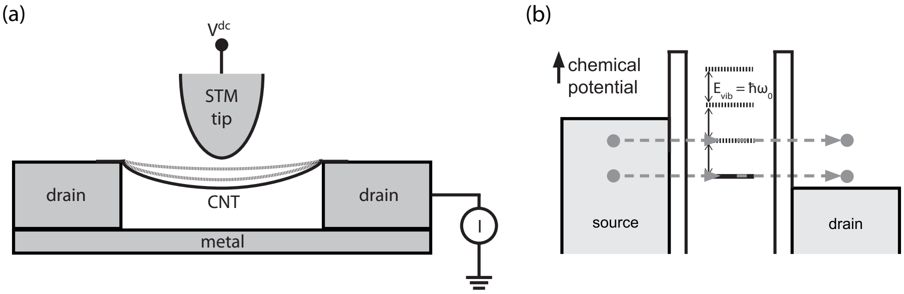

FIGURE 2.1: a) Scanning tunneling microscopy. The spectrum of the CNT at a certain position is read out through electrons tunneling from the STM-tip onto the CNT. b) Energy diagram, showing transport through vibrational excitations of the CNT quantum dot.

The use of optical methods is common for top-down fabricated nanomechanical resonators, but has its difficulties with CNTs, because of their small cross-section. In Ref. [7], the reflection of a laser from the CNT cantilever back onto an optical microscope was used to investigate the CNT's motion in a liquid. In Ref. [8], an optical cavity was formed between two concave ends of optical fibers. Here, the length of the cavity is optimized to be on the slope of an optical resonance of the cavity. The displacement of the CNT in the cavity causes a change in the power reflected from the cavity through dispersive and dissipative interaction. By looking at the spectrum of this power, the thermal motion of a multiwalled CNT or a few-CNT rope could be discerned.

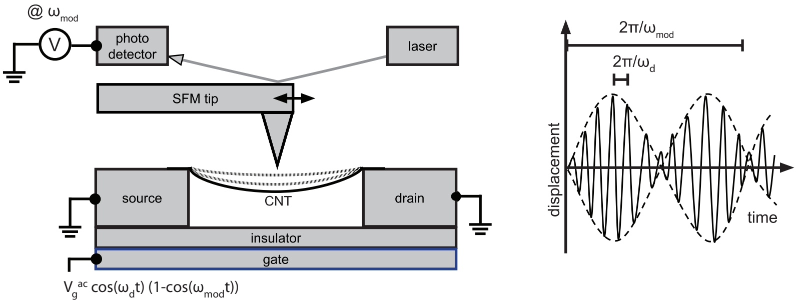

FIGURE 2.2: Scanning force microscopy. A suspended doubly-clamped CNT is brought into motion by a nearby gate electrode (left). The amplitude-modulated motion (right) at different parts of the CNT is read out at ω_{mod} by a tip in tapping mode.

2.1.1 MICROSCOPY METHODS

Using scanning force microscopy (SFM) [9], it is possible to spatially image the different mode shapes in a CNT resonator. Figure 2.2 shows an SFM in tapping mode with the tip positioned above a doubly clamped CNT. The CNT is actuated by a nearby gate at a frequency ω_d. Since the bandwidth of the SFM is not high enough to measure the oscillations of the CNT at the resonance frequency, an amplitude-modulated actuation signal is used for the voltage on the gate with a frequency of ω_{mod}. The tip cannot follow the high-frequency CNT vibrations, but it can follow the envelope of the oscillation. On resonance, the amplitude-modulated actuation results in a fast-oscillating displacement envelope with frequency ω_{mod} (see figure 2.2). The modulation frequency can be conveniently chosen such that the signal can be measured with a lock-in amplifier. For higher sensitivity, ω_{mod} is matched to the first eigenmode of the SFM tip. The amplitude of oscillation at different locations on the CNT provides a time averaged image of the shape of the driven mode.

With transmission electron microscopy (TEM) [10], a fiber of CNT cantilevers is connected to a gold wire, which is placed between the electron gun and the viewing system, as shown in figure 2.3. By applying a voltage to the CNTs by a nearby electrode, the ones that are not perpendicular to the grounded counter electrode are attracted to it. To drive the CNTs, an alternating voltage is applied to them and the resulting envelope of the motion is observed in the TEM image. As with the SFM method, the low bandwidth of TEM imaging only allows visualizing the mode shape of the vibrations.

With field-emission microscopy (FEM), temporal and spatial information on the flexural motion is obtained. Figure 2.4 shows a CNT cantilever to which a few

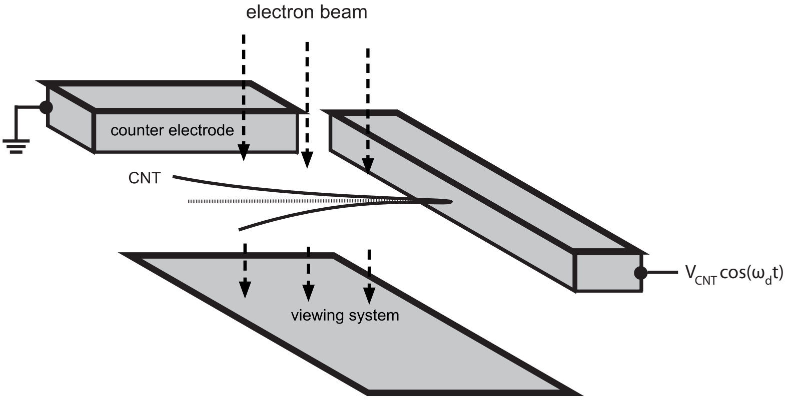

FIGURE 2.3: Transmission electron microscopy. A suspended CNT cantilever is driven by applying a voltage V_{CNT} to the CNT with respect to a grounded counter electrode. Electrons from an incident electron beam are not transmitted through the CNT and as result an image of the flexural motion is obtained.

hundred volts is applied. A field-emission tunnel current now flows to the anode which is placed up to a few hundred nm away. In one case [11], the CNT was excited by radio waves from a nearby antenna. At the mechanical resonance frequency the distance between the tip of the CNT, which acts as a cathode, and the anode oscillates. This causes the tunnel resistance and therefore the current flowing through the circuit to oscillate. In this way, the CNT acts as a rectifier; the current is highest when the CNT is in its equilibrium position and becomes lower, but never negative, when the CNT moves away from this position in either direction. As a consequence, the time-averaged current decreases when the CNT is set in motion. Thus, the ac motion of the CNT is probed by a dc measurement of the averaged current. In another case [12] the CNT was positioned near a phosphor screen so that the averaged 2-dimensional image of emitted electrons was recorded by a 25 Hz video camera.

It should be noted that the three microscopy techniques operate at room temperature. At low temperatures, mechanical properties such as damping change dramatically. We now discuss the five electrical detection methods that are used at low temperature.

2.1.2 ELECTRICAL METHODS

In Ref. [13], mechanical motion of a CNT was observed for the first time, as mechanically-induced heating caused ropes of ~100 CNTs, suspended between superconducting leads, to return to the resistive state at a mechanical resonance.

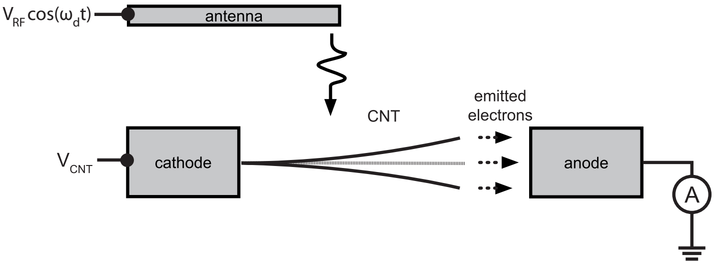

FIGURE 2.4: Field emission microscopy. A suspended CNT cantilever is excited by radio waves from a nearby antenna. Current tunnels from the CNT to the anode and oscillates with the motion of the CNT resonator.

However, without the observation of tuning of the resonance frequency by e.g. gate-induced tension, the origin of the resistance at certain excitation frequencies could be non-mechanical.

In measuring the high-frequency response of mechanical resonators, one often employs electrical frequency-mixing techniques. Here, a nonlinear element, i.e. an element whose output signal is not linearly dependent on the input signals, mixes two different high-frequency signals to their difference frequency, which is considerably lower and is measured more easily. In the case of a CNT mechanical resonator, the CNT itself is used as the nonlinear element. To measure CNTs using the two-source mixing technique [14–17], the working principle is modeled as follows. A three terminal setup is used, as shown in figure 2.5. The current $I = GV_b$ flowing through the CNT, where G is the conductance of the CNT and V_b is the bias voltage over the CNT, depends on the gate-induced charge, $q_c = C_g V_g$, where C_g is the capacitance to the gate and V_g is the gate voltage. When the CNT moves away from its equilibrium position, the capacitance to the gate oscillates with δC_g, giving $\delta q_c^{mech} = V_g \cdot \delta C_g$. Also, when an oscillating signal δV_g^{elec} is applied to the gate, the gate induced charge changes as: $\delta q_c^{direct} = C_g \cdot \delta V_g^{elec}$. Putting these two contributions together gives the time-dependent conductance:

$$\delta G = \frac{dG}{dV_g}\left(\delta V_g^{elec} + \frac{V_g}{C_g}\delta C_g\right). \tag{2.1}$$

The two contributions both oscillate at a frequency ω_d but can in general have a different phase. Note that the frequency of the mechanical oscillation of the CNT equals the frequency of the driving voltage applied to the gate electrode. When also the bias voltage is alternated with δV_b, but now at a frequency $\omega_d + \Delta\omega$, both the mechanical oscillations and the direct oscillations are mixed given that $\delta I = \delta G \cdot \delta V_b$.

One mixing component occurs at $\Delta\omega$, which can be conveniently chosen at a few kHz. This signal is then detected using a lock-in amplifier.

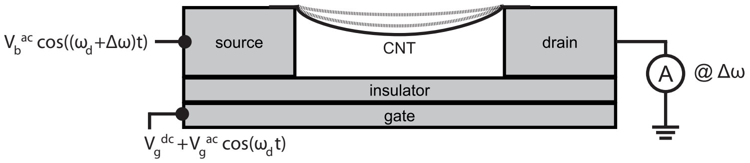

FIGURE 2.5: Detecting the CNT's motion using the two-source mixing technique. A CNT is doubly clamped between a source and a drain electrode suspended above and driven by a gate electrode. The flexural motion of the CNT mixes the bias voltage at $\omega_d + \Delta\omega$ and the gate voltage at ω_d to a current at $\Delta\omega$. When frequency-modulation of the source voltage is performed, no ac voltage needs to be applied to the gate electrode.

Using the FM mixing technique, measurement of the flexural motion of a CNT resonator has also been performed. This technique employs a frequency-modulated (FM) ac voltage applied to the source electrode [18]. Because of the frequency modulation, the source voltage now contains, besides a signal at the carrier frequency, ω_d, sidebands around the carrier frequency, whose amplitude is determined by a Bessel function of the first kind, J_n:

$$\begin{aligned} V_b^{FM}(t) &= V_b^{ac} \times \Big[J_0(\frac{\omega_\Delta}{\Delta\omega})\cos(\omega_d t) \\ &\quad + \sum_{n=1}^{\infty} J_n(\frac{\omega_\Delta}{\Delta\omega})\big(\cos((\omega_d - n\Delta\omega)t) + (-1)^n \cos((\omega_d + n\Delta\omega)t)\big)\Big] \end{aligned} \tag{2.2}$$

Figure 2.6 illustrates how the frequency spacing between the sidebands is determined by the modulation frequency, $\Delta\omega$. The sidebands spread around the carrier frequency by approximately the deviation frequency, ω_Δ, i.e. the frequency modulation depth. In this case, no ac voltage needs to be applied to the gate, as the CNT is actuated by the capacitive force, $F_{ac} = -(dC/du)(C_s/C_{tot})V_g^{dc}V_b^{ac}$, due to the voltage difference between the CNT and the gate. To actuate the CNT, the carrier frequency of the source voltage should be set to the mechanical resonance frequency. When the modulation frequency is smaller than the resonator's bandwidth, $\Delta\omega \ll \omega_0/Q$, the sidebands also drive the CNT. The modulation of the conductance due to the mechanical motion at the carrier frequency, and possibly at each of these sidebands, combined with the ac source voltage of its neighbouring sideband, causes a mixing current at $\Delta\omega$. This mixing current is proportional to the

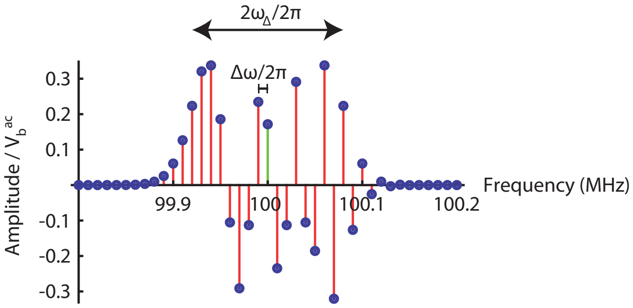

FIGURE 2.6: Illustrative spectrum of the FM signal supplied to the source: the sidepeaks (red) have a separation of $\Delta\omega/2\pi = 10$ kHz from the carrier frequency (green) at $\omega_d/2\pi = 100$ MHz, where 98% of the power is within twice the devation frequency, $\omega_\Delta/2\pi = 80$ kHz. Note that, for each pair of consecutive peaks below the resonance frequency, there is a pair of peaks above the resonance frequency with opposite parity. The relative weight of the peaks is highly dependent on the modulation index, $\omega_\Delta/\Delta\omega$.

deviation frequency, ω_Δ:

$$I_{mix} = \frac{1}{2}\frac{d^2 I}{dV_g dV_b} V_b^{ac} \frac{V_g^{dc}}{C_g}\frac{dC_g}{du}\omega_\Delta \frac{\partial}{\partial\omega_d}\mathrm{Re}(u_{ac}), \tag{2.3}$$

where $\mathrm{Re}(u_{ac})$ denotes the real part of the complex vibration amplitude. Interestingly, because of the opposing amplitudes of the sidebands due to the Bessel function, the electrical mixing current reduces to zero. The absence of an electrical mixing current is an advantage of the FM mixing technique compared to the two-source mixing technique. Disadvantages arise from the actuation of the CNT through the source and not the gate electrode. A CNT three terminal device withstands a lower voltage on the source than on the gate and the power of the drive and probe signals cannot be set independently.

Another technique that resembles the mixing techniques transduces the mechanical oscillations of the CNT resonator at several hundred megahertz into a dc current [19], thereby using the CNT resonator as a rectifier. The advantage of this rectifying technique is that the amplitude of the mechanical motion is given by a change in the dc current flowing through the CNT. As with the mixing techniques, the use of the rectification technique avoids the difficulty of getting small, high-frequency signals out of a setup at millikelvin temperatures and minimizing the crosstalk from the actuation onto the measurement signal.

The working principle for the rectification technique is as follows. The CNT is suspended between source and drain electrodes above a gate electrode. At low temperatures, the CNT acts as a suspended quantum dot, in which charging effects dominate transport. It is actuated using a nearby antenna, which sends out an oscillating electric field. When the CNT oscillates, the distance to the gate changes in time, and therefore the capacitance $\delta C_g = \frac{dC_g}{du} u_{ac} \cos(\omega_d t)$, where u_{ac} is the ac amplitude of the CNT. Since the only relevant quantity is the charge induced by the gate, it is equivalent to say that the gate voltage changes as $\delta V_g^{mech} = \frac{V_g}{C_g} \delta C_g$. Expanding the current through the CNT quantum dot with respect to gate voltage, one obtains:

$$\begin{aligned} I(V_g + \delta V_g^{mech}) = I(V_g) &+ \frac{dI}{dV_g} \frac{V_g}{C_g} \frac{dC_g}{du} u_{ac} \cos(\omega_d t) \\ &+ \frac{1}{2} \frac{d^2 I}{dV_g^2} \left(\frac{V_g}{C_g} \frac{dC_g}{du} \right)^2 u_{ac}^2 \left(\frac{1}{2} + \frac{1}{2} \cos(2\omega_d t) \right). \end{aligned} \tag{2.4}$$

The high resistance of CNTs combined with a high capacitance to ground often means that the bandwidth is too low to measure the oscillations at ω_d and $2\omega_d$ directly.[1] Omitting the oscillating terms in Equation 2.4, the change in the dc current ΔI due to mechanical motion is given by:

$$\Delta I = \frac{1}{4} \frac{d^2 I}{dV_g^2} \left(\frac{V_g}{C_g} \frac{dC_g}{du} \right)^2 u_{ac}^2. \tag{2.5}$$

Important to note is that the change in current is averaged over time and that it is proportional to the amplitude squared.

Equation 2.5 shows that, in order to observe a large mechanical signal, $d^2 I/dV_g^2$ should be high, as is the case in the Coulomb blockade regime [20, 21]. When measured on a Coulomb peak, the second derivative is negative and therefore the change in current as well. In the Coulomb valley, both the second derivative and the change in current are positive. Typically, $d^2 I/dV_g^2$ is several $\mu A/V^2$. On the inflection point of the Coulomb peak, $d^2 I/dV_g^2 = 0$, and there is no change in current. This is in contrast to the mixing technique, which has the highest signal on the inflection point and the lowest on the Coulomb peak or in the valleys (cf. Equation 2.1).

Using the previously mentioned electrical techniques, it is not possible to determine the static displacement of a CNT, when it is pulled towards the gate electrode by a gate voltage. Embedding the CNT in a superconducting quantum interference device (SQUID), with a gate electrode added [22], allows for this measurement in the following way. A dc SQUID is a two-terminal superconducting loop with two parallel Josephson junctions, where the critical current of the SQUID is

---

[1] A method to significantly increase the bandwidth is discussed in Chapter 7.

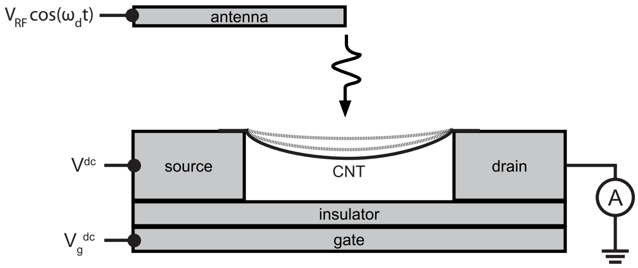

FIGURE 2.7: Detecting the CNT's motion using the rectification technique. A CNT is doubly clamped between a source and a drain electrode suspended above a gate electrode. The CNT is driven by a high-frequency signal applied to an antenna at approximately 1 cm from the CNT. The single-electron tunnel current through the CNT quantum dot contains information on the oscillation of the CNT at dc due to a rectification effect from Coulomb blockade.

determined by the magnetic flux that passes through the loop (see figure 2.8a). Using a single suspended CNT as the two Josephson junctions, a magnetic field is applied at a small angle with respect to the plane of the SQUID loop. The flux through the loop is changed by the static displacement of the CNT, when the gate pulls at it (see figure 2.8b). As the gate voltage in the experiment is changed from 0 to -4 V, the 800 nm long CNT displaces 7.4 nm. Combining the SQUID readout and the abovementioned rectification technique, the dynamic displacement of the CNT is also observed.

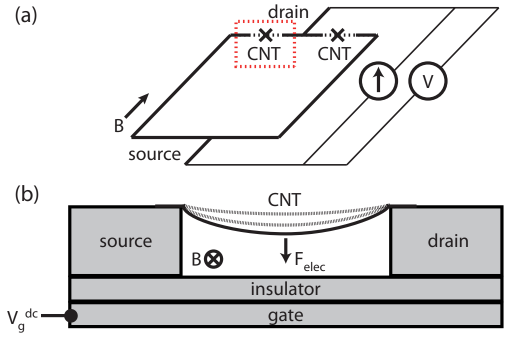

FIGURE 2.8: A superconducting quantum interference device used to measure the static displacement of a CNT mechanical resonator: (a) a four probe measurement measures the voltage across the SQUID, which contains two segments of the CNT as its Josephson junctions, (b) zoom-in of the red dashed rectangle in (a): an electric force F_{elec}, acting on the CNT and applied by a gate voltage, changes the magnetic flux through the SQUID loop.

2.2 COMPARISON OF ELECTRICAL DETECTION METHODS FOR CNT MECHANICAL RESONATORS

Using three-terminal devices, there is a myriad of electrical techniques to detect the CNT's mechanical motion. Besides the three techniques described in the previous section: two-source mixing, FM mixing, and rectification, we introduce five more techniques in this section and compare all eight. The five new techniques are dubbed: direct readout, two-source gate mixing, parametric excitation, $2\omega_d$ excitation, and $2\omega_0$ readout. As we describe the electrical techniques, we will see that readout and excitation are connected to each other. Concerning readout, the techniques can be divided according to the frequency at which the signal is read out: dc for the rectification technique, $\Delta\omega$ for the mixing techniques, ω_d for the direct readout, and $2\omega_d$ for the $2\omega_d$ readout. Different excitation schemes at ω_d or $2\omega_d$ can be combined with different readout schemes.

A direct readout scheme has not yet been successfully applied for measuring CNT mechanical resonators, but only for graphene sheet resonators [23] and nanowires [24]. Figure 2.9 shows the schematics of the required setup. The readout scheme is direct in the sense that the signal is read out at the drain of the CNT at the same frequency as the drive voltage applied to the gate electrode. It is important to have a device with a high transconductance, dG/dV_g. Then, the mechanical resonance causes an oscillating conductance of the resonator at ω_d as the resonator moves towards and away from the gate electrode. Combined with a dc bias voltage, this oscillating conductance gives rise to an oscillating current passing through the resonator, which is detected at the drain, given by:

$$I = \frac{dG}{dV_g} V_b^{dc} \left(\frac{V_g}{C_g} \frac{dC_g}{du} \right) u_{ac}. \tag{2.6}$$

It is in the end the most straightforward and flexible electrical measurement technique, but bandwidth limitations and crosstalk cause significant technical difficulties. Chapter 7 goes into more detail on the motivation and challenges for high-bandwidth readout of CNT mechanical resonators.

The two-source gate mixing technique is a proposed excitation scheme, to be combined with a $\Delta\omega$ readout. The technique is similar to the rectification technique in that two gate voltage-induced signals are mixed. The difference lies in that it does not lead to a response at dc, but at the difference frequency between the two gate signals. This technique is useful in the Coulomb blockade regime, when $d^2I/dV_g^2 \gg d^2I/dV_g dV_b$. It should be noted that contrary to the two-source mixing technique, the two signals applied in the two-source gate mixing technique are interchangeable, as they are both applied to the gate. This means that mechan-

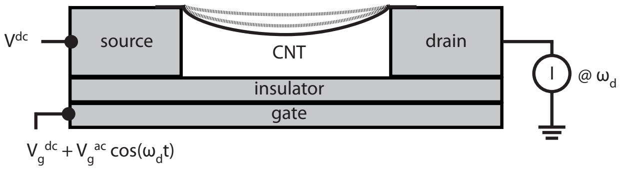

FIGURE 2.9: Direct readout of a CNT's mechanical motion at the drive frequency, ω_d, using a three terminal device.

ical motion occurs when either of the signals at ω_d and $\omega_d + \Delta\omega$ matches the mechanical resonance frequency, resulting in the current being mixed down to $\Delta\omega$.

The $2\omega_d$ readout scheme is a proposal that is similar to the rectification technique and is suitable for systems with a high d^2I/dV_g^2. Instead of using the component rectified to dc, the component up-converted to $2\omega_d$ is read out. This technique moves the signal away from the high $1/f$ noise at dc, but requires a setup with a bandwidth exceeding $2\omega_0$.

The parametric excitation scheme involves excitation of the mechanical motion with a force at $2\omega_0$. It has the advantage that the gate voltage causing the excitation takes place at $2\omega_0$, while the signal can be read out at ω_0. This avoids electrical crosstalk of the ac gate voltage onto the measured signal. Since this scheme merely specifies the excitation and not the readout, it can in principle be combined with another readout technique, as has been done with the FM mixing technique in [25]. More details on parametric excitation as a nonlinear restoring force can be found in section 6.2.

The $2\omega_d$ excitation scheme has the same reasoning behind it, to avoid having the ac gate voltage at the same frequency as the current through the CNT. This can be done by driving the CNT not with the (capacitive) force $\propto 2V_g^{dc}V_g^{ac}\cos(\omega_d t)$ at ω_d, but with the force $\propto \left(V_g^{ac}\right)^2\cos(2\omega_d t)$ at $2\omega_d$. Now, the gate voltage is at ω_d, but the current flowing through the CNT is mechanically modulated at $2\omega_d$. Since in general $V_g^{dc} \gg V_g^{ac}$, a reduction of the driving force is often the result. In [15], this excitation scheme has been combined with the two-source mixing readout scheme.

Besides being mechanical or electrical in nature, contributions to the measured current can be divided into currents due to the CNT's (trans)conductance, due to its capacitance, and due to capacitive crosstalk. To describe the current due to the CNT's (trans)conductance, the current is expanded to second order with respect to gate and bias voltage. Here, we use three infinitesimals, describing the ac bias and gate voltage, and the equivalent gate voltage due to the mechanical motion, oscillating at a yet unspecified frequency ω:

$$\begin{aligned} \delta V_b &= V_b^{ac}\cos(\omega t), && (2.7)\\ \delta V_g^{elec} &= V_g^{ac}\cos(\omega t), && (2.8)\\ \delta V_g^{mech} &= \frac{V_g^{dc}}{C_g}\frac{dC_g}{du}u_{ac}\cos(\omega t). && (2.9) \end{aligned}$$

The depiction of the mechanical motion with an oscillating gate voltage, δV_g^{mech}, arises from its equivalent influence on the gate induced charge on the CNT, δq_c, as an oscillating gate capacitance due to mechanical motion, δC_g:

$$\delta q_c = V_g^{dc}\cdot\delta C_g \Leftrightarrow \delta q_c = C_g\cdot\delta V_g^{mech} \tag{2.10}$$

The current, expanded to second order, then reads:

$$\begin{aligned} &I(V_b^{dc}+\delta V_b, V_g^{dc}+\delta V_g^{elec}+\delta V_g^{mech}) = \\ &\quad \underbrace{I(V_b^{dc},V_g^{dc})}_{\text{I}} + \underbrace{\frac{dI}{dV_b}\delta V_b}_{\text{II}} + \underbrace{\frac{dI}{dV_g}\delta V_g^{elec}}_{\text{III}} + \underbrace{\frac{dI}{dV_g}\delta V_g^{mech}}_{\text{IV}} \\ &\quad + \underbrace{\frac{1}{2}\frac{d^2I}{dV_b^2}(\delta V_b)^2}_{\text{V}} + \underbrace{\frac{1}{2}\frac{d^2I}{dV_g^2}\left(\delta V_g^{elec}\right)^2}_{\text{VI}} + \underbrace{\frac{1}{2}\frac{d^2I}{dV_g^2}\left(\delta V_g^{mech}\right)^2}_{\text{VII}} \\ &\quad + \underbrace{\frac{d^2I}{dV_g^2}\delta V_g^{elec}\delta V_g^{mech}}_{\text{VIII}} + \underbrace{\frac{d^2I}{dV_b dV_g}\delta V_b\delta V_g^{elec}}_{\text{IX}} + \underbrace{\frac{d^2I}{dV_b dV_g}\delta V_b\delta V_g^{mech}}_{\text{X}}, \end{aligned}$$

resulting in ten different terms. The terms IV, VII, VIII, and X are mechanical in nature. Term IV describes direct readout, terms VII and VIII describe rectification and $2\omega_d$ readout, term VIII describes two-source gate mixing, and term X describes two-source and FM mixing. The other terms, which are electrical in nature, can dominate the mechanical signal. For direct readout, term III is important; for rectification, terms I and VI are important; for 2ω readout and two-source gate mixing, term VI is important; and for two-source mixing, term IX is important. It should be noted that the terms IX and X describe mixing as laid out earlier only when $dI/dV_b = G$. In other cases, an expression should be obtained by multiplying $V_b^{dc}+\delta V_b$ with the expansion of the conductance, G, with respect to gate voltage.

The second contribution to the current is due to changes in capacitance as the CNT moves towards and away from the gate electrode, with a displacement $\delta u = u_{ac}\cos(\omega t)$. It is given by:

$$I_{cap} = -i\omega \frac{dC_g}{du} V_g^{dc} \delta u. \tag{2.11}$$

Thirdly, when an oscillating voltage is applied to the gate electrode it creates crosstalk as the applied signal leaks onto the drain. The generated current depends on the capacitance between the gate and drain, $C_{crosstalk}$, and is given by:

$$I_{crosstalk} = i\omega_d C_{crosstalk} \delta V_g^{elec}. \tag{2.12}$$

Tables 2.1 and 2.2 summarize the eight chosen electrical methods, showing the frequency and expression of the ac and dc voltages applied to the source and gate, of the measured electrical and mechanical current, and of the ac force acting on the CNT mechanical resonator, together with the origins of the measured electrical and mechanical current. Using the expressions in the tables, the amplitude of oscillation, u_{ac}, can be calculated for each readout scheme from the mechanical current, I_{mech}.

To decide which detection scheme to use, there are three main factors to take into account. The first factor is the occurrence of Coulomb blockade and associated Coulomb peaks. In general, Coulomb peaks yield a high d^2I/dV_g^2, making rectification, two-source gate mixing and $2\omega_d$ readout attractive schemes. The second factor is the bandwidth of the measurement system. For measurement systems with a bandwidth lower than the mechanical resonance frequency, down-mixing schemes such as two-source mixing, FM mixing, and two-source gate mixing become attractive, along with the rectification technique. The third factor is the occurrence of crosstalk between the gate and the drain. To avoid crosstalk by measuring at a different frequency than the applied gate voltage, the techniques of parametric drive, $2\omega_d$ excitation, and $2\omega_d$ readout are useful. For a system with a high dI/dV_g, large bandwidth, and small crosstalk, the direct readout scheme should be chosen, as it is the most straightforward in design and holds the least limitations in the measurements that can be performed.

Measurement technique	Source terminal	Gate terminal	I_{mech}	I_{elec}	$F_{ac}/(dC_g/du)$
	ω	ω	ω		ω
			term	term	
	expression	expression	amplitude at ω	amplitude at ω	expression
two-source mixing	$\omega_d + \Delta\omega$	dc & ω_d	$\Delta\omega$		ω_d
			X	IX	
	$V_b^{ac}\cos((\omega_d + \Delta\omega)t)$	$V_g^{dc} + V_g^{ac}\cos(\omega_d t)$	$\frac{d^2 I}{dV_g dV_b} V_b^{ac} \frac{V_g^{dc}}{C_g} \frac{dC_g}{du} u_{ac}$	$\frac{d^2 I}{dV_g dV_b} V_b^{ac} V_g^{ac}$	$V_g^{dc} V_g^{ac}\cos(\omega_d t)$
FM mixing	$\{\omega_d + n\Delta\omega\}$ (Fig. 2.6)	dc	$\Delta\omega$		ω_d
			X	-	
	$V_b^{FM}(t)$ (Eq. 2.2)	V_g^{dc}	$\frac{1}{2}\frac{d^2 I}{dV_g dV_b} V_b^{ac} \frac{V_g^{dc}}{C_g}$ $\times \frac{dC_g}{du}\omega_\Delta \frac{\partial}{\partial\omega_d}\mathrm{Re}(u_{ac})$	-	$-\frac{C_s}{C_{tot}} V_g^{dc} V_b^{ac}\cos(\omega_d t)$
rectification	dc	dc & ω_d	dc		ω_d
			VII & VIII	I & VI	
	V_b^{dc}	$V_g^{dc} + V_g^{ac}\cos(\omega_d t)$	$\frac{1}{4}\frac{d^2 I}{dV_g^2}\left(\frac{V_g^{dc}}{C_g}\frac{dC_g}{du}\right)^2 u_{ac}^2$ $+\frac{1}{2}\frac{d^2 I}{dV_g^2}\frac{V_g^{dc}}{C_g}\frac{dC_g}{du} V_g^{ac} u_{ac}$	$I(V_g^{dc}, V_b^{dc})$ $+\frac{1}{4}\frac{d^2 I}{dV_g^2}\left(V_g^{ac}\right)^2$	$V_g^{dc} V_g^{ac}\cos(\omega_d t)$
direct readout	dc	dc & ω_d	ω_d		ω_d
			IV & cap	III & crosstalk	
	V_b^{dc}	$V_g^{dc} + V_g^{ac}\cos(\omega_d t)$	$\frac{dI}{dV_g}\frac{V_g^{dc}}{C_g}\frac{dC_g}{du} u_{ac}$ $-i\omega_d V_g^{dc}\frac{dC_g}{du} u_{ac}$	$\frac{dI}{dV_g} V_g^{ac}$ $+i\omega_d C_{tot} V_g^{ac}$	$V_g^{dc} V_g^{ac}\cos(\omega_d t)$

TABLE 2.1: Summary of the eight electrical detection methods as described in the text. The origin of the mechanical and electrical current is denoted by a roman numeral corresponding to the term in Eq. 2.11, by "cap" for I_{cap} in Eq. 2.11, or by "crosstalk" for $I_{crosstalk}$ in Eq. 2.12.

Measurement technique	Source terminal	Gate terminal	I_{mech}	I_{elec}	$F_{ac}/(dC_g/du)$
	ω	ω	ω		ω
			term	term	
	expression	expression	amplitude at ω	amplitude at ω	expression
two-source gate mixing	dc	dc & ω_d & $\omega_d+\Delta\omega$	$\Delta\omega$		ω_d & $\omega_d+\Delta\omega$
	V_b^{dc}	$V_g^{dc}+V_{g,d}^{ac}\cos(\omega_d t)+$ $V_{g,p}^{ac}\cos((\omega_d+\Delta\omega)t)$	VIII	VI	$V_g^{dc}V_{g,d}^{ac}\cos(\omega_d t)+$ $V_g^{dc}V_{g,p}^{ac}\cos((\omega_d+\Delta\omega)t)$
			$\frac{d^2I}{dV_g^2}V_{g,p}^{ac}\frac{V_g^{dc}}{C_g}\frac{dC_g}{du}u_{ac}$ or $\frac{d^2I}{dV_g^2}V_{g,d}^{ac}\frac{V_g^{dc}}{C_g}\frac{dC_g}{du}u_{ac}$	$\frac{d^2I}{dV_g^2}V_{g,p}^{ac}V_{g,d}^{ac}$	
parametric excitation	dc	dc & $2\omega_d$	ω_d		$2\omega_d$
	V_b^{dc}	$V_g^{dc}+V_g^{ac}\cos(2\omega_d t)$	IV & cap	-	$V_g^{dc}V_g^{ac}\cos(2\omega_d t)$
			$\frac{dI}{dV_g}\frac{V_g^{dc}}{C_g}\frac{dC_g}{du}u_{ac}$ $-i\omega_d V_g^{dc}\frac{dC_g}{du}u_{ac}$	-	
$2\omega_d$ excitation	dc	dc & ω_d	$2\omega_d$		$2\omega_d$
	V_b^{dc}	$V_g^{dc}+V_g^{ac}\cos(\omega_d t)$	IV & cap	-	$\frac{1}{2}\left(V_g^{ac}\right)^2\cos(2\omega_d t)$
			$\frac{dI}{dV_g}\frac{V_g^{dc}}{C_g}\frac{dC_g}{du}u_{ac}$ $-i2\omega_d V_g^{dc}\frac{dC_g}{du}u_{ac}$	-	
$2\omega_d$ readout	dc	dc & ω_d	$2\omega_d$		ω_d
	V_b^{dc}	$V_g^{dc}+V_g^{ac}\cos(\omega_d t)$	VII & VIII	VI	$V_g^{dc}V_g^{ac}\cos(\omega_d t)$
			$\frac{1}{4}\frac{d^2I}{dV_g^2}\left(\frac{V_g^{dc}}{C_g}\frac{dC_g}{du}\right)^2u_{ac}^2$ $+\frac{1}{2}\frac{d^2I}{dV_g^2}\frac{V_g^{dc}}{C_g}\frac{dC_g}{du}V_g^{ac}u_{ac}$	$\frac{1}{4}\frac{d^2I}{dV_g^2}\left(V_g^{ac}\right)^2$	

TABLE 2.2: Continued from the previous page. $V_{g,d}^{ac}$ and $V_{g,p}^{ac}$ refer to the exchangeable drive (d) and probe (p) ac gate voltages.

REFERENCES

[1] H. B. Meerwaldt, G. A. Steele, and H. S. J. van der Zant, *Fluctuating Nonlinear Oscillators* (Oxford University Press, 2012), chap. Carbon nanotubes: Nonlinear high-Q resonators with strong coupling to single-electron tunneling, pp. 312–340, URL `http://arxiv.org/abs/1205.4921`.

[2] S. Sapmaz, J. P. Herrero, Y. M. Blanter, C. Dekker, and H. S. J. van der Zant, *Tunneling in Suspended Carbon Nanotubes Assisted by Longitudinal Phonons*, Physical Review Letters **96**, 026801 (2006).

[3] R. Leturcq, C. Stampfer, K. Inderbitzin, L. Durrer, C. Hierold, E. Mariani, M. G. Schultz, F. von Oppen, and K. Ensslin, *Franck-Condon blockade in suspended carbon nanotube quantum dots*, Nature Physics **5**, 327 (2009).

[4] A. K. Hüttel, B. Witkamp, M. Leijnse, M. R. Wegewijs, and H. S. J. van der Zant, *Pumping of Vibrational Excitations in the Coulomb-Blockade Regime in a Suspended Carbon Nanotube*, Physical Review Letters **102**, 225501 (2009).

[5] B. LeRoy, S. Lemay, J. Kong, and C. Dekker, *Electrical generation and absorption of phonons in carbon nanotubes*, Nature **432**, 371 (2004).

[6] L. Vitali, M. Burghard, M. Schneider, L. Liu, S. Wu, C. Jayanthi, and K. Kern, *Phonon spectromicroscopy of carbon nanostructures with atomic resolution*, Physical Review Letters **93**, 136103 (2004).

[7] S. Sawano, T. Arie, and S. Akita, *Carbon nanotube resonator in liquid*, Nano Letters **10**, 3395 (2010).

[8] S. Stapfner, L. Ost, D. Hunger, E. Weig, J. Reichel, and I. Favero, *Cavity-enhanced optical detection of carbon nanotube Brownian motion* (2012), URL `http://arxiv.org/abs/1211.1608`.

[9] D. Garcia-Sanchez, A. S. Paulo, M. J. Esplandiu, F. Perez-Murano, L. Forro, A. Aguasca, and A. Bachtold, *Mechanical detection of carbon nanotube resonator vibrations*, Physical Review Letters **99**, 085501 (2007).

[10] P. Poncharal, Z. L. Wang, D. Ugarte, and W. A. de Heer, *Electrostatic deflections and electromechanical resonances of carbon nanotubes*, Science **283**, 1513 (1999).

[11] K. Jensen, J. Weldon, H. Garcia, and A. Zettl, *Nanotube radio*, Nano Letters **7**, 3508 (2007).

[12] S. Perisanu, T. Barois, A. Ayari, P. Poncharal, M. Choueib, S. T. Purcell, and P. Vincent, *Beyond the linear and Duffing regimes in nanomechanics: Circularly polarized mechanical resonances of nanocantilevers*, Physical Review B **81**, 165440 (2010).

[13] B. Reulet, A. Y. Kasumov, M. Kociak, R. Deblock, I. Khodos, Y. B. Gorbatov, V. Volkov, C. Journet, and H. Bouchiat, *Acoustoelectric effects in carbon nanotubes*, Physical Review Letters **85**, 2829 (2000).

[14] V. Sazonova, Y. Yaish, H. Ustunel, D. Roundy, T. A. Arias, and P. L. McEuen, *A tunable carbon nanotube electromechanical oscillator*, Nature **431**, 284 (2004).

[15] H. B. Peng, C. W. Chang, S. Aloni, T. D. Yuzvinsky, and A. Zettl, *Ultrahigh frequency nanotube resonators.*, Physical Review Letters **97**, 087203 (2006).

[16] B. Witkamp, M. Poot, and H. S. J. van der Zant, *Bending-mode vibration of a suspended nanotube resonator*, Nano Letters **6**, 2904 (2006).

[17] B. Lassagne, D. Garcia-Sanchez, A. Aguasca, and A. Bachtold, *Ultrasensitive mass sensing with a nanotube electromechanical resonator*, Nano Letters **8(11)**, 3735 (2008).

[18] V. Gouttenoire, T. Barois, S. Perisanu, J. L. Leclercq, S. T. Purcell, P. Vincent, and A. Ayari, *Digital and FM Demodulation of a Doubly Clamped Single-Walled Carbon-Nanotube Oscillator: Towards a Nanotube Cell Phone*, Small **6**, 1060 (2010).

[19] A. K. Hüttel, G. A. Steele, B. Witkamp, M. Poot, L. P. Kouwenhoven, and H. S. J. van der Zant, *Carbon Nanotubes as Ultrahigh Quality Factor Mechanical Resonators*, Nano Letters **9**, 2547 (2009).

[20] C. W. J. Beenakker, *Theory Of Coulomb-Blockade Oscillations In The Conductance Of A Quantum Dot*, Physical Review B **44**, 1646 (1991).

[21] J. M. Thijssen and H. S. J. Van der Zant, *Charge transport and single-electron effects in nanoscale systems*, Physica Status Solidi B-Basic Solid State Physics **245**, 1455 (2008).

[22] B. Schneider, S. Etaki, H. van der Zant, and G. Steele, *Coupling carbon nanotube mechanics to a superconducting circuit*, Scientific Reports **2**, 599 (2012).

[23] Y. Xu, C. Chen, V. V. Deshpande, F. A. DiRenno, A. Gondarenko, D. B. Heinz, S. Liu, P. Kim, and J. Hone, *Radio frequency electrical transduction of graphene mechanical resonators*, Applied Physics Letters **97**, 243111 (2010).

[24] T. S. Abhilash, J. P. Mathew, S. Sengupta, M. Gokhale, A. Bhattacharya, and M. M. Deshmukh, *Wide Bandwidth Nanowire Electromechanics on Insulating Substrates at Room Temperature*, Nano Letters **12**, 6432 (2012).

[25] A. Eichler, J. Chaste, J. Moser, and A. Bachtold, *Parametric Amplification and Self-Oscillation in a Nanotube Mechanical Resonator*, Nano Letters **11**, 2699 (2011).

3

STRONG COUPLING BETWEEN SINGLE-ELECTRON TUNNELING AND NANOMECHANICAL MOTION

G. A. Steele, A. K. Hüttel, B. Witkamp, M. Poot, H. B. Meerwaldt, L. P. Kouwenhoven, and H. S. J. van der Zant

We study a high-quality mechanical resonator made from a suspended carbon nanotube driven into motion by a periodic RF source and by single-electron charge fluctuations. The high quality-factor exceeding 10^5 *allows the detection of a shift in resonance frequency due to the addition of a single electron charge on the nanotube. As a function of d.c. gate voltage, we observe single-electron tuning oscillations as a mechanical analogue of electrical single-electron tunneling oscillations. The mechanical motion and electron tunneling are strongly coupled, as observed by frequency shifts induced by single-electron charge fluctuations, energy transfer to the electrons causing mechanical damping, and qualitatively new nonlinear behaviour. Strikingly, we also discover that a d.c. current through the nanotube spontaneously drives the mechanical resonator, exerting a force that is coherent with the high-frequency resonant mechanical motion.*

This Chapter has been published in Science **325**, 1103-1107 (2009) [1].

Nanomechanical systems [2, 3] have promising applications, such as ultrasensitive mass detection [4–6]. The combination of a high resonance frequency and a small mass also makes nanomechanical resonators attractive for a fundamental study of mechanical motion in the quantum limit [7–10]. For a successful observation of quantum motion of a macroscopic object, it is required to have a resonator with a high resonance frequency (which translates to nanoscale dimensions), low dissipation (implying a high quality-factor), and a sensitive detector with minimum back-action (i.e. quantum limited) [11, 12]. Here, we demonstrate a dramatic backaction that strongly couples a quantum dot detector to the resonator dynamics, and which, in the limit of strong feedback, spontaneously excites large-amplitude resonant mechanical motion.

Nanomechanical resonators have been realized by etching a large structure down to nanometer dimensions. In small devices, however, surfaces effects impose a limit on the quality-factor [3]. Alternatively, suspended nanotubes can be used to avoid surface damage from the (etching) fabrication process. We recently developed a mechanical resonator based on an ultra-clean carbon nanotube with high resonance frequencies of several 100 MHz and a record quality-factor exceeding 10^5 [13]. Here, we exploit this new resonator to explore an unprecedented coupling regime between single-electron tunneling and nanomechanical motion. We follow pioneering approaches using aluminium single-electron transistors as position detectors [7–9] and AFM cantilevers as resonators [14–16]; however, our experiment is in the limit of much stronger electromechanical coupling, achieved by embedding a quantum dot detector in the nanomechanical resonator itself.

3.1 DEVICE FABRICATION, MECHANICAL CHARACTERISTICS, AND DETECTION

Our device consists of a nanotube suspended across a trench, making electrical contact to two metal electrodes (Fig. 3.1A and B). Electrons are confined in the nanotube by Schottky barriers at the Pt metal contacts, forming a quantum dot in the suspended segment. The nanotube growth is the last step in the fabrication process, yielding ultra-clean devices [17], as demonstrated by the four-fold shell-filling of the Coulomb peaks (Fig. 3.1C). The measurements are all performed at a temperature of 20 mK with an electron temperature of ~80 mK.

We actuate the resonator with a nearby antenna, and detect the resonator motion by its influence on the d.c. current through the nanotube. The inset to Fig. 3.1D shows a peak in the current at the resonance frequency, which we have identified as a bending-mode mechanical resonance of the nanotube [13]. The quality factor (Q-factor) typically exceeds 10^5, which is an increase of more than two orders of magnitude compared to previous nanotube studies [5, 18, 19]. The res-

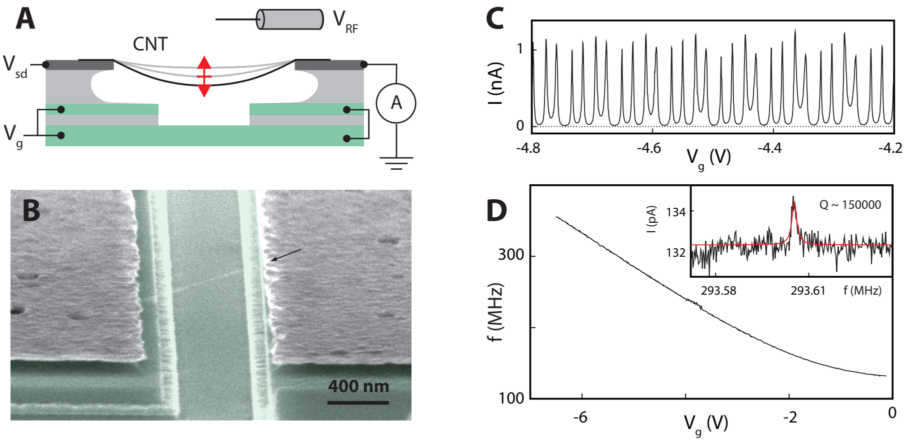

FIGURE 3.1: A high quality-factor nanotube mechanical resonator with an embedded quantum dot. (A) Device layout. A suspended carbon nanotube is excited into mechanical motion by applying an a.c. voltage to a nearby antenna. A d.c. current through the nanotube detects the motion. (B) SEM image of a typical device. (C) A quantum dot, formed between Schottky barriers at the metal contacts, displays 4-fold shell filling of holes. (D) Inset: the mechanical resonance induces a corresponding resonance in the d.c. current which can have a narrow linewidth with quality-factors up to 150 000. Main plot: the resonance frequency can be tuned using a tensioning force from the d.c. voltage on the gate.

onance frequency is tuned by more than a factor 2 with gate voltage (Fig. 3.1D). Here, the electric field due to the gate voltage pulls the nanotube towards the gate, lengthening it and inducing more tension, similar to the tuning of a guitar string [18].

Our detection signal results from a change in gate capacitance, ΔC_g, during a displacement of the nanotube. This changes the effective quantum dot potential and, if positioned initially beside a Coulomb peak (Fig. 3.1C), can move it onto the peak, thereby increasing the current. For a nanotube oscillating on resonance, the effective potential oscillates, and due to the nonlinearity of Coulomb blockade, is rectified to a detectable d.c. current.

3.2 SINGLE-ELECTRON TUNING AND BACKACTION

The narrow linewidth of the resonance peak due to the high Q-factor provides an unprecedented sensitive probe for studying nanomechanical motion. We first show the influence of a single electron on the resonance frequency, f_0. The Coulomb oscillations in Fig. 3.2A are due to single-electron tunneling, giving rise to current peaks and Coulomb blockade, fixing the electron number in the valleys. From valley to valley, the electron number changes by one. Fig. 3.2B shows the mechanical resonance signal recorded at the same time. Overall, a more negative gate voltage (right to left) increases the total charge on the nanotube, increasing the tension. This stiffens the mechanical spring constant and increases the resonance frequency. Linear stiffening occurs in the Coulomb valleys (indicated with dashed lines), whereas at Coulomb peaks, a peculiar softening occurs, visible as dips in f_0.

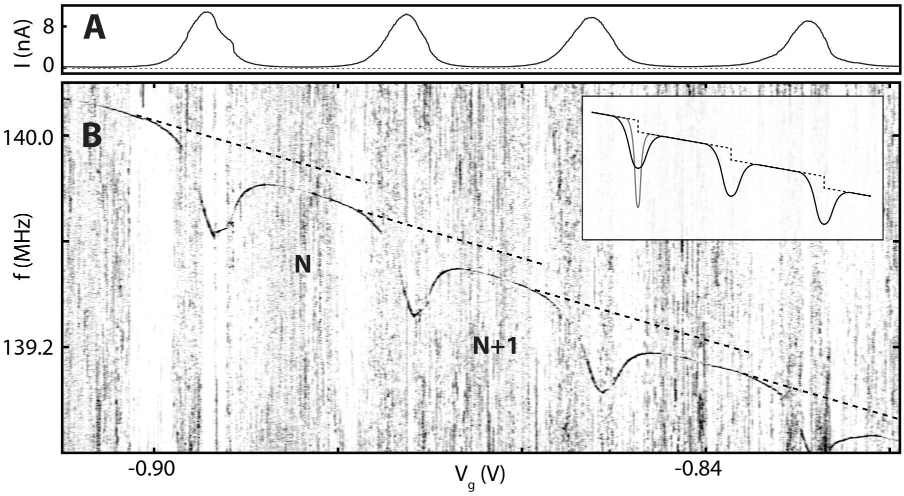

FIGURE 3.2: Single-electron tuning. (A) Nanotube current vs. gate voltage showing single-electron tunneling at the peaks and Coulomb blockade in the valleys. This curve is taken from (B) at f = 138.8 MHz. (B) Normalized resonance signal $\Delta I/\Delta I_{peak}$ vs. RF frequency and gate voltage (V_{sd} = 1.5 mV). The tuned mechanical resonance shows up as the darker curve with dips at the Coulomb peaks. The offsets between dashed lines indicate the frequency shift due to the addition of one electron to the nanotube. The resonance frequency also shows dips caused by a softening of the spring constant due to single-electron charge fluctuations. The inset illustrates the expected resonance behavior (see text).

We first focus on the change in resonance frequency due to the addition of one electron, which is measured as offsets of about 0.1 MHz between the dashed lines. This shift from *single-electron tuning*, predicted in [20], is about 20 times our linewidth and thus resolvable for the first time in a nanomechanical system. Since we compare valleys with a fixed electron number, this single-electron tuning comes from a change in a static force on the nanotube. The (electro)static force is proportional to the square of the charge on the nanotube and thus adding one electron charge results, here, in a detectable shift in the mechanical resonance [20]. The shifts from single-electron tuning can be as large as 0.5 MHz, more than 100 times the linewidth.

Next, we focus on the dips in resonance frequency that occur at the Coulomb peaks. The current at the Coulomb peaks is carried by single-electron tunneling, meaning that one electron tunnels off the nanotube before the next electron can enter the nanotube. The charge on the nanotube thus fluctuates by exactly one electron charge, e, with a time dynamics understood in detail by the theory of Coulomb blockade [21]. The average rate, Γ, at which an electron moves across the tube can be read off from the current $I = e\Gamma$ (1.6 pA corresponds to a 10 MHz rate). Moving the gate voltage off or on a Coulomb peak, we can tune the rate from the regime $\Gamma \sim f_0$ to $\Gamma \gg f_0$ and explore the different effects on the mechanical resonance.

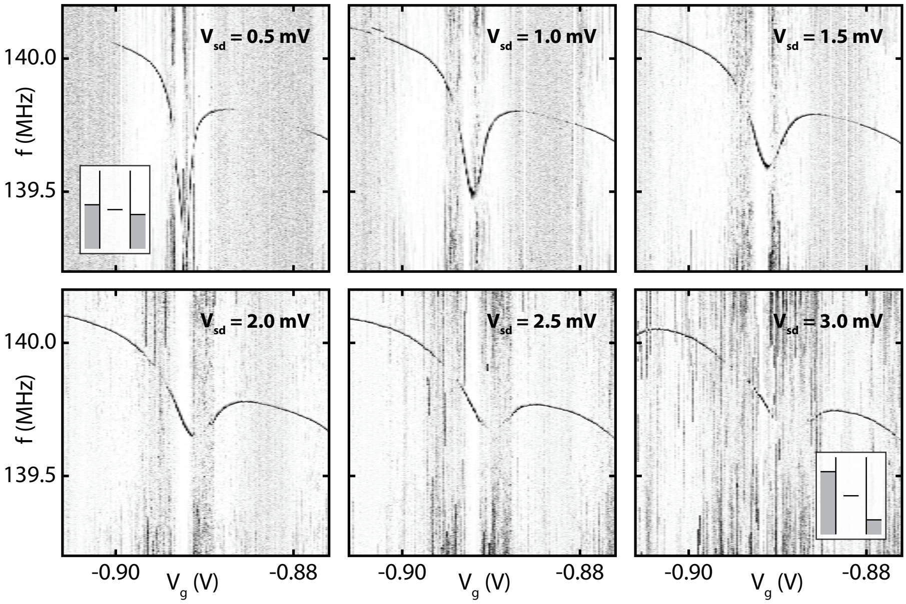

FIGURE 3.3: Single electron tuning: zoom on one frequency dip for various source-drain voltages, V_{sd}, showing dip broadening for increasing V_{sd}. The two insets illustrate the energy diagrams for small and large V_{sd}.

In Figs. 3.2A,B the Coulomb peak values of ~8 nA yield $\Gamma \sim 300 f_0$, the regime of many single-electron tunneling events per mechanical oscillation. In addition to the static force and the RF oscillating driving force, single-electron tunneling now exerts a time-fluctuating, dynamic force on the mechanical resonator. We observe that this dynamic force causes softening, giving dips in the resonance frequency. The single-electron charge fluctuations do not simply smooth the stepwise transition from the static single-electron tuning shifts. Strikingly, we find that fluctuations instead cause dips in the resonant frequency up to an order of magnitude larger than the single electron tuning shifts. As shown in [14, 22] and discussed in detail in Ch. 4, the dynamic force modifies the nanotube's spring constant, k, resulting in a softening of the mechanical resonance. The shape of the frequency dip can be altered by applying a finite bias, V_{sd}, across the nanotube. Fig. 3.3 shows that, starting from deep and narrow at small $V_{sd} = 0.5$ mV, the dip becomes shallower and broader on increasing V_{sd}. This dip-shape largely resembles the broadening of Coulomb blockade peaks when increasing V_{sd}. We thus conclude from Fig. 3.3 that the *single-electron tuning oscillations* are a mechanical effect that is a direct consequence of single-electron tunneling oscillations.

3.3 SINGLE-ELECTRON DAMPING AND NONLINEARITY

Besides softening, the charge fluctuations also provide a channel for dissipation of mechanical energy. Fig. 3.4A shows the resonance dip for small RF power with linecuts in Fig. 3.4B. In the Coulomb valleys, tunneling is suppressed ($\Gamma \sim f_0$), damping of the mechanical motion is minimized, and we observe the highest quality-factors. On a Coulomb peak, charge fluctuations are maximal ($\Gamma \gg f_0$), and the quality-factor decreases to a few thousand. These results explicitly show that detector backaction can cause significant mechanical damping. The underlying mechanism for the damping is an energy transfer occasionally occurring when a current-carrying electron is pushed up to a higher (electrostatic) energy by the nanotube motion before tunneling out of the dot. This gain in potential energy is later dissipated in the drain contact.

If we drive the system at higher RF powers (Fig. 3.4C,D), we observe an asymmetric resonance peak, along with distinct hysteresis between upward and downward frequency sweeps. Theoretically, this marks the onset of nonlinear terms in the equation of motion, such as in the well-studied Duffing oscillator [23, 24]. The spring constant, k, is modified, due to a large oscillation amplitude, x, which is accounted for by replacing k with $(k+\alpha x^2)$. The time-averaged spring constant increases if $\alpha > 0$, which is accompanied by a sharp edge at the high frequency side of the peak; vice versa for $\alpha < 0$. In addition to the overall softening of k yielding the frequency dips of Fig. 3.2, the fluctuating charge on the dot also changes α, giving a softening spring ($\alpha < 0$) outside of the frequency dip (Coulomb valleys), and a hardening spring ($\alpha > 0$) inside the frequency dip (Coulomb peaks), shown in Fig. 3.4. The sign of α follows the curvature of $f_0(V_g)$ induced by the fluctuating electron force, giving a change in sign at the inflection point of the frequency dip. Interestingly, nonlinearity from the single-electron force in our device dominates, and is much stronger than that from the mechanical deformation (see Ch. 6 for

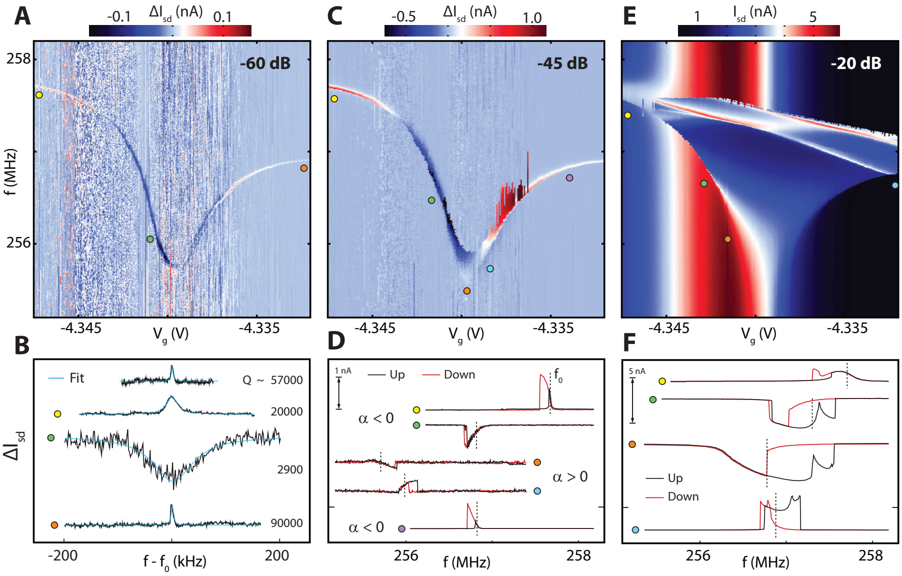

FIGURE 3.4: Lineshapes of the mechanical resonance from linear to nonlinear driving regimes. (A) Detector current, ΔI, vs. frequency and gate voltage at RF excitation power of -60 dB as the gate voltage is swept through one Coulomb peak. (B) Fits of the resonance to a squared Lorentzian lineshape at different gate voltages [13]. The RF power for each trace is adjusted to stay in the linear driving regime (-75,-64,-52, and -77 dB top to bottom). Traces are taken at the positions indicated by colored circles (aside from the top trace which is taken at V_g = -4.35 V). (C) At -45 dB, the resonance has an asymmetric lineshape with one sharp edge, see linecuts (D), typical for a nonlinear oscillator [23, 24]. Dashed lines in (D) and (F) indicate the resonance frequency f_0 at low powers. (E) and (F) At even higher driving powers (-20 dB), the mechanical resonator displays sharp sub-peaks and several jumps in amplitude when switching between different stable modes. (C) and (E) are taken in the upwards sweep direction.

further discussion).

Figs. 3.4E,F show the regime of further enhanced RF driving. The nonlinearity is now no longer a perturbation of the spring constant, but instead gives sharp peaks in the lineshape and switching between several different metastable modes. At this strong driving, we observe very rich nonlinear mechanical behavior due to the coupling of the resonator motion to the quantum dot.

3.4 SINGLE-ELECTRON SELF-SUSTAINED OSCILLATION

The question of whether a fluctuating driving force from electron tunneling alone can excite the mechanical resonance is addressed in Fig. 3.5 with a standard Coulomb-blockade measurement shown in A. Mechanical effects in Coulomb diamonds have been studied before in the form of phonon sidebands of electronic transitions [25–28]. New in the data of Fig. 3.5 are reproducible ridges of positive and negative spikes in the differential conductance as indicated by arrows. This instability has been seen in all 12 measured devices with clean suspended nanotubes and never in non-suspended devices. Fig. 3.5B and C shows such ridges in a second device, visible both as spikes in the differential conductance (Fig. 3.5B), and as discrete jumps in the current (Fig. 3.5C). The barriers in device 2 were highly tunable: we find that the switch-ridge can be suppressed by reducing the tunnel rate to the source-drain contacts, thereby decreasing the current. The instability disappears roughly when the tunnel rate is decreased below the mechanical resonance frequency.

In a model predicting such instabilities [29], positive feedback from single-electron tunneling excites the mechanical resonator into a large amplitude oscillation. The theory predicts a characteristic shape of the switch-ridges and the suppression of the ridges for $\Gamma \sim f_0$, in striking agreement with our observations. If the required positive feedback is present, however, it should also have a mechanical signature: such a signature is indeed observed in Fig. 3.5E. The RF-driven mechanical resonance experiences a dramatic perturbation triggered by the switch-ridge discontinuities in the Coulomb peak current shown in Fig. 3.5D. At the position of the switch, the resonance peak shows a sudden departure from the expected frequency dip (dashed line), and becomes strongly asymmetric and broad, as if driven by a much higher RF power. This is indeed the case, but the driving power is now provided by an internal source: due to strong feedback, the fluctuating force from single-electron tunneling becomes a driving force coherent with the mechanical oscillation. Remarkably, the d.c. current through the quantum dot can be used both to detect the high-frequency resonance and, in the case of strong feedback, directly excite resonant mechanical motion.

Acknowledgements: We thank Y. M. Blanter and Y. V. Nazarov for helpful discussions. This work was supported by the Dutch Organization for Fundamental Research on Matter (FOM), the Netherlands Organization for Scientific Research (NWO) (L.P.K. Spinoza and H.S.J.Z. Vici), the Nanotechnology Network Netherlands (NanoNed), and the Japan Science and Technology Agency International Cooperative Research Project (JST-ICORP).

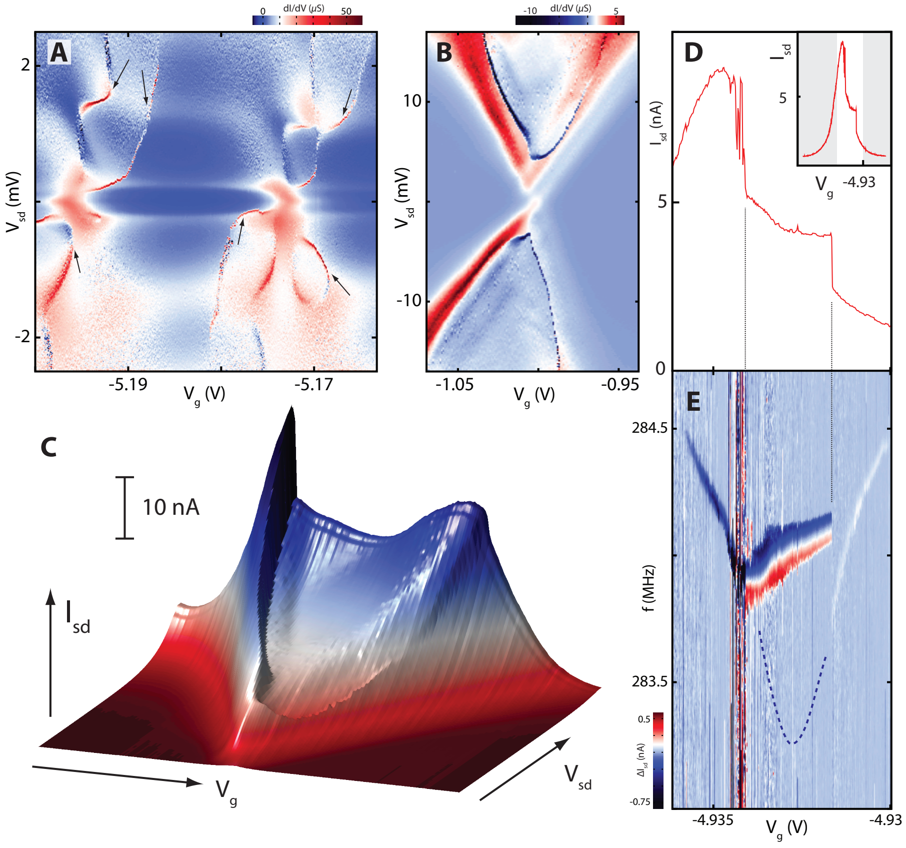

FIGURE 3.5: Spontaneous driving of the mechanical resonance by single-electron tunneling. (A) Differential conductance, dI/dV_{sd}, showing ridges of sharp positive (deep red) and negative (deep blue) spikes (arrows). (B) Similar ridges measured on device 2 (trench width = 430 nm) in the few-hole regime (4hole to 3hole transition). Spikes in dI/dV_{sd} appear as step-like ridges in current: (C) shows the data from the upper half of (B), but now as a 3D current plot. Note that the ridges are entirely reproducible. (D) Inset: Coulomb peak at V_{sd} = 0.5 mV showing large switching-steps. Main plot: zoom-in on data from inset. (E) RF-driven mechanical resonance measured for the same Coulomb peak in (D) at a driving power of -50 dB. Outside the “switch-region”, the resonance has a narrow lineshape and follows the softening-dip from Figs. 3.2, 3.3, and 3.4. At the first switch, the resonance position departs from the expected position (indicated by the dashed line). The mechanical signal is strongly enhanced in amplitude and displays a broad asymmetric lineshape. At the second switch, the resonance returns to the frequency and narrow lineshape expected at these powers.

REFERENCES

[1] G. A. Steele, A. K. Hüttel, B. Witkamp, M. Poot, H. B. Meerwaldt, L. P. Kouwenhoven, and H. S. J. van der Zant, *Strong Coupling Between Single-Electron Tunneling and Nanomechanical Motion*, Science **325**, 1103 (2009).

[2] H. G. Craighead, *Nanoelectromechanical Systems*, Science **290**, 1532 (2000).

[3] K. L. Ekinci and M. L. Roukes, *Nanoelectromechanical systems*, Review of Scientific Instruments **76**, 061101 (2005).

[4] K. L. Ekinci, X. M. H. Huang, and M. L. Roukes, *Ultrasensitive nanoelectromechanical mass detection*, Applied Physics Letters **84**, 4469 (2004).

[5] B. Lassagne, D. Garcia-Sanchez, A. Aguasca, and A. Bachtold, *Ultrasensitive Mass Sensing with a Nanotube Electromechanical Resonator*, Nano Letters **8**, 3735 (2008).

[6] H.-Y. Chiu, P. Hung, H. W. Postma, and M. Bockrath, *Atomic-Scale Mass Sensing Using Carbon Nanotube Resonators*, Nano Letters **8**, 4342 (2008).

[7] R. G. Knobel and A. N. Cleland, *Nanometre-scale displacement sensing using a single electron transistor*, Nature **424**, 291 (2003).

[8] M. D. Lahaye, O. Buu, B. Camarota, and K. C. Schwab, *Approaching the Quantum Limit of a Nanomechanical Resonator*, Science **304**, 74 (2004).

[9] A. Naik, O. Buu, M. D. Lahaye, A. D. Armour, A. A. Clerk, M. P. Blencowe, and K. C. Schwab, *Cooling a nanomechanical resonator with quantum backaction*, Nature **443**, 193 (2006), ISSN 0028-0836.

[10] K. C. Schwab and M. L. Roukes, *Putting Mechanics into Quantum Mechanics*, Physics Today **58**, 36 (2005).

[11] C. M. Caves, K. S. Thorne, R. W. Drever, V. D. Sandberg, and M. Zimmermann, *On the measurement of a weak classical force coupled to a quantum-mechanical oscillator. I. Issues of principle*, Reviews of Modern Physics **52**, 341 (1980).

[12] C. A. Regal, J. D. Teufel, and K. W. Lehnert, *Measuring nanomechanical motion with a microwave cavity interferometer*, Nature Physics **4**, 555 (2008).

[13] A. K. Hüttel, G. A. Steele, B. Witkamp, M. Poot, L. P. Kouwenhoven, and H. S. J. van der Zant, *Carbon Nanotubes as Ultrahigh Quality Factor Mechanical Resonators*, Nano Letters **9**, 2547 (2009).

[14] M. T. Woodside and P. L. McEuen, *Scanned Probe Imaging of Single-Electron Charge States in Nanotube Quantum Dots*, Science **296**, 1098 (2002).

[15] J. Zhu, M. Brink, and P. L. McEuen, *Frequency shift imaging of quantum dots with single-electron resolution*, Applied Physics Letters **87** (2005).

[16] R. Stomp, Y. Miyahara, S. Schaer, Q. Sun, H. Guo, P. Grutter, S. Studenikin, P. Poole, and A. Sachrajda, *Detection of Single-Electron Charging in an Individual InAs Quantum Dot by Noncontact Atomic-Force Microscopy*, Physical Review Letters **94**, 056802 (2005).

[17] G. A. Steele, G. Gotz, and L. P. Kouwenhoven, *Tunable few-electron double quantum dots and Klein tunnelling in ultraclean carbon nanotubes*, Nature Nanotechnology **4**, 363 (2009).

[18] V. Sazonova, Y. Yaish, H. Ustunel, D. Roundy, T. A. Arias, and P. L. McEuen, *A tunable carbon nanotube electromechanical oscillator*, Nature **431**, 284 (2004).

[19] B. Witkamp, M. Poot, and H. S. J. van der Zant, *Bending-Mode Vibration of a Suspended Nanotube Resonator*, Nano Letters **6**, 2904 (2006).

[20] S. Sapmaz, Y. Blanter, L. Gurevich, and H. S. J. van der Zant, *Carbon nanotubes as nanoelectromechanical systems*, Physical Review B **67**, 235414 (2003).

[21] C. W. J. Beenakker, *Theory of Coulomb-blockade oscillations in the conductance of a quantum dot*, Physical Review B **44**, 1646 (1991).

[22] M. Brink, thesis, Cornell Univerity (2007).

[23] A. Cleland, *Foundations of Nanomechanics* (Springer-Verlag, 2002).

[24] A. H. Nayfeh and D. T. Mook, *Nonlinear Oscillations* (Wiley, 1979).

[25] H. Park, J. Park, A. K. Lim, E. H. Anderson, P. A. Alivisatos, and P. L. McEuen, *Nanomechanical oscillations in a single-C60 transistor*, Nature **407**, 57 (2000).

[26] S. Sapmaz, J. P. Herrero, Ya, C. Dekker, and H. S. J. van der Zant, *Tunneling in Suspended Carbon Nanotubes Assisted by Longitudinal Phonons*, Physical Review Letters **96** (2006).

[27] F. A. Zwanenburg, C. E. van Rijmenam, Y. Fang, C. M. Lieber, and L. P. Kouwenhoven, *Spin States of the First Four Holes in a Silicon Nanowire Quantum Dot*, Nano Letters **9**, 1071 (2009).

[28] R. Leturcq, C. Stampfer, K. Inderbitzin, L. Durrer, C. Hierold, E. Mariani, M. G. Schultz, F. von Oppen, and K. Ensslin, *Franck-Condon blockade in suspended carbon nanotube quantum dots*, Nature Physics **5**, 327 (2009).

[29] O. Usmani, Y. M. Blanter, and Y. V. Nazarov, *Strong feedback and current noise in nanoelectromechanical systems*, Physical Review B **75**, 195312 (2007).

4

PROBING THE CHARGE OF A QUANTUM DOT WITH A NANOMECHANICAL RESONATOR

H. B. Meerwaldt, G. Labadze, B. H. Schneider,
A. Taspinar, H. S. J. van der Zant, and G. A. Steele

We have used the mechanical motion of a carbon nanotube (CNT) as a probe of the average charge on a quantum dot. Variations of the resonance frequency and the quality factor are determined by the change in average charge on the quantum dot during a mechanical oscillation. The average charge, in turn, is influenced by the gate voltage, the bias voltage, and the tunnel rates of the barriers to the leads. At bias voltages that exceed the broadening due to tunnel coupling, the resonance frequency and quality factor show a double dip as a function of gate voltage. We find that increasing the current flowing through the CNT at the Coulomb peak does not increase the damping, but in fact decreases damping. Using a model with energy-dependent tunnel rates, we obtain quantitative agreement between the experimental observations and the model. We theoretically compare different contributions to the single-electron induced nonlinearity, and show that only one term is significant

---

This Chapter has been published in Phys. Rev. B **86**, 115454 (2012) [1].

for both the Duffing parameter and the mode coupling parameter. We also present additional measurements which support the model we develop: Tuning the tunnel barriers of the quantum dot to the leads gives a 200-fold decrease of the quality factor. Single-electron tunneling through an excited state of the CNT quantum dot also changes the average charge on the quantum dot, bringing about a decrease in the resonance frequency. In the Fabry-Pérot regime, the absence of charge quantization results in a spring behaviour without resonance frequency dips, which could be used, for example, to probe the transition from quantized to continuous charge with a nanomechanical resonator.

4.1 INTRODUCTION

Nanomechanical systems [2, 3] are studied intensively for both their potential applications such as mass sensing [4–6] and for insights into the quantum mechanical ground state of a macroscopic object [7–11]. Because of their small size, nanomechanical resonators are strongly influenced by electrostatic forces from single-electron charge effects, which allows single-electron transistors to be used as sensitive detectors of the deflection of a nanomechanical beam [12, 13], demonstrating clear backaction from the single-electron forces [14]. Coupling of these forces to mechanical resonators can also be exploited in mechanical single-electron shuttle devices [15] to shuttle electrons one-by-one through the nanomechanical resonator.

A carbon nanotube (CNT) is a stiff, bottom-up nanomechanical resonator with a large aspect ratio [16]. Dissipation in an ultraclean CNT at cryogenic temperatures is low, which results in a high quality factor [17] and allows investigation into other sources of damping, such as nonlinear [18] and magnetic damping [19]. At cryogenic temperatures, a quantum dot is formed, embedded in the CNT [20, 21], which makes single-electron charge effects couple strongly to the mechanical motion through the bending mode (see [22] and Ch. 3). For a CNT quantum dot, the effects of damping, spring stiffening and softening, and nonlinearity, are completely dominated by single-electron charging effects (see also Ch. 6).

The interplay between single-electron tunneling and mechanical motion has been the topic of many theoretical investigations. The motion of nanomechanical resonators is found to have an influence on the electron transport through the single-electron transistor [23, 24] affecting current [25, 26] and current noise [27–30]. Conversely, transport through the single-electron transistor by tunneling of single electrons causes backaction [28, 31] on the mechanical motion in the form of frequency shifts [32, 33] and damping [26, 32, 34, 35]. Under certain conditions, single-electron tunneling can lead to a negative charging energy [36] or negative damping, causing instabilities, where a distinction should be made between the low-frequency limit [37] ($\omega_0 \ll \Gamma$) and the high-frequency limit [38] ($\omega_0 \gg \Gamma$), relating the mechanical resonance frequency, ω_0, to the single-electron tunnel rate, Γ. Besides causing backaction on the mechanical motion, single-electron tunneling is proposed to be used to parametrically drive the nanomechanical resonator [39]. In the Coulomb blockade regime, CNT quantum dot resonators in particular are found to have a large electron-vibron coupling [40], and nonlinear restoring forces are found to be completely dominated by single-electron tunneling effects (see Ch. 6 and [33]). Further theoretical studies have been performed on the subject of single-electron shuttles [41–44], and on the coupling between a single-electron transistor and a nanomechanical resonator in the quantum regime [45–47].

In this Chapter, we present measurements of single-electron effects in CNT resonators in the Coulomb blockade regime and we demonstrate that our experimental observations agree quantitatively with the theoretical model we develop. This agreement allows the CNT nanomechanical resonator to be used as a probe for the average charge residing on the CNT quantum dot. Furthermore, we examine the implications of the established model through additional experiments. The layout of the Chapter is as follows. In section 4.2, the fabrication of the ultraclean suspended CNT is described, followed by the measurement setup. Section 4.3 contains the characterization of the CNT device in electrical terms, and the influence of single-electron tunneling on the mechanical resonance frequency, followed by the novel experimental observation of a double frequency dip feature. In section 4.4, we develop a model for the dynamics of the mechanical resonator in the presence of Coulomb blockade, which explains the presence of such a double frequency dip, and make a quantitative comparison to the measured data. In section 4.5, we extend this model to include the effect of Coulomb blockade on mechanical damping and, again, compare the model to experimental data. In section 4.6, we expand the model further with the description of single-electron induced nonlinearity, resulting in an expression for the Duffing parameter and the mode coupling parameter. In section 4.7, we explore the coupling of the average charge to the mechanical resonator by varying the tunnel rates of the quantum dot, by studying the effects of excited states of the quantum dot, and by studying the mechanical resonator in the Fabry-Pérot regime, in which Coulomb Blockade no longer plays a role. All of these additional measurements can be understood qualitatively in the context of the model we present.

4.2 FABRICATION AND MEASUREMENT SETUP

Ultraclean suspended carbon nanotube devices are fabricated as follows [48]. The fabrication begins with a degenerately doped silicon wafer with a 285 nm thermal oxide. In the first step, the contacts are patterned by evaporating 5 nm of tungsten and 25 nm of platinum on a patterned double layer of PMMA, and performing lift-off. In the second step, a three-layer etch mask, consisting of photoresist, tungsten, and PMMA, is used to etch the trenches between the contacts. The trenches are first patterned onto the PMMA by electron beam lithography. This pattern is transferred onto the tungsten by parallel plate reactive ion etching using a mixture of SF_6 and helium, where the PMMA acts as an etch mask. After this, the photoresist is etched by an oxygen plasma, during which the tungsten acts as an etch mask. In the third step, trenches between the contacts are etched into the silicon oxide, by the same mixture of SF_6 and helium, during which the photoresist acts as an etch mask. To improve wire-bonding, a layer of 10 nm of chromium and 80 nm of platinum is evaporated onto the bondpads, followed by a sputtered layer of 20 nm of silicon. In the final step, catalyst islands [49] are deposited onto holes patterned in a double layer of PMMA. The sample is now placed in a CVD oven, where CNTs grow out of the catalyst particles in a mixture of hydrogen and methane at a temperature of 900 °C. As the CNTs grow in a random direction, approximately one third of the patterned trenches has a CNT across them, touching both the source and the drain, thus forming a device. Room temperature measurements of current as a function of gate voltage are performed for each trench, showing semiconductor behaviour for potential devices.

Figure 4.1a shows a schematic diagram of the setup used to measure mechanical resonances in the suspended carbon nanotube devices [17]. The device is mounted at the mixing chamber of a ^{3}He/^{4}He dilution refrigerator with a temperature of 20 mK. Filtered twisted-pair cabling is used to connect to the source, drain, and gate of the device, allowing d.c. voltages to be applied to the source and gate. The current flowing through the device is measured at the drain. The CNT is driven into motion by an a.c. voltage difference between the gate electrode and the CNT. This high-frequency signal needed to drive the CNT is supplied by an RF source through a coaxial cable. At a separation of ~1 cm from the device, the shielding of the coaxial cable is removed to form the antenna. We expect that the electrostatic coupling between the antenna and the nanotube segment itself is much too small to actuate the CNT, which was confirmed by a lack of response of the CNT quantum dot to a d.c. voltage applied to the coax. Instead, the coaxial cable is capacitively coupled to the d.c. wires leading to the source, drain, and gate. Because of a difference in crosstalk capacitance from the coaxial cable to the source, drain, and gate, a.c. voltages are generated asymmetrically on the three. The a.c. voltage difference arising between the gate and the CNT then actuates the CNT into motion.

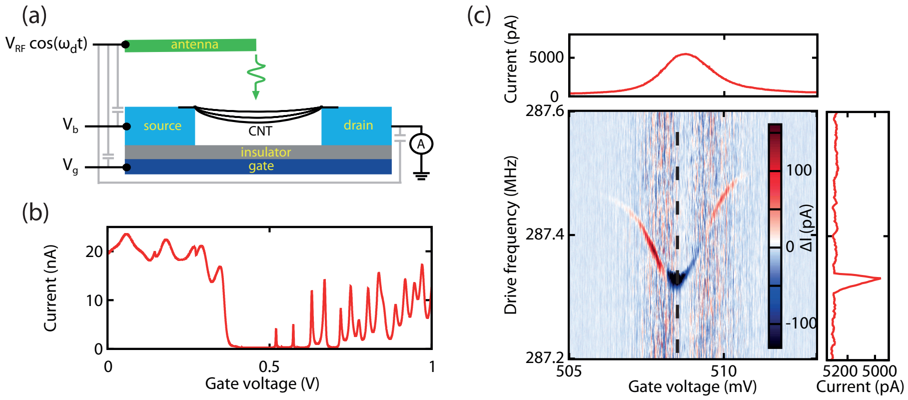

FIGURE 4.1: (a) Schematic drawing of the chip geometry, antenna, and measurement electronics. The CNT acts as a doubly-clamped beam resonator with a displacement x and is driven because of an asymmetrical capacitive coupling of the radio frequency coaxial cable to the source, drain, and gate. (b) Current versus gate voltage at V_b = 0.3 mV showing, for increasing gate voltage, Fabry-Pérot oscillations, then a small bandgap, and finally Coulomb oscillations with the increasing tunnel coupling to the leads opening up the quantum dot as the gate voltage is increased further. (c) Top panel: Current as a function of gate voltage, showing a Coulomb peak. Middle panel: Change in current as a function of drive frequency and gate voltage, showing a dip in resonance frequency across the Coulomb peak. Right panel: Current as a function of drive frequency at a gate voltage, V_g = 508.5 mV, as denoted by the black dashed line in the middle panel, showing the mechanical resonance as a decrease in current around $\omega_d/2\pi = 287.33$ MHz.

4.3 ELECTRICAL AND MECHANICAL CHARACTERISTICS

Figure 4.1b shows the current through a small-bandgap CNT with a suspended length of 600 nm as a function of gate voltage. For gate voltages below $V_g = 0.4$ V, the device is doped with holes and weak scattering at the metal-CNT interface at the edge of the trench results in conductance that is modulated by Fabry-Pérot interferences [50] of the hole wavefunction. For $0.4 < V_g < 0.5$, the Fermi level lies in the bandgap and the current is suppressed. From the distance in gate voltage from electron and hole conduction, together with the coupling factor $\alpha = C_g/C_{tot} = 0.38$ determined from the Coulomb diamonds, we estimate the bandgap to be $E_{gap} =$ 58 meV. Above $V_g = 0.5$ V, Coulomb oscillations are visible. Now, electrons tunnel onto the CNT through tunnel barriers, which arise from the p-n junctions between the segments of the CNT near the W/Pt metal near the edge of the trench and the CNT. The small capacitance between the quantum dot and the three terminals gives rise to a large charging energy of $E_C = 9.6$ meV. For $V_g > 0.7$ V, the Coulomb peaks are increasingly more smeared out. For larger electron doping, the p-n junctions become narrower and the tunnel barriers to the quantum dot become more transparent [48].

We measure the mechanical bending mode resonances of the CNT by actuating it into motion and measuring the d.c. current. When the drive frequency matches the resonance frequency, the CNT resonates, causing the capacitance between the CNT and the gate to oscillate with a large amplitude. This oscillating capacitance effectively induces an oscillating gate voltage. The nonlinearity of the Coulomb peak allows the oscillating effective gate voltage from the motion to be rectified into a d.c. current [17].

As reported earlier, the mechanical resonance frequency of the CNT is strongly influenced by single-electron tunneling (see Ch. 3). The middle panel of Fig. 4.1c shows the change in current due to the mechanical motion, ΔI, as a function of the drive frequency and gate voltage on a Coulomb peak at $V_b = 0.2$ mV. On a Coulomb peak, single-electron tunneling leads to a dip in the resonance frequency. In the top panel of Fig. 4.1c, a linecut is shown of current versus gate voltage at a drive frequency chosen to be far from the resonance frequency. In the right panel of Fig. 4.1c, a linecut is shown of the current versus the drive frequency at one gate voltage, denoted by the black dashed line in the middle panel, showing the mechanical resonance as a change in the d.c. current.

In order to qualitatively understand these dips in frequency, three essential elements are required. The first is that the motion of the CNT changes the charge on the quantum dot, which in turn changes the electrostatic force on the CNT. Thus, the CNT experiences a displacement-dependent electrostatic force. Because the electron tunnel rates Γ are much faster than the mechanical frequency f_0 ($\Gamma \sim 450$ GHz, $f_0 \sim 300$ MHz), the mechanical motion sees a displacement-dependent force from the charge averaged over many tunnel events. This displacement-dependent force induces a reduction of the spring constant, which changes the mechanical frequency.

The sign of the frequency shifts can be understood by realizing that electrostatic forces do not act as a restoring force, but instead as an anti-restoring force: if the CNT is pulled away from its equilibrium position towards the gate, for example, the electrostatic force will increase and tend to pull the CNT with more force towards the gate. Thus, electrostatic forces generally result in a decrease of the net spring constant.

Finally, to understand the gate voltage dependence, it is illustrative to examine the differential capacitance of the quantum dot to the gate. Due to the quantized charge on the island of the dot, the quantum dot shows zero differential capacitance when it is in the Coulomb valleys: the charge is fixed independent of gate voltage. At the position of the Coulomb peaks, the charge on the island undergoes a discrete step of one electron. In the absence of tunnel or temperature broadening of this transition, this step would be infinitely sharp, and the differential capacitance would diverge. The electrostatic spring effects discussed in the previous paragraph are determined by the differential capacitances for small amplitudes of motion, and the diverging differential capacitance of the quantum dot at the positions of the Coulomb peaks leads to a diverging softening renormalization of the net mechanical spring constant, resulting in the dips in mechanical frequency observed in the data.

In this Chapter, we explore in detail how single-electron tunneling affects the mechanical motion of the CNT and develop a quantitative model to describe our results. In contrast to earlier work (see Ch. 3), here we map out the behaviour of the mechanical resonator for bias and gate voltages covering the single-electron tunneling region between two charge states. The stability diagram in Fig. 4.2a shows the differential conductance, dI/dV_b, as a function of gate voltage and bias voltage for the transition from 1 to 2 electrons. Coulomb blockade is visible in blue, whereas single-electron tunneling takes place in the red and white regions.

At a low bias voltage, Fig. 4.2b shows, in blue, the experimentally obtained normalized current, $|I-I_0|/|I-I_0|_{max}$, as a function of gate voltage and drive frequency, where I_0 is the current off mechanical resonance. The bias voltage of 0.17 mV for this figure is denoted by the upper white dashed line in Fig. 4.2a. The mechanical resonance is visible as an increase in the normalized current. Around $V_{g,offset} = 1$ mV, where $V_{g,offset} = V_g - 0.565$ V, the mechanical resonance frequency shows a dip, as was demonstrated in previous measurements.

When the bias voltage is increased, the resonance frequency of the CNT exhibits substantially different behaviour. Figure 4.2c shows the measured normalized current as a function of gate voltage and drive frequency as a color plot at a bias voltage of −0.55 mV, corresponding to the lower white dashed line in Fig. 4.2a. Instead of one dip, two dips in resonance frequency are visible. The presence of such a peculiar double dip feature in the mechanical resonance frequency forms the motivation for the work in the following sections, in which we establish a quantitative model for the mechanical resonance frequency and quality factor in the presence of Coulomb blockade, and further explore the coupling of the mechanical resonator dynamics to the average charge of the quantum dot.

4.4 MODELING SINGLE-ELECTRON SPRING EFFECTS

This section describes a model developed for the coupling of the mechanical resonator to the Coulomb blockaded quantum dot, and the quantitative fitting of the experimentally observed frequency dips. In subsection 4.4.1, a model for the average charge on the CNT is described. In subsection 4.4.2, we derive a model for how the average charge leads to a displacement-dependent force that causes the softening of the CNT spring. In subsection 4.4.3, fits of the experimentally obtained

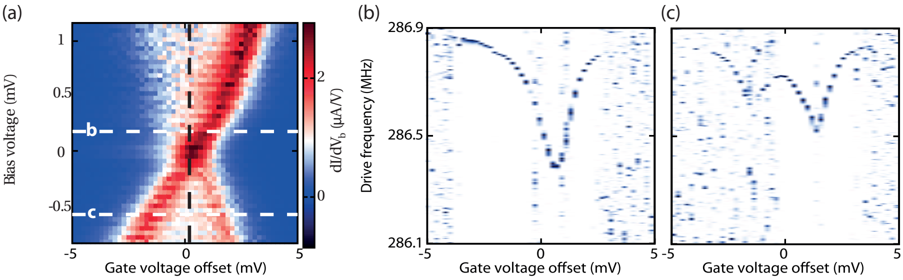

FIGURE 4.2: (a) Stability diagram: dI/dV_b as a function of bias and gate voltage for the charge transition from 1 to 2 electrons. The linecuts, at which Figs. 4.2b and c are taken, are indicated by the white dashed lines. The black dashed line denotes the gate voltage at which the middle panel of Fig. 4.4c is taken. (b, c) Measured normalized current, $|I - I_0|/|I - I_0|_{max}$, as a function of drive frequency and gate voltage offset at (b) $V_b = 0.17$ mV, showing a decrease in resonance frequency around $V_{g,offset} = 1$ mV, and at (c) $V_b = -0.55$ mV, showing a double dip in resonance frequency.

resonance frequency and current are performed using the established model.

4.4.1 MODEL FOR THE AVERAGE CHARGE ON A QUANTUM DOT

The average charge on the CNT at a charge transition can be determined as follows. Single-electron tunneling onto or off the CNT is a stochastic process, where the amount of time an electron spends on the source or the CNT is determined, respectively, by the tunneling rates Γ^+ and Γ^-. The average occupation, $\langle N \rangle$, of charges on the CNT for the charge transition from N_0 to $N_0 + 1$ electrons is given by:

$$\langle N \rangle = N_0 + \frac{\Gamma^+}{\Gamma_{tot}}, \tag{4.1}$$

where $\Gamma_{tot} = \Gamma^+ + \Gamma^-$.

The tunneling rates, determining the average occupation, are modeled as follows. Traditionally, tunneling onto and off a quantum dot is described [51, 52] using energy-independent tunnel rates. The average occupation and the current are determined by using energy-independent tunnel rates and the overlap of the density of available states of the quantum dot and the leads. Such an approximation of energy-independent tunnel rates is valid when the tunnel barriers are sufficiently high, so that a change in either bias or gate voltage does not cause a significant change in the barrier height or width.

In this work instead, we use energy-dependent tunnel rates, assuming that the tunnel barriers are not high. This assumption is supported by the strong dependence of the tunnel barriers on the gate voltage (cf Fig. 4.1b). The influence of bias and gate voltage on the tunnel rates is demonstrated in Figs. 4.3a and b. At zero bias voltage, Fig. 4.3a shows the p-n junctions as tunnel barriers between the CNT and the leads. When the bias voltage is increased, Fig. 4.3b illustrates how the higher electrostatic potential of the source increases the tunnel barrier at the source, leading to a lower tunnel rate, whereas the tunnel barrier at the drain is decreased, resulting in a higher tunnel rate. In our device, the tunnel barriers are not formed by steps in the potential but instead by p-n junctions in the CNT. Figure 4.3c shows how tunnel barriers arise from p-n junctions formed in the CNT at the metal-CNT interface, as the chemical potential of the CNT is decreased by a positive gate voltage. The height of the tunnel barriers is determined by the bandgap of the CNT, E_{gap}.

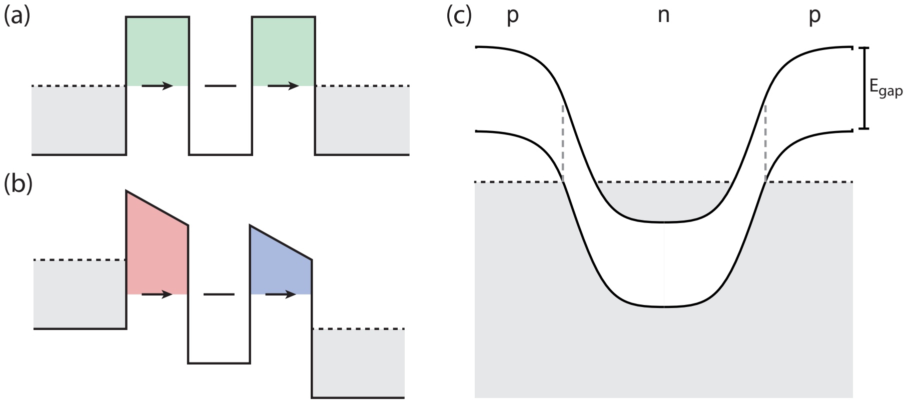

FIGURE 4.3: (a) Energy diagram at zero bias voltage, with the p-n junctions represented by square tunnel barriers between the CNT and the leads. (b) Energy diagram at finite bias voltage, showing an increase of the height of the tunnel barrier to the source relative to the energy of the tunneling electron, and a decrease in the height of the barrier to the drain. (c) Diagram of the CNT band structure with two p-n junctions induced through a positive gate voltage.

To calculate the tunnel rates, the density of available states of the leads and the quantum dot are used, taking the energy dependence of the tunnel rates into account. The density of available states of the level in the CNT quantum dot, $D(\mu)$, caused by tunnel coupling to the leads, is described with a Lorentzian lineshape.

$$D(\mu) = \frac{1}{2\pi} \frac{\hbar\Gamma_{broad}}{(\mu - \mu_{CNT})^2 + (\hbar\Gamma_{broad}/2)^2}. \tag{4.2}$$

Here, μ_{CNT} is the chemical potential of the CNT. The broadening Γ_{broad} gives the full width at half maximum. At $T = 20$ mK, we are in the regime where $\hbar\Gamma_{broad} \gg$

$k_B T$. The density of available states of the left and right lead, $f_{L,R}(E)$, is now modeled by a step function:

$$f_{L,R}(E) = \begin{cases} 1 : E < \mu_{L,R} \\ 0 : E > \mu_{L,R}, \end{cases} \tag{4.3}$$

where E is the energy of the electron, and $\mu_{L,R}$ is the chemical potential of the left (right) lead. The tunnel rates are determined by the overlap of the density of available states of the CNT and the leads, and by their relative chemical potential:

$$\Gamma^{\pm}_{L,R} = a_{L,R} e^{b_{L,R}\Delta\mu_{L,R}} \left(\frac{1}{2} + \frac{1}{\pi} \arctan\left(\frac{\mp 2\Delta\mu_{L,R}}{\hbar\Gamma_{broad}} \right) \right). \tag{4.4}$$

Here, the energy-dependent tunneling is reflected by the exponential factor, which is shown theoretically [53] to occur for tunnel barriers brought about by an electrostatic potential, where the barrier height is low and the barrier width is large. The parameters $a_{L,R}$ depend on the height and width of the tunnel barriers. The parameters $b_{L,R}$ describe the triangular profile that the tunnel barriers have, which is there at zero bias voltage (cf Fig. 4.3c) and is additionally changed by altering the bias and gate voltage (cf Fig. 4.3b). The difference in chemical potential between the CNT and the left or right lead is denoted by $\Delta\mu_{L,R} = \mu_{CNT} - \mu_{L,R}$. The last factor in Eq. 4.4 arises from the broadening due to tunnel coupling and is determined from the overlap of the density of available states of the left or right electrode with that of the CNT.

The calculated average occupation, at a bias voltage of $V_b = 0.17$ mV, corresponding to the white dashed line labeled (b) in Fig. 4.2a, is shown in the top panel of Fig. 4.4a as a function of gate voltage at the charge transition from 1 to 2 electrons. At zero broadening, $\Gamma_{broad} = 0$, the green line shows the average occupation increase in two discrete steps. The left inset of Fig. 4.4a shows an energy diagram illustrating zero broadening. The three discrete plateaus in average charge correspond to Coulomb blockade, single-electron tunneling, and Coulomb blockade again. At a broadening of $\Gamma_{broad} = 450$ GHz, for which $\hbar\Gamma_{broad} > e|V_b|$, the red line shows the average occupation increases monotonically in a single step. The right inset of Fig. 4.4a illustrates how the double step in average occupation, seen at zero broadening, is completely smeared out. Here, e is the elementary charge, k_B is Boltzmann's constant, and $\hbar$ is the reduced Planck's constant.

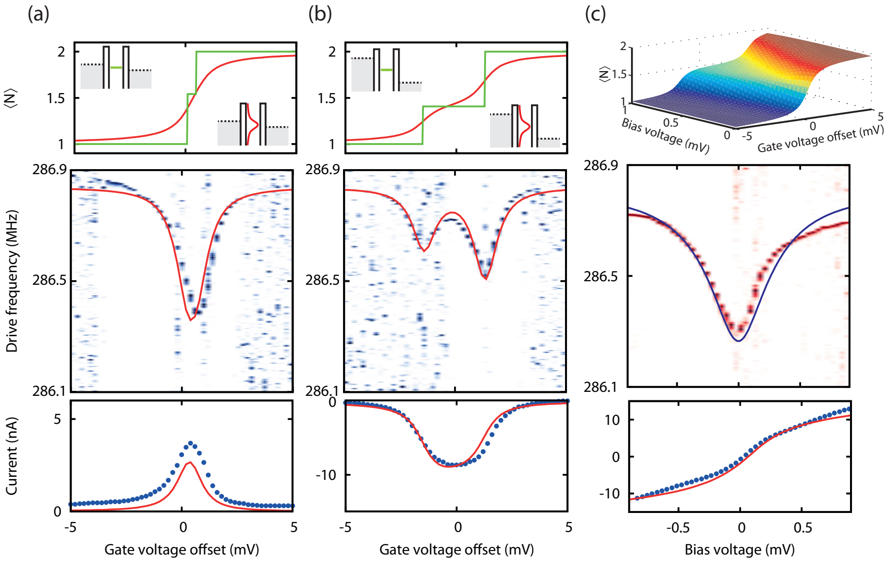

FIGURE 4.4: (a, top) Calculated average occupation, $\langle N \rangle$, as a function of gate voltage at $V_b = 0.17$ mV, showing two discrete steps for $\Gamma_{broad} = 0$ (green line), and a smeared-out monotonic increase for $\Gamma_{broad} = 450$ GHz (red line). Insets: energy diagrams at low bias for zero broadening (left) and finite broadening (right). (a, b, c, middle) Measured normalized current, $|I - I_0|/|I - I_0|_{max}$, as a function of drive frequency and (a, blue) gate voltage offset at $V_b = 0.17$ mV (b, blue) gate voltage offset at $V_b = -0.55$ mV, and (c, red) bias voltage at a gate voltage offset $V_{g,offset} = 0.04$ mV and the corresponding calculated resonance frequency (red line, red line, blue line), showing (a) a decrease in resonance frequency around $V_{g,offset} = 0$, (b) a double dip in resonance frequency, (c) a decrease in resonance frequency for low bias voltages. (a, b, c, bottom) Measured (blue dots) and calculated (red line) current as a function of gate voltage at (a) $V_b = 0.17$ mV, (b) $V_b = -0.55$ mV, and (c) as a function of bias voltage at $V_{g,offset} = 0.04$ mV. (b, top) Calculated average occupation, $\langle N \rangle$, as a function of gate voltage at $V_b = -0.55$ mV, showing two discrete steps for both $\Gamma_{broad} = 0$ (green line) and for $\Gamma_{broad} = 450$ GHz (red line). Insets: energy diagrams at high bias for zero broadening (left) and finite broadening (right). (c, top) Calculated average occupation, $\langle N \rangle$, as a function of gate voltage and bias voltage at $\Gamma_{broad} = 450$ GHz, showing the average occupation, $\langle N \rangle$, from increasing in a single step at zero bias to increasing in two steps at $V_b = 1$ mV.

At a bias voltage of $V_b = -0.55$ mV, corresponding to the white dashed line labeled (c) in Fig. 4.2a, the calculated average occupation is shown in the top panel of Fig. 4.4b as a function of gate voltage. Both at a broadening of $\Gamma_{broad} = 0$ (green) and at a broadening of $\Gamma_{broad} = 450$ GHz (red), two steps and three plateaus are visible. The insets of the top panel of Fig. 4.4b show how all allowed states on the CNT are inside the bias window, both for zero broadening (left) and finite broadening (right). Contrary to low bias, the two steps are not smeared into a single step at finite broadening.

For different bias voltages, the calculated average occupation is shown in the top panel of Fig. 4.4c as a function of gate voltage. At low bias, the charge transition takes place in a small range in gate voltage. This gives rise to a large slope for the average occupation with respect to gate voltage. As the bias voltage is increased, the range in gate voltage increases. When the bias voltage is larger than the broadening, the average occupation increases in two steps.

4.4.2 MODEL FOR THE SINGLE-ELECTRON SPRING

Using the average charge as determined in the previous subsection, the shift in resonance frequency is modeled as follows. The electrostatic force acting on the CNT depends on the voltage difference between the CNT and the gate electrode [54]:

$$F_{CNT} = \frac{1}{2}\frac{dC_g}{dx}(V_g - V_{CNT})^2, \tag{4.5}$$

where C_g is the capacitance between the CNT and the gate, x is the displacement of the fundamental mode of the CNT, and V_g and V_{CNT} are the voltages on the gate and the CNT, respectively. The voltage on the CNT is determined by the control charge, $q_c = C_g V_g + C_S V_S + C_D V_D$, which is the charge that would be on the CNT in the absence of Coulomb blockade, and the average occupation, $\langle N \rangle$, of charges residing on the CNT:

$$V_{CNT} = \frac{q_c - e\langle N \rangle}{C_{tot}}. \tag{4.6}$$

Here, $C_{S,D}$ and $V_{S,D}$ are the capacitances to and the voltages on the source and drain respectively, and $C_{tot} = C_g + C_S + C_D$. In our case, the bias voltage is applied to the source, $V_S = V_b$, and the drain electrode is grounded, $V_D = 0$. Because the charge N on the dot fluctuates stochastically between N_0 and N_0+1 at a rate $\Gamma_{tot} \gg f_0$, the mechanical motion experiences a voltage on the CNT due to an average occupation, $\langle N \rangle$.

The spring constant and, consequently, the resonance frequency of the CNT are determined by the change in force acting on the CNT per unit displacement:

$$2m\omega_0\Delta\omega_0 = \Delta k = -\frac{dF}{dx}, \tag{4.7}$$

where m is the mass of the CNT, and $\Delta\omega_0 \ll \omega_0$. The full derivative of the force with respect to the displacement of the CNT is expanded into partial derivatives with respect to displacement and gate voltage:

$$\begin{aligned} -\frac{dF(x,V_g)}{dx} &= -\frac{\partial F(x,V_g)}{\partial x} - \frac{dC_g}{dx}\frac{dq_c}{dC_g}\frac{dV_g}{dq_c}\frac{\partial F(x,V_g)}{\partial V_g} \\ &= -\frac{1}{2}\frac{d^2C_g}{dx^2}(V_g - V_{CNT})^2 \\ &\quad - \frac{V_g(V_g - V_{CNT})}{C_g}\left(\frac{dC_g}{dx}\right)^2 \frac{\partial(V_g - V_{CNT})}{\partial V_g}. \end{aligned} \tag{4.8}$$

The first term gives rise to a softening spring effect due to the capacitive force between the CNT and the gate. The second term takes into account the influence of the displacement on the control charge through the gate capacitance. In turn, the influence of the control charge on the force is incorporated through the gate voltage. In this Chapter, we focus on changes in the spring constant that occur rapidly with gate voltage and we show that the experimental features can be captured using only the second term.

Combining Eq. (4.6) and the second term of (4.8) leads to the following expression for the change in resonance frequency due to a changing average charge:

$$\Delta\omega_0 = \frac{V_g(V_g - V_{CNT})}{2m\omega_0 C_{tot}}\left(\frac{dC_g}{dx}\right)^2\left(1 - \frac{C_{tot}}{C_g} - \frac{e}{C_g}\frac{\partial\langle N\rangle}{\partial V_g}\right). \tag{4.9}$$

Because of the rightmost minus sign and the fact that $\partial\langle N\rangle/\partial V_g > 0$, the changing average charge on the CNT leads to a softening spring effect. The resonance frequency of the CNT decreases more when the mechanical oscillation causes a larger change in average charge, expressed by $\partial\langle N\rangle/\partial V_g$.

4.4.3 FITTING OF THE EXPERIMENTAL RESONANCE FREQUENCY SHIFT AND DISCUSSION

To verify the model established in the previous two paragraphs, we perform a quantitative fit on the experimental data shown earlier in Fig. 4.2. The fits are accomplished by using Eq. 4.9 and a single set of parameters for all figures. The values chosen for the parameters can be found in the appendix in section 4.9. A value for

$\partial \langle N \rangle / \partial V_g$ is obtained by numerically differentiating the calculated average occupation, as is displayed in the top panel of Fig. 4.4a, with respect to gate voltage.

The red graphs in the middle panel of Fig. 4.4a and b show the calculated change in resonance frequency as a function of gate voltage. At $V_b = 0.17$ mV, Fig. 4.4a shows quantitative agreement between the measurement and the model describing the frequency dips. The frequency dip corresponds to the largest slope of the average charge with gate voltage. At $V_b = -0.55$ mV, Fig. 4.4b demonstrates how the model reproduces the experimentally observed double dip structure. At the plateau in average charge, the mechanical oscillation only brings about a small change in average charge, and the resonance frequency returns towards its original value.

To investigate the reduction in the resonance frequency as a function of bias voltage, a vertical linecut is taken, at a constant gate voltage through the charge degeneracy point in the stability diagram. The middle panel of Fig. 4.4c shows the measured current, but now as a function of bias voltage, not gate voltage, and drive frequency. The calculated resonance frequency in blue shows excellent quantitative agreement with the measurement. At low bias voltages, the narrow charge transition leads to a large change in average charge due to the mechanical oscillation and a large change in the displacement-dependent force, resulting in a large decrease in resonance frequency. At higher, both positive and negative, bias voltage, the slope in average occupation, $\partial\langle N\rangle/\partial V_g$, becomes less, as the plateau arises. This leads to a smaller change in the displacement-dependent force and a smaller decrease in the resonance frequency.

The experimentally obtained current flowing through the CNT is shown with blue dots in the bottom panels of Fig. 4.4 at $V_b = 0.17$ mV (a), $V_b = -0.55$ mV (b), and as a function of bias voltage (c). For $V_b = 0.17$ mV, a Coulomb peak is visible. For $V_b = -0.55$ mV, the plateau in current shows that the bias voltage, V_b, is larger than the broadening, Γ_{broad}. As a function of bias, the bottom panel of Fig. 4.4c shows no Coulomb blockade, since the vertical linecut in bias voltage exactly passes through the charge degeneracy point. The absence of a saturation of the current at high bias voltage indicates low tunnel barrier heights and supports the choice of energy-dependent tunnel rates. As an independent examination of the chosen tunnel rates, the measured current is fitted using the same parameters as for the frequency dips (red lines). The current is calculated using [55]:

$$I = e\frac{\Gamma_L^+\Gamma_R^- - \Gamma_R^+\Gamma_L^-}{\Gamma_{tot}}. \tag{4.10}$$

For intermediate bias voltages, Fig. 4.5 illustrates the transition from the double dip structure to a single dip. Using the same set of parameters as for Fig. 4.4, the calculated resonance frequency follows the measurement well. The quantitative agreement between the experiment and the calculation of the resonance frequency and the current for different bias voltages demonstrates the consistency of the single set of parameters used for the calculation.

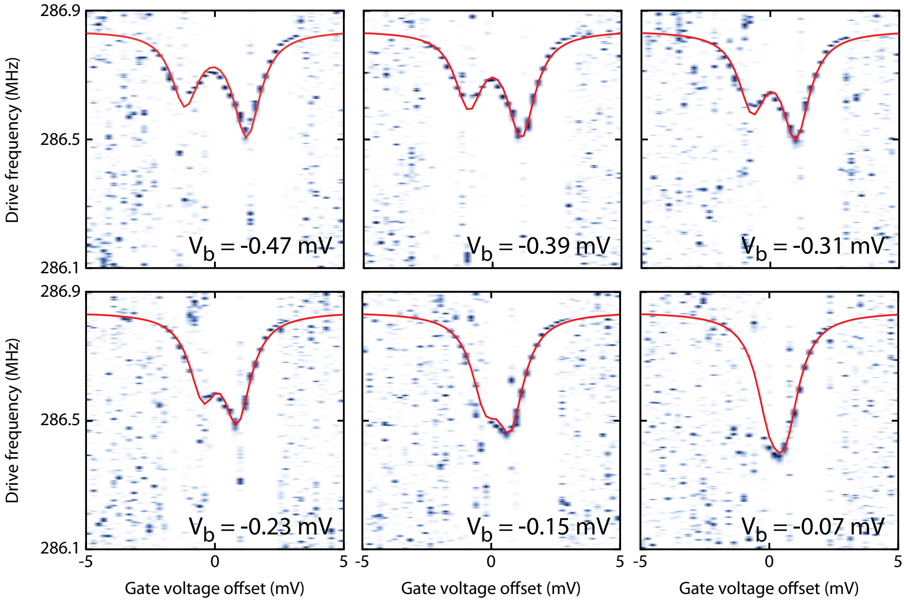

FIGURE 4.5: Measured normalized current (blue) and calculated resonance frequency (red line) as a function of gate voltage offset for different bias voltages, showing the transition of the double dip structure into a single dip as the bias voltage becomes less negative.

4.5 SINGLE-ELECTRON DAMPING

In this section, the influence of the changing average charge on the mechanical quality factor of the CNT is investigated. As with the resonance frequency in the previous section, the quality factor is determined experimentally and by using a model, for low bias voltage, high bias voltage, and as a function of bias voltage. To show the consistency of the used parameters, the corresponding resonance frequency is also displayed.

Figure 4.6a shows the stability diagram of the charge transition from 7 to 8 electrons at a parallel magnetic field of 8 T. The current flowing through the CNT is measured as a function of bias and gate voltage, and the derivative dI/dV_b is determined numerically. The letters b and d denote, respectively, the low and high bias voltage, at which Figs. 4.6b and 4.6d were taken. The letter f denotes the gate voltage at which Fig. 4.6f was taken.

4.5.1 EXPERIMENTAL OBSERVATION OF SINGLE-ELECTRON DAMPING

The experimentally determined mechanical quality factor at a low bias voltage of $V_b = 0.3$ mV is displayed in blue dots in the top panel of Fig. 4.6b. The quality factor is obtained by measuring the current versus drive frequency 10 times and averaging. The drive power is adjusted for each quality factor measurement such that the frequency response shows a lineshape which is as close as possible to Lorentzian, but which is not obscured by noise. By working at low powers in the linear response regime, we minimize the likelihood that nonlinear damping terms [18] play a significant role. The change in current, ΔI, due to the mechanical motion in our detection scheme is proportional to the amplitude of the displacement squared. At the sides of the Coulomb peak, the lack of nonlinearity of the current with gate voltage prevents the measurement of the mechanical motion through a change in current, and consequently a determination of the quality factor. A fit with the following Lorentzian function is performed to extract the quality factor.

$$\Delta I(\omega_d) = \mathscr{A}\frac{\omega_0^4/Q^2}{((\omega_0^2-\omega_d^2)^2+\frac{\omega_0^2\omega_d^2}{Q^2})}. \tag{4.11}$$

Here, Q is the mechanical quality factor, ω_d is the drive frequency, and $\mathscr{A} = \frac{1}{4}\left(\frac{V_g}{C_g}\frac{dC_g}{dx}\right)^2\frac{d^2I}{dV_g^2}x^2$ is a fit parameter, which incorporates the amplitude of oscillation x and the electromechanical coupling. At a low bias of $V_b = 0.3$ mV, a large decrease in the quality factor of two orders of magnitude is visible, spanning several millivolts of gate voltage corresponding to single-electron tunneling. The top panel of Fig. 4.6d shows the experimentally obtained quality factor in blue dots at a high bias voltage of $V_b = 1.1$ mV. Here, similarly to the double frequency dip at high bias in the middle panel of Fig. 4.4b, two dips in quality factor are visible.

To investigate the relation between current and single-electron damping of the mechanical motion, Fig. 4.6e shows the current as a function of bias voltage. The gate voltage is chosen such that the graph is a vertical linecut through the charge degeneracy point. The top panel of Fig. 4.6f shows the corresponding quality factor as a function of bias voltage, again at a gate voltage of $V_g = 0.9002$ V. The quality factor exhibits a dip at low bias voltages and returns to its original value at higher, both negative and positive, bias voltage. We emphasize that the highest current flowing through the CNT does not correspond to the largest reduction in quality factor. Instead, in fact, when the gate voltage is positioned at a Coulomb peak, the quality factor actually goes up when increasing the current through the device.

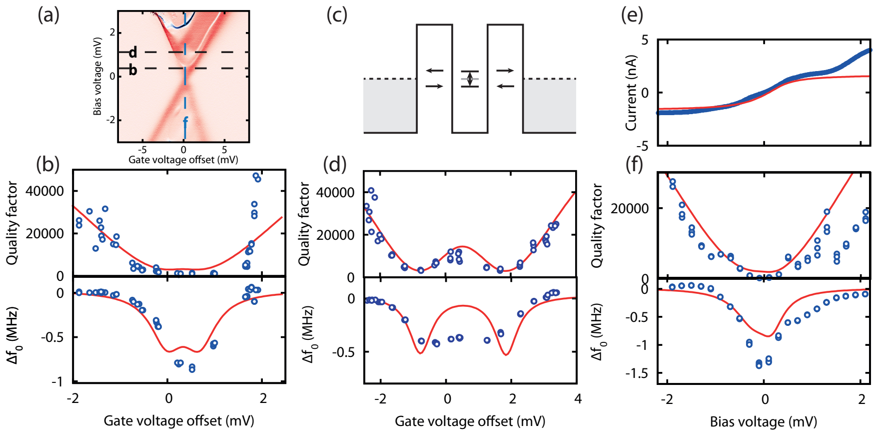

FIGURE 4.6: (a) Stability diagram at a parallel magnetic field of 8 T and $V_g = 0.9$ V, showing the charge transition from 7 to 8 electrons, with the gate and bias voltages at which Figs. 4.6b, 4.6d, and 4.6f were taken, indicated by black and blue dashed lines. (b, d, f) Comparison between measurement (blue dots) and model (red lines) of the quality factor (top) and the shift in resonance frequency (bottom) as a function of gate voltage (b, d) and bias voltage (f), showing, (b) at $V_b = 0.3$ a single dip, (d) at $V_b = 1.1$ mV, a double dip, and (f) at $V_{g,offset} = 0$ mV, a large decrease in quality factor and resonance frequency at low bias voltages. (c) Energy diagram (exaggerated) illustrating the damping mechanism, showing the asymmetry of electrons tunneling onto the CNT at low chemical potential and off the CNT at high chemical potential. (e) Measured (blue dots) and calculated (red line) current as a function of bias voltage at $V_{g,offset} = 0$ V.

Figure 4.6c shows the basic concept of the damping mechanism, illustrated with zero broadening and one electron tunneling event during a mechanical oscillation. Let us first consider the zero bias voltage case. The mechanical motion brings the chemical potential of the CNT below and above the Fermi level of the leads. The asymmetry of the Fermi sea in the leads implies that electrons can only tunnel onto the CNT when the level of the CNT is below the Fermi energy of the leads, and can only tunnel off when it is above. As the mechanical oscillation pushes the level downwards through the Fermi energy, there is a small retardation in the time when the electron tunnels on, given by $1/\Gamma$. As the level is pushed back upwards in electrostatic energy by the motion, the electron tunnels off, again with a small time delay. The net result is that electrons are pumped from below the Fermi energy to above it, extracting energy from the mechanical motion, and thus resulting in mechanical damping. Although the retardation time is small compared to the mechanical frequency ($\Gamma \gg \omega_0$), the damping is still large due to the large electromechanical coupling. At finite bias voltage, the same picture applies, but now the damping occurs when the level of the CNT passes by the Fermi energy of each of the left and right lead separately.

At zero temperature and with no broadening of the transition from the tunnel coupling to the leads, the dip in quality factor would be infinitely narrow. Including finite temperature and tunnel coupling of the level to the leads, the dip in quality factor acquires a finite width, and is proportional to the change in average occupation with gate voltage, $\partial\langle N\rangle/\partial V_g$, as shown in Eq. 4.12 in the next subsection. The fact that the quality factor is determined in this way also explains the observed single and double dip structures in the quality factor. At low bias voltage, the charge transition takes place in a single step and consequently there is a single dip in the quality factor. As the bias voltage is increased, the single step changes into two steps with a plateau between them. On the plateau, the change in average occupation with gate voltage, $\partial\langle N\rangle/\partial V_g$, is smaller, leading to a smaller retarded single-electron force acting on the CNT and a smaller reduction of the quality factor. Although a larger current is due to more tunnel events, the CNT does not perform extra work at high bias. As more electrons pass the CNT and reside on it, the retardation time is reduced. What causes the reduction in quality factor is the pumping of the electrons from below the Fermi energy to above it, and the retardation between the electrostatic force and the mechanical motion.

4.5.2 MODEL FOR SINGLE-ELECTRON DAMPING

Using the following model, the quality factor is calculated, as shown in the red lines in the top panels of Figs. 4.6b, 4.6d, and 4.6f. We look at the limit where there are many tunneling events per mechanical oscillation, $\Gamma_{tot} \gg f_0$. As derived in Refs. [26, 37], the total damping has an intrinsic contribution and a contribution due to the displacement-dependent force associated with tunneling electrons:

$$\frac{\omega_0}{Q_{tot}} = \frac{\omega_0}{Q_{int}} + \frac{F_{stoch} V_g}{m C_g} \frac{1}{\Gamma_{tot}} \frac{dC_g}{dx} \frac{\partial\langle N\rangle}{\partial V_g}, \tag{4.12}$$

where Q_{tot} is the total quality factor and Q_{int} is the intrinsic quality factor in the absence of tunneling electrons.

The stochastic force experienced by the CNT, $F_{stoch} = F(N_0+1) - F(N_0)$, is the difference between the force experienced at N_0 and N_0+1 electrons. Assuming that both source and drain voltage are much smaller than the d.c. gate voltage, $V_s, V_d \ll V_g^{dc}$, and taking only into account the d.c. force acting on the electrons as the CNT oscillates (which is valid as long as $V_g^{ac} \ll V_g^{dc}$), Ref. [26] gives the following expression for the stochastic force:

$$F_{stoch} = \frac{1}{C_{tot}^2} \frac{dC_g}{dx} \left(2e(C_S + C_D)V_g + e^2(2N+1)\right). \tag{4.13}$$

Equation (4.12) illustrates how single-electron damping is increased by a large change in average occupation because of mechanical motion, $\partial\langle N\rangle/\partial V_g$, but is reduced by a large total tunnel rate, Γ_{tot}, as the retardation time decreases. In the case that exponential tunnel rates cause $\partial\langle N\rangle/\partial V_g$ to become negative, single-electron tunneling pumps the mechanical motion, leading to self-sustained oscillation (see [37] and section 3.4).

4.5.3 FITTING OF THE EXPERIMENTAL QUALITY FACTOR AND DISCUSSION

The calculated and the measured quality factors, at low bias, are compared in the top panel of Fig. 4.6b, showing quantitative agreement below $V_{g,offset} = 1$ mV, where $V_{g,offset} = V_g - 0.9$ V. At high bias, the top panel of Fig. 4.6d shows an excellent quantitative agreement between the model and the measurement. As a function of bias in the top panel of Fig. 4.6f, the calculated quality factors match the measured quality factors at bias voltages below 1 mV. Above 1 mV, an excited state, as evident in the current in Fig. 4.6e, may be the cause of extra damping.

The bottom panels of Figs. 4.6b, 4.6d, and 4.6f show, in blue dots, the resonance frequency extracted from the frequency responses alongside the quality factors. The decrease in quality factor is accompanied by a decrease in the resonance frequency. The red lines show the resonance frequency calculated with the model as described in the previous section, using the same tunnel rates as for the quality factors. Without changing any fit parameters, we have qualitative agreement as the quality factor dips and the resonance frequency dips occur at corresponding gate voltages. It is not fully understood why agreement between the calculated and measured resonance frequency is not quantitative.

4.6 NONLINEAR RESTORING FORCES DUE TO SINGLE-ELECTRON TUNNELING

In the previous sections, we described linear corrections to the restoring force due to single-electron tunneling, which change the spring constant and cause damping. In this section, we cover nonlinear corrections due to single-electron charge effects (see also Ch. 6), resulting in expressions for the Duffing parameter and the mode coupling parameter.

4.6.1 DUFFING NONLINEARITY DUE TO SINGLE-ELECTRON TUNNELING

Adding nonlinear corrections, the single-electron force is expanded with respect to the displacement, x, as follows:

$$F_{CNT} = -\Delta k_{SET}x - \beta_{SET}x^2 - \alpha_{SET}x^3. \tag{4.14}$$

The β_{SET} parameter and the Duffing parameter, α_{SET}, are calculated as derivatives of the single-electron force:

$$\beta_{SET} = -\frac{1}{2}\frac{d^2F_{CNT}}{dx^2} \tag{4.15}$$

$$\alpha_{SET} = -\frac{1}{6}\frac{d^3F_{CNT}}{dx^3}. \tag{4.16}$$

Expanding the full derivatives into partial partial derivatives as $d/dx = \partial/\partial x + (V_g/C_g)(dC_g/dx)\partial/\partial V_g$, we arrive at:

$$\beta_{SET} = -\frac{1}{2}F_{xx} - \frac{V_g}{C_g}\frac{dC_g}{dx}F_{xg} - \frac{1}{2}\left(\frac{V_g}{C_g}\frac{dC_g}{dx}\right)^2 F_{gg} \tag{4.17}$$

$$\begin{aligned}\alpha_{SET} = &-\frac{1}{6}F_{xxx} - \frac{1}{2}\frac{V_g}{C_g}\frac{dC_g}{dx}F_{xxg} \\ &-\frac{1}{2}\left(\frac{V_g}{C_g}\frac{dC_g}{dx}\right)^2 F_{xgg} - \frac{1}{6}\left(\frac{V_g}{C_g}\frac{dC_g}{dx}\right)^3 F_{ggg}.\end{aligned} \tag{4.18}$$

Here, the subscripts of F denote differentiation with respect to displacement, x, or gate voltage, g.

The quadratic nonlinearity, β_{SET}, renormalizes [56] α_{SET}, leading to an effective Duffing parameter, $\alpha_{eff,SET}$:

$$\alpha_{eff,SET} = \alpha_{SET} + \Delta\alpha_{\beta,SET} = \alpha_{SET} - \frac{10}{9}\frac{\beta_{SET}^2}{m\omega_0^2}. \tag{4.19}$$

For the parameters of the device we study here, there is a leading order dominant contribution, α_{SET}^0, given by:

$$\alpha_{SET}^0 = -\frac{1}{6}\left(\frac{dC_g}{dx}\right)^4\left(\frac{V_g}{C_g}\right)^3\frac{e(V_g - V_{CNT})}{C_{tot}}\frac{\partial^3\langle N\rangle}{\partial V_g^3}, \tag{4.20}$$

which is one of the terms arising from $-1/6((V_g/C_g)(dC_g/dx))^3F_{ggg}$ in Eq. 4.18. Using the same set of parameters as for Figs. 4.4 and 4.5, we repeat the calculated average occupation as displayed in Fig. 4.4a, and we plot $\alpha_{eff,SET}$ and α^0_{SET} together in Fig. 4.7. The figure shows that the other contributions in Eq. 4.18 and the renormalization, $\Delta\alpha_{\beta,SET}$, due to β_{SET}, play no significant role in our device. For completeness, the other contributions, which are more than one order of magnitude smaller than α^0_{SET}, are plotted in Fig. 4.12 in the appendix in section 4.10. The switching of the sign of the Duffing parameter $\alpha_{eff,SET}$, due to the third derivative of the average occupation with respect to gate voltage, is visible in Fig. 4.7 and has been observed experimentally previously (see Ch. 3).

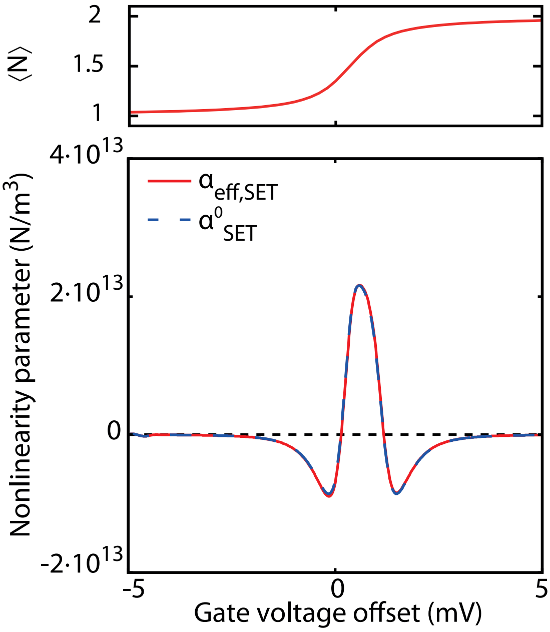

FIGURE 4.7: (top) Average occupation, $\langle N\rangle$, as a function of gate voltage, identical to the top panel of Fig. 4.4a. (bottom) Calculated nonlinearity parameter as a function of gate voltage at $V_b = 0.17$ mV across the Coulomb peak depicted in Fig. 4.2, with its sign flipping from negative to positive to negative again, showing the significance of the α^0_{SET} contribution in $\alpha_{eff,SET}$. Other contributions, including the renormalization, $\Delta\alpha_{\beta,SET}$, due to β_{SET}, are shown to be negligible.

4.6.2 MODE COUPLING DUE TO SINGLE-ELECTRON TUNNELING

In Ch. 5, different bending modes in CNT quantum dot resonators are experimentally shown to have strong coupling, resulting in a shift in the resonance frequency of one mode due to the resonance of another mode. In contrast to top-down micromechanical beams [57] and CNTs outside the Coulomb blockade regime [58], mode coupling in CNT quantum dot resonators is not dominated by tension, but, instead, by single-electron charge effects. In this section, we establish a theoretical framework for single-electron mode coupling. We focus on the leading order nonlinear contribution to the restoring force, arising from $F^0_{SET} = -\alpha^0_{SET}x^3$, and write it in terms of the change in capacitance, δC_g, due to mechanical motion:

$$F^0_{SET} = -\mathscr{B}(V_g)\frac{\partial^3\langle N\rangle}{\partial V_g^3}\frac{dC_g}{dx}(\delta C_g)^3, \tag{4.21}$$

where, for brevity, we capture the slowly varying dependence on gate voltage in $\mathscr{B}(V_g) = \frac{1}{6}\left(\frac{V_g}{C_g}\right)^3\frac{e(V_g - V_{CNT})}{C_{tot}}$. The change in capacitance due to mechanical motion depends on the mode shape:

$$\delta C_g = \int_0^L \frac{dc_g}{du}\left(\sum_n u_n(z)\cos(\omega_n t)\right)dz, \tag{4.22}$$

where dc_g/du is the change in capacitance per unit length with respect to the amplitude $u(z)$ at position z along the CNT. We use the infinite cylinder parallel to a plate model [59], and assume that dc_g/du is independent of the position, z, along the CNT. The position-dependent amplitude, $u_n(z)$ is given by:

$$u_n(z) = x_n\xi_n(z), \tag{4.23}$$

where the mode shapes, $\xi_n(z)$, are orthonormalized as $\int_0^L \xi_i(z)\xi_j(z)dz = L\delta_{ij}$ with δ_{ij} the Kronecker delta, such that the amplitude x represents the root-mean-squared amplitude over the length of the CNT (not over time). With this definition of the amplitude [11], the mass of each mode is given by the total mass and the spring constant is given by $k_n = m\omega_n^2$. The change in gate capacitance due to the mechanical motion is simplified to:

$$\delta C_g = L\frac{dc_g}{du}\sum_n x_n a_n\cos(\omega_n t), \tag{4.24}$$

with the first four elements of $a_n = (1/L)\int_0^L \xi_n(z)dz$ calculated [11] for a bending-rigidity dominated beam to be 0.83, 0, 0.36, and 0. The leading order nonlinear term, F^0_{SET} is expanded as:

$$\begin{aligned} F^0_{SET} = &-\mathscr{B}(V_g)\frac{\partial^3\langle N\rangle}{\partial V_g^3}\mathscr{C}(\{x_i\}) \\ &\times\sum_{m,n} a_m^2 x_m^2\left(\frac{1}{2}+\frac{1}{2}\cos(2\omega_m t)\right)a_n x_n\cos\omega_n t, \end{aligned} \tag{4.25}$$

where we have used $\mathscr{C}(\{x_i\}) = (Ldc_g/du)^4(\sum_i a_i x_i)/\sum x_i$.

We address several terms in this expression. The terms containing $(1/2)\cos(2\omega_m t)$ give rise to parametric excitation due to single-electron effects. The terms not containing $(1/2)\cos(2\omega_m t)$, while having $m = n$, lead to the Duffing nonlinearity of mode 1 and 3, as described in the previous subsection. Single-electron mode coupling is brought about through the terms not containing $(1/2)\cos(2\omega_m t)$, while having $m \neq n$, as the amplitude of one mode changes the spring constant of another mode. The change in resonance frequency of mode m due to the resonance of mode n is then given by:

$$\frac{\Delta\omega_m}{x_n^2} = -\frac{1}{4m\omega_m}\mathscr{B}(V_g)\frac{\partial^3\langle N\rangle}{\partial V_g^3}\mathscr{C}(x_m, x_n)a_n^2 a_m. \tag{4.26}$$

As the sign of $\partial^3\langle N\rangle/\partial V_g^3$ goes from positive, to negative, to positive again, across a Coulomb peak, mode coupling causes softening, then stiffening, and then softening, in the CNT spring. The change in sign from mode coupling across a Coulomb peak arises from the mechanically modulated average charge in the same way as the sign of the Duffing nonlinearity does.

4.7 ADDITIONAL EXPERIMENTAL OBSERVATIONS OF SINGLE-ELECTRON SPRING AND DAMPING EFFECTS

In sections 4.4 and 4.5, we showed how the resonance frequency and the quality factor decrease as the average charge on the CNT is modulated through mechanical oscillation. How much the average charge changes is determined by $\partial\langle N\rangle/\partial V_g$, which in turn depends on the broadening Γ_{broad} due to tunnel coupling to the leads. First, in subsection 4.7.1, we show that, by tuning the tunnel rates through magnetic field, the dips in resonance frequency and quality factor are influenced significantly, and in a way that is in qualitative agreement with the physical picture of the damping and frequency shifts from our model. In subsection 4.7.2, a step in the average charge caused by an excited state of the CNT is presented to lead to a decrease in the resonance frequency, demonstrating detection of the excited state of the quantum dot using the mechanical resonator. Finally, in subsection 4.7.3, we demonstrate that the single electron spring and damping effects we observe are indeed originating from Coulomb blockade, by studying the gate dependence of the resonance frequency in the Fabry-Pérot conductance regime. In this regime, the charge on the suspended CNT segment is no longer quantized, and we no longer observe dips in the mechanical frequency as we sweep the gate.

4.7.1 RESONANCE FREQUENCY SHIFTS AND DAMPING VIA MAGNETIC-FIELD DEPENDENT TUNNEL RATES

In this subsection, we examine the quality factor and mechanical frequency as a function of the tunnel rates of the quantum dot. We tune the tunnel barriers of the quantum dot in a somewhat unconventional way by using a magnetic field parallel to the CNT.

The tuning of the tunnel barriers by magnetic field occurs through the parallel magnetic field's influence on the bandgap of the CNT. Figure 4.8a shows the current flowing through the CNT as a function of gate voltage and magnetic field parallel to the CNT. The increase in the bandgap is visible as an increase in the gate voltage range between the hole current and the first Coulomb peak, which can be seen clearly by the trajectory of the first Coulomb peak in Fig. 4.8b. Also, as the magnetic field is increased, the width and the magnitude of the Coulomb peaks decreases. This decrease in the Coulomb peak width is a result of an increase in the p-n junction tunnel barrier height by the increased bandgap at higher magnetic fields.

The increase of the bandgap with an increasing parallel magnetic field can be explained as follows [60]. A parallel magnetic field changes the quantized wavevectors $k_\perp$ of the electrons along the circumference of the CNT through an Aharonov-Bohm term. The band structure of the CNT is determined by taking a cross-section of the Dirac cone at a constant $k_\perp$. Figure 4.8c shows the quantized wavevectors $k_\perp$ intersecting with the Dirac cones. Figure 4.8d illustrates how the bandgap is changed through a parallel magnetic field. The height of the tunnel barrier is determined by the bandgap of the CNT, through the p-n junction that is formed at the interface of the metal and the CNT. In general, the shift of the quantization lines with magnetic field decreases the bandgap. This occurs only up until a magnetic field B_{Dirac}, at which point the quantization line crossing the Dirac point and the bandgap begins to increase again. From the orbital magnetic moment we observe of 1.0 meV/T, together with the bandgap of $E_g = 58$ meV at zero magnetic field, this should occur at a very large magnetic field of 29 T. Similar to previous reports [61], we observe that the quantization line crosses the Dirac point at a magnetic field much smaller than expected, in this case at 0.6 T. At a magnetic field above B_{Dirac}, the p-n junction tunnel barriers to the quantum dot increase in height, and the tunnel rates to the quantum dot are significantly reduced.

The tunnel rate of the quantum dot to the leads as a function of magnetic field, $\Gamma_{broad}(B)$, is determined from the observed width of the Coulomb peaks. Figure 4.9a shows the tunnel coupling as a function of parallel magnetic field, decreasing with an order of magnitude. To determine the tunnel coupling, a Lorentzian fit, similar to Eq. 4.2, was performed on the Coulomb peak at $V_b = 0.3$ mV.

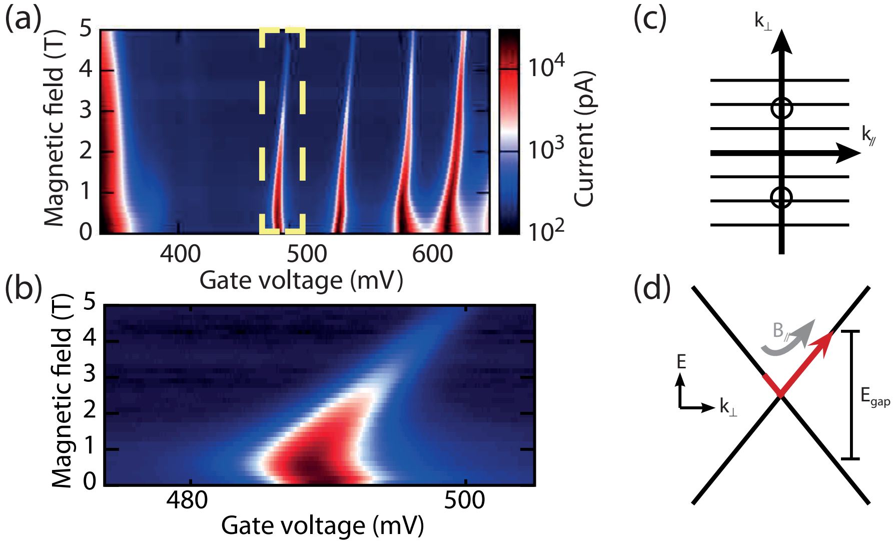

FIGURE 4.8: (a) Current as a function of gate voltage and parallel magnetic field, showing a decrease in the height and width of the Coulomb peaks and a shift of the Coulomb peaks with increasing magnetic field for the first four charge states. The yellow dashed box denotes the region shown in 4.8b. (b) Current as a function of gate voltage and parallel magnetic field, showing the shift of the transition from 0 to 1 electrons with magnetic field (c) Cross-section of the Dirac cones of a CNT at a constant energy as a function of $k_\perp$ and $k_\parallel$, showing the intersection of the quantized $k_\perp$ with the Dirac cones. (d) Cross-section of a Dirac cone of a CNT, showing the change in the bandgap, E_{gap}, as the parallel magnetic field alters $k_\perp$.

In Figs. 4.9b and 4.9c, the resonance frequency and quality factor as a function of parallel magnetic field are shown, respectively. The resonance frequency and quality factor are determined by taking a frequency response at the top of the Coulomb peak of the charge transition from 7 to 8 electrons, at a low bias voltage of $V_b = 0.3$ mV. Between 0 T and 9 T, the reduction of the tunnel coupling with a parallel magnetic field causes the resonance frequency to decrease by ~1 MHz. At a magnetic field of 9 T, the quality factor has decreased by a factor of ~200, compared to zero magnetic field.

The decrease in resonance frequency and quality factor with magnetic field can be explained as follows. As the tunnel coupling is decreased through a parallel magnetic field, the charge transition takes place in a smaller range of gate voltage, yielding a larger slope $\partial\langle N\rangle/\partial V_g$. The larger change in the displacement-dependent force acting on the CNT during a mechanical oscillation causes a larger change in spring constant and therefore in resonance frequency. Also, the asymmetry of the CNT level between being above and below the Fermi level of the leads is sharper, leading to a larger retarded single-electron force acting on the CNT, and consequently a lower quality factor.

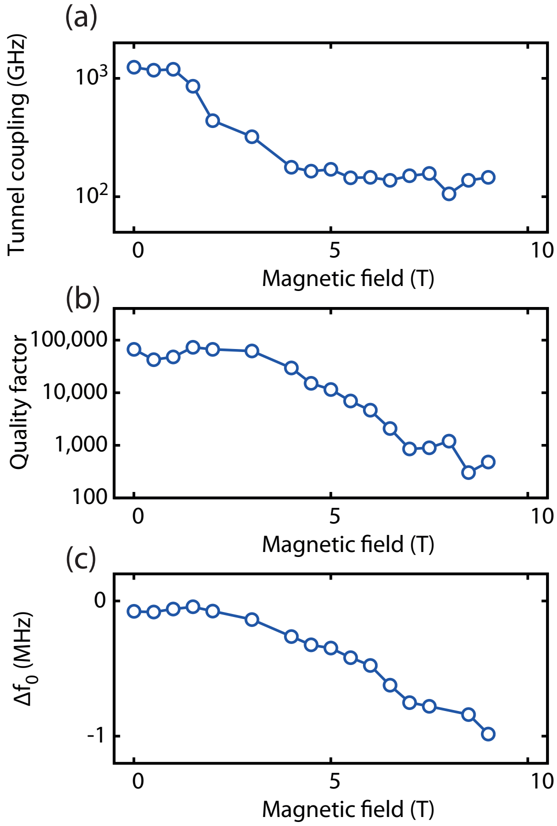

FIGURE 4.9: (a) Broadening due to tunnel coupling as a function of magnetic field, showing a decrease in broadening with increasing magnetic field. (b) Quality factor on the Coulomb peak of the 7 to 8 transition at $V_b = 0.3$ mV showing the quality factor decreasing by two orders of magnitude with increasing magnetic field. (c) Shift in resonance frequency on the Coulomb peak of the 7 to 8 transition at $V_b = 0.3$ mV, showing a decrease of ~1 MHz.

The decrease in quality factor with magnetic field has to be put in contrast with the recently observed magnetic damping in CNT resonators [19]. Damping in Ref. [19] is measured with a CNT placed perpendicular, not parallel, to the magnetic field. There, Lorentz forces are the cause of damping, due to the perpendicular orientation of eddy currents flowing through the CNT with respect to the magnetic field. In this Chapter, damping is increased as the magnetic field reduces the level broadening by increasing the band gap, and the modulation of the average charge due to the mechanical motion is increased.

4.7.2 MECHANICAL DETECTION OF AN EXCITED STATE

In this subsection, we demonstrate that the presence of excited states of the quantum dot inside the bias window can also result in frequency shifts of the mechanical resonator. Figure 4.10a shows the differential conductance, dI/dV_b, as a function of bias and gate voltage in the charge transition from 0 to 1 electron in a stability diagram of a different device (B). An excited electronic state of the CNT is visible as a diagonal line inside the single-electron tunneling region at negative bias. Because of charging effects, it is not possible for both states to be occupied by an electron; current still takes place through single-electron tunneling, but now can occur through two channels: through both the ground state and the excited state. This means that the rate to tunnel onto the quantum dot, Γ^+, has increased. When both states are allowed for tunneling, the current increases in a step, leading to a high dI/dV_b, as visible in the stability diagram.

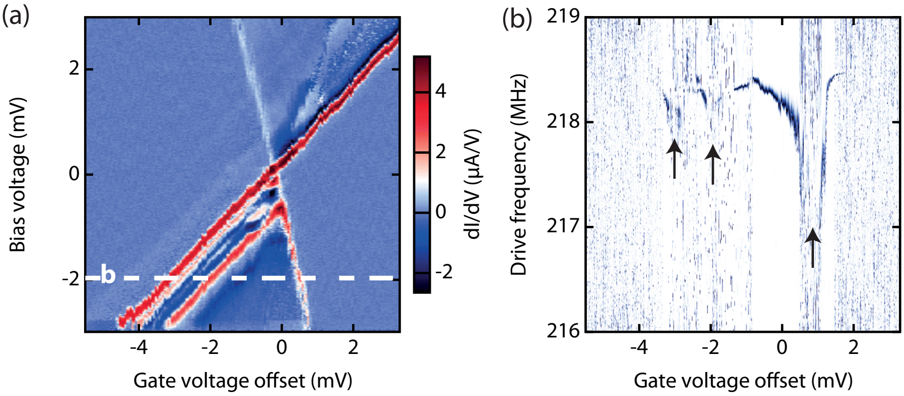

FIGURE 4.10: (a) Stability diagram at $V_g = 293$ mV of device B, showing an excited state as a diagonal line at negative bias voltage inside the single-electron tunneling region. (b) $|I - I_0|/|I - I_0|_{max}$ as a function of drive frequency and gate voltage offset at $V_b = -2$ mV, showing three dips in resonance frequency, indicated by black arrows, with the middle dip corresponding to the excited state.

The influence of the excited state on the mechanical motion of the CNT is examined through a measurement of the normalized current as a function of gate voltage and drive frequency at a bias voltage of -2 mV, shown in Fig. 4.10b. Three dips in resonance frequency can be seen: the leftmost and rightmost correspond to the chemical potential of the ground state aligning with the Fermi level of the source and drain, respectively. The middle dip corresponds to the chemical potential of the excited state aligning with the Fermi level of the drain. At this gate voltage, the excited state causes the rate to tunnel onto the CNT to increase, whereas the rate to tunnel off the CNT remains the same. This leads to a step in the average charge residing on the CNT. As with the ground state, tunneling through the excited state causes the CNT to experience a displacement-dependent force as it oscillates, resulting in a frequency dip.

4.7.3 ABSENCE OF SINGLE-ELECTRON SPRING EFFECTS IN THE FABRY-PÉROT REGIME

In this subsection, we examine the regime of low tunnel resistance R_T for its influence on the mechanical motion by looking at the Fabry-Pérot regime [50], for which $R_T < e^2/h$. For quantum dots with large tunnel barriers ($R_T > e^2/h$), the charge on the quantum dot is quantized. For sufficiently transparent barriers with $R_T < e^2/h$, however, Coulomb blockade is destroyed by quantum fluctuations of the charge, and charge on the quantum dot is no longer quantized. In this regime, the conductance as a function of gate voltage still oscillates due to electronic Fabry-Pérot interferences, but the charge quantization is lost. The top figure of Fig. 4.11 shows Fabry-Pérot oscillations in the measured voltage across the CNT as a function of gate voltage using a four terminal current bias measurement of device B. The bottom figure of Fig. 4.11 displays the measured mechanical resonance frequency as a function of gate voltage and drive frequency. Visible in the plot is an increase in the resonance frequency as gate voltage is decreased, resulting from the electrostatic force from the gate that induces tension in the CNT. However, frequency dips do not occur at a Fabry-Pérot oscillation. This is because the Fabry-Pérot oscillations, in contrast to Coulomb oscillations, are not associated with discrete steps in the average charge. Softening due to the electrostatic force on the CNT quantum dot is therefore constant (or very slowly varying) across the entire gate range, and no frequency dips occur.

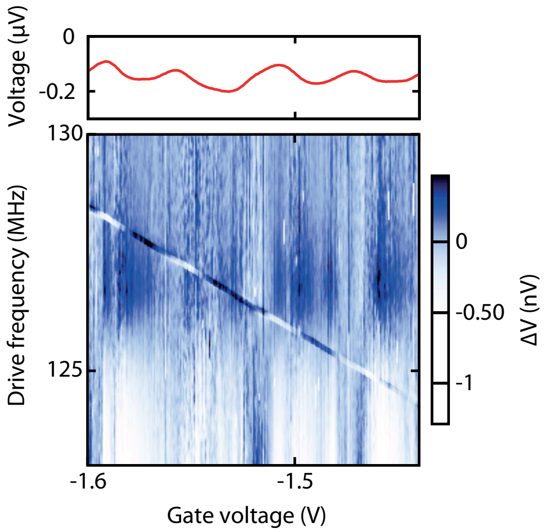

FIGURE 4.11: (top) Voltage measured across the CNT in a four-terminal current-bias configuration as a function of gate voltage, showing Fabry-Pérot oscillations at a bias current of -20 nA. (bottom) Change in measured voltage as a function of drive frequency and gate voltage, showing the tuning of the mechanical resonance frequency with tension arising from the gate.

4.8 CONCLUSIONS

To conclude, we have found quantitative agreement between the experimental observation of single-electron effects on the resonance frequency and quality factor of a CNT quantum dot resonator, and a theoretical model. This allows the mechanical motion of a suspended CNT quantum dot to be used as a probe to detect its average charge. It is found that the mechanical resonance frequency and quality factor are reduced as the average charge changes the electrostatic force during a mechanical oscillation. At high bias, a double dip structure arises for both the resonance frequency and the quality factor, which is quantitatively supported by the model. A model, describing single-electron induced Duffing nonlinearity and mode coupling, leads to the finding of a single significant contribution. Additional experiments illustrating the model show that, by tuning the tunnel rates, the resonance frequency is reduced by ~1 MHz, and the quality factor by a factor of ~200. The increase of the average charge due to tunneling through an excited state of the CNT also leads to a reduction of the resonance frequency. The occurrence of frequency dips in the Fabry-Pérot regime is excluded due to the absence of steps in average charge.

Acknowledgements: We acknowledge the financial support of the FET programme of the European Commission, under the FET-Open project QNEMS (233992), and the Foundation for Fundamental Research on Matter (FOM).

4.9 APPENDIX: PARAMETERS USED IN THE MODEL

For the quantitative fits describing the resonance frequency, quality factor, and nonlinearity parameters in Figs. 4.4, 4.5, 4.6, 4.7, and 4.12, the following parameters were used.

Device properties

m	$2.6 \cdot 10^{-21}$ kg
f_0	286.82 MHz
C_g	2.9 aF

Model parameters

Figure	4.4, 4.5, 4.7, and 4.12	4.6
Γ_{broad}	450 GHz	540 GHz
C_{tot}	8.2 aF	12.3 aF
dC_g/dx	-6.5 zF/nm	-5.2 zF/nm
Q_{int}	-	100,000
N_0	1	7
$B_\parallel$	0 T	8 T
V_g	0.565 V	0.9 V
a_L	140 GHz	22 GHz
a_R	170 GHz	22 GHz
b_L	288 /eV	20 /eV
b_R	288 /eV	20 /eV

TABLE 4.1: Properties of device A and parameters that were used for the quantitative fits and the calculations in this Chapter.

4.10 APPENDIX: OTHER SINGLE-ELECTRON CONTRIBUTIONS TO THE DUFFING PARAMETER

In subsection 4.6.1, we discussed the different single-electron contributions to the Duffing parameter, arriving at the dominance of the leading order term α^0_{SET}. Figure 4.12 shows that the other contributions to the single-electron Duffing parameter are more than one order of magnitude smaller and can be neglected. We use the notation where α_{ijk} is the contribution to α_{SET} resulting from the term with F_{ijk} in Eq. 4.18.

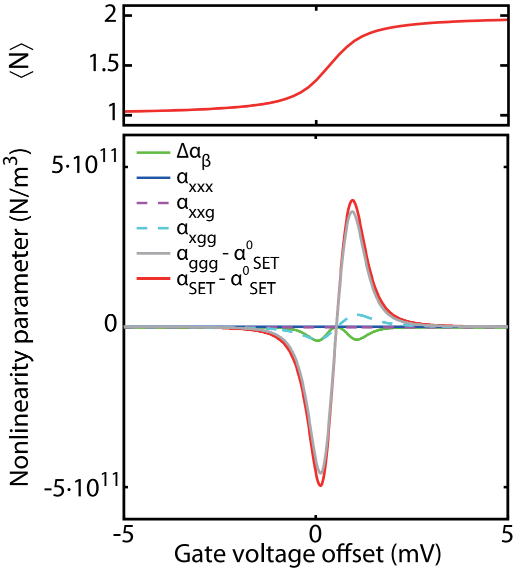

FIGURE 4.12: (top) Average occupation, ⟨N⟩, as a function of gate voltage, identical to the top panel of Fig. 4.4a. (bottom) Other calculated contributions to the nonlinearity parameter, which are shown to be more than one order of magnitude smaller than α^0_{SET}.

REFERENCES

[1] H. B. Meerwaldt, G. Labadze, B. H. Schneider, A. Taspinar, Y. M. Blanter, H. S. J. van der Zant, and G. A. Steele, *Probing the charge of a quantum dot with a nanomechanical resonator*, Physical Review B **86**, 115454 (2012).

[2] H. G. Craighead, *Nanoelectromechanical systems*, Science **290**, 1532 (2000).

[3] K. L. Ekinci and M. L. Roukes, *Nanoelectromechanical systems*, Review of Scientific Instruments **76**, 061101 (2005).

[4] N. V. Lavrik and P. G. Datskos, *Femtogram mass detection using photothermally actuated nanomechanical resonators*, Applied Physics Letters **82**, 2697 (2003).

[5] K. L. Ekinci, X. M. H. Huang, and M. L. Roukes, *Ultrasensitive nanoelectromechanical mass detection*, Applied Physics Letters **84**, 4469 (2004).

[6] B. Lassagne, D. Garcia-Sanchez, A. Aguasca, and A. Bachtold, *Ultrasensitive mass sensing with a nanotube electromechanical resonator*, Nano Letters **8(11)**, 3735 (2008).

[7] K. C. Schwab and M. L. Roukes, *Putting mechanics into quantum mechanics*, Physics Today **58**, 36 (2005).

[8] A. D. O'Connell, M. Hofheinz, M. Ansmann, R. C. Bialczak, M. Lenander, E. Lucero, M. Neeley, D. Sank, H. Wang, M. Weides, et al., *Quantum ground state and single-phonon control of a mechanical resonator*, Nature **464**, 697 (2010).

[9] J. D. Teufel, T. Donner, D. Li, J. W. Harlow, M. S. Allman, K. Cicak, A. J. Sirois, J. D. Whittaker, K. W. Lehnert, and R. W. Simmonds, *Sideband cooling of micromechanical motion to the quantum ground state*, Nature **475**, 359 (2011).

[10] J. Chan, T. P. Mayer Alegre, A. H. Safavi-Naeini, J. T. Hill, A. Krause, S. Groeblacher, M. Aspelmeyer, and O. Painter, *Laser cooling of a nanomechanical oscillator into its quantum ground state*, Nature **478**, 89 (2011).

[11] M. Poot and H. S. J. van der Zant, *Mechanical systems in the quantum regime*, Physics Reports-Review Section of Physics Letters **511**, 273 (2012).

[12] R. G. Knobel and A. N. Cleland, *Nanometre-scale displacement sensing using a single electron transistor*, Nature **424**, 291 (2003).

[13] M. D. LaHaye, O. Buu, B. Camarota, and K. C. Schwab, *Approaching the quantum limit of a nanomechanical resonator*, Science **304**, 74 (2004).

[14] A. Naik, O. Buu, M. D. LaHaye, A. D. Armour, A. A. Clerk, M. P. Blencowe, and K. C. Schwab, *Cooling a nanomechanical resonator with quantum backaction*, Nature **443**, 193 (2006).

[15] D. R. Koenig, E. M. Weig, and J. P. Kotthaus, *Ultrasonically driven nanomechanical single-electron shuttle*, Nature Nanotechnology **3**, 482 (2008).

[16] V. Sazonova, Y. Yaish, H. Ustunel, D. Roundy, T. A. Arias, and P. L. McEuen, *A tunable carbon nanotube electromechanical oscillator*, Nature **431**, 284 (2004).

[17] A. K. Hüttel, G. A. Steele, B. Witkamp, M. Poot, L. P. Kouwenhoven, and H. S. J. van der Zant, *Carbon Nanotubes as Ultrahigh Quality Factor Mechanical Resonators*, Nano Letters **9**, 2547 (2009).

[18] A. Eichler, J. Chaste, J. Moser, and A. Bachtold, *Parametric Amplification and Self-Oscillation in a Nanotube Mechanical Resonator*, Nano Letters **11**, 2699 (2011).

[19] D. R. Schmid, P. L. Stiller, C. Strunk, and A. K. Hüttel, *Magnetic damping of a carbon nanotube nano-electromechanical resonator*, New Journal of Physics **14**, 083024 (2012).

[20] S. J. Tans, M. H. Devoret, H. J. Dai, A. Thess, R. E. Smalley, L. J. Geerligs, and C. Dekker, *Individual single-wall carbon nanotubes as quantum wires*, Nature **386**, 474 (1997).

[21] M. Bockrath, D. H. Cobden, P. L. McEuen, N. G. Chopra, A. Zettl, A. Thess, and R. E. Smalley, *Single-electron transport in ropes of carbon nanotubes*, Science **275**, 1922 (1997).

[22] B. Lassagne, Y. Tarakanov, J. Kinaret, D. Garcia-Sanchez, and A. Bachtold, *Coupling Mechanics to Charge Transport in Carbon Nanotube Mechanical Resonators*, Science **325**, 1107 (2009).

[23] C. B. Doiron, W. Belzig, and C. Bruder, *Electrical transport through a single-electron transistor strongly coupled to an oscillator*, Physical Review B **74**, 205336 (2006).

[24] N. M. Chtchelkatchev, W. Belzig, and C. Bruder, *Charge transport through a single-electron transistor with a mechanically oscillating island*, Physical Review B **70**, 193305 (2004).

[25] A. D. Armour, M. P. Blencowe, and Y. Zhang, *Classical dynamics of a nanomechanical resonator coupled to a single-electron transistor*, Physical Review B **69**, 125313 (2004).

[26] G. Labadze and Y. M. Blanter, *Current response of ac-driven nanoelectromechanical systems in single-electron tunnelling regime* (2011), URL `http://arxiv.org/abs/1007.5186`.

[27] A. D. Armour, *Current noise of a single-electron transistor coupled to a nanomechanical resonator*, Physical Review B **70**, 165315 (2004).

[28] A. A. Clerk and S. Bennett, *Quantum nanoelectromechanics with electrons, quasi-particles and Cooper pairs: effective bath descriptions and strong feedback effects*, New Journal of Physics **7**, 238 (2005).

[29] C. Flindt, T. Novotny, and A. P. Jauho, *Full counting statistics of nano-electromechanical systems*, Europhysics Letters **69**, 475 (2005).

[30] J. Brueggemann, G. Weick, F. Pistolesi, and F. von Oppen, *Large current noise in nanoelectromechanical systems close to continuous mechanical instabilities*, Physical Review B **85**, 125441 (2012).

[31] D. Mozyrsky, I. Martin, and M. B. Hastings, *Quantum-limited sensitivity of single-electron-transistor-based displacement detectors*, Physical Review Letters **92**, 018303 (2004).

[32] D. A. Rodrigues and A. D. Armour, *Quantum master equation descriptions of a nanomechanical resonator coupled to a single-electron transistor*, New Journal of Physics **7**, 251 (2005).

[33] A. Nocera, C. A. Perroni, V. M. Ramaglia, and V. Cataudella, *Probing nonlinear mechanical effects through electronic currents: The case of a nanomechanical resonator acting as an electronic transistor*, Physical Review B **86**, 035420 (2012).

[34] D. A. Rodrigues, J. Imbers, T. J. Harvey, and A. D. Armour, *Dynamical instabilities of a resonator driven by a superconducting single-electron transistor*, New Journal of Physics **9**, 84 (2007).

[35] S. D. Bennett, L. Cockins, Y. Miyahara, P. Gruetter, and A. A. Clerk, *Strong Electromechanical Coupling of an Atomic Force Microscope Cantilever to a Quantum Dot*, Physical Review Letters **104**, 017203 (2010).

[36] T. Ojanen, F. C. Gethmann, and F. von Oppen, *Electromechanical instability in vibrating quantum dots with effectively negative charging energy*, Physical Review B **80**, 195103 (2009).

[37] O. Usmani, Y. M. Blanter, and Y. V. Nazarov, *Strong feedback and current noise in nanoelectromechanical systems*, Physical Review B **75**, 195312 (2007).

[38] R. El Boubsi, O. Usmani, and Y. M. Blanter, *Mechanical feedback in the high-frequency limit*, New Journal of Physics **10**, 095011 (2008).

[39] D. Midtvedt, Y. Tarakanov, and J. Kinaret, *Parametric Resonance in Nanoelectromechanical Single Electron Transistors*, Nano Letters **11**, 1439 (2011).

[40] E. Mariani and F. von Oppen, *Electron-vibron coupling in suspended carbon nanotube quantum dots*, Physical Review B **80**, 155411 (2009).

[41] L. Y. Gorelik, A. Isacsson, M. V. Voinova, B. Kasemo, R. I. Shekhter, and M. Jonson, *Shuttle mechanism for charge transfer in Coulomb blockade nanostructures*, Physical Review Letters **80**, 4526 (1998).

[42] A. D. Armour and A. MacKinnon, *Transport via a quantum shuttle*, Physical Review B **66**, 035333 (2002).

[43] F. Pistolesi and R. Fazio, *Charge shuttle as a nanomechanical rectifier*, Physical Review Letters **94**, 036806 (2005).

[44] C. Huldt and J. M. Kinaret, *Multiscale modelling of a nanoelectromechanical shuttle*, New Journal of Physics **9**, 51 (2007).

[45] A. D. Armour, M. P. Blencowe, and K. C. Schwab, *Entanglement and decoherence of a micromechanical resonator via coupling to a Cooper-pair box*, Physical Review Letters **88**, 148301 (2002).

[46] A. D. Armour and M. P. Blencowe, *Probing the quantum coherence of a nanomechanical resonator using a superconducting qubit: I. Echo scheme*, New Journal of Physics **10**, 095004 (2008).

[47] M. P. Blencowe and A. D. Armour, *Probing the quantum coherence of a nanomechanical resonator using a superconducting qubit: II. Implementation*, New Journal of Physics **10**, 095005 (2008).

[48] G. A. Steele, G. Gotz, and L. P. Kouwenhoven, *Tunable few-electron double quantum dots and Klein tunnelling in ultraclean carbon nanotubes*, Nature Nanotechnology **4**, 363 (2009).

[49] J. Kong, H. T. Soh, A. M. Cassell, C. F. Quate, and H. J. Dai, *Synthesis of individual single-walled carbon nanotubes on patterned silicon wafers*, Nature **395**, 878 (1998).

[50] W. J. Liang, M. Bockrath, D. Bozovic, J. H. Hafner, M. Tinkham, and H. Park, *Fabry-Perot interference in a nanotube electron waveguide*, Nature **411**, 665 (2001).

[51] C. W. J. Beenakker, *Theory Of Coulomb-Blockade Oscillations In The Conductance Of A Quantum Dot*, Physical Review B **44**, 1646 (1991).

[52] J. M. Thijssen and H. S. J. Van der Zant, *Charge transport and single-electron effects in nanoscale systems*, Physica Status Solidi B-Basic Solid State Physics **245**, 1455 (2008).

[53] A. N. Korotkov and Y. V. Nazarov, *Single-Electron Tunneling Coexisting With The Barrier Suppression*, Physica B **173**, 217 (1991).

[54] M. Brink, Ph.D. thesis, Cornell University (2007), URL `http://hdl.handle.net/1813/3668`.

[55] Y. V. Nazarov and Y. M. Blanter, *Quantum transport: Introduction to nanoscience* (Cambridge University Press Cambridge, UK, 2009).

[56] R. Lifshitz and M. C. Cross, *Review of nonlinear dynamics and complexity* (John Wiley and Sons, New York,, 2008), chap. Nonlinear dynamics of nanomechanical and micromechanical resonators, URL `http://bitly.com/ZdtfxJ`.

[57] H. J. R. Westra, M. Poot, H. S. J. van der Zant, and W. J. Venstra, *Nonlinear modal interactions in clamped-clamped mechanical resonators.*, Physical Review Letters **105**, 117205 (2010).

[58] A. Eichler, M. del Álamo Ruiz, J. A. Plaza, and A. Bachtold, *Strong coupling between mechanical modes in a nanotube resonator*, Physical Review Letters **109**, 25503 (2012).

[59] S. Sapmaz, Y. M. Blanter, L. Gurevich, and H. S. J. van der Zant, *Carbon nanotubes as nanoelectromechanical systems*, Physical Review B **67**, 235414 (2003).

[60] E. D. Minot, Y. Yaish, V. Sazonova, and P. L. McEuen, *Determination of electron orbital magnetic moments in carbon nanotubes*, Nature **428**, 536 (2004).

[61] V. V. Deshpande, B. Chandra, R. Caldwell, D. S. Novikov, J. Hone, and M. Bockrath, *Mott Insulating State in Ultraclean Carbon Nanotubes*, Science **323**, 106 (2009).

5

STRONG AND TUNABLE MODE COUPLING IN CARBON NANOTUBE RESONATORS

A. Castellanos-Gomez, H. B. Meerwaldt, W. J. Venstra, H. S. J. van der Zant, and G. A. Steele

The nonlinear interaction between two mechanical resonances of the same freely suspended carbon nanotube resonator is studied. We find that in the Coulomb blockade regime, the nonlinear modal interaction is dominated by single-electron-tunneling processes, and that the mode-coupling parameter can be tuned with the gate voltage, allowing both mode softening and mode stiffening behavior. This is in striking contrast to tension-induced mode coupling in strings, where the coupling parameter is positive and gives rise to a stiffening of the mode. The strength of the mode coupling in carbon nanotubes in the Coulomb blockade regime is observed to be six orders of magnitude larger than the mechanical mode coupling in micromechanical resonators.

This Chapter has been published in Phys. Rev. B **86**, 041402 (2012) [1].

Carbon nanotubes present remarkable properties for applications in nanoelectromechanical systems (NEMS) such as low mass density, high Young's modulus and high crystallinity [2, 3]. This fact has motivated the use of carbon nanotubes to fabricate high-quality factor (Q) mechanical resonators [4] that can be operated at ultrahigh frequencies [5, 6] and can be used as ultrasensitive mass sensors [7–9]. Additionally, both the mechanical tension and electrical properties of carbon nanotubes can be tuned to a large extent by an external electric field [10], making nanotubes a very versatile component in NEMS devices.

Due to the small diameter of carbon nanotubes, they can be easily excited into the nonlinear oscillation regime [11]. Moreover, it has been demonstrated that the nonlinear dynamics of carbon nanotubes can be tuned over a large range (see [12] and Ch. 3) making nanotube NEMS excellent candidates for the implementation of sensing schemes based on nonlinearity and for the study of fundamental problems on nonlinear dynamics. The nonlinear interaction between mechanical resonance modes is interesting both from a fundamental and from an applied perspective. Nonlinear modal interactions have been studied recently in micro- and nanoresonators [13–18]. These studies concentrated on mechanical coupling between the modes via the geometric nonlinearity or via the displacement-induced-tension, the same mechanism responsible for the Duffing nonlinearity in doubly-clamped resonators. By employing a different mode of the same resonator as a phonon cavity, the mechanical mode can be controlled in-situ, and its damping characteristics can be modified to a great extent, leading to cooling of the mode and parametric mode splitting [13, 16]. The nonlinear coupling can be also used to detect resonance modes that would otherwise be inaccessible by the experiment [18] to increase the dynamic range of resonators by tuning the nonlinearity constant [18], and for mechanical frequency conversion [17]. Additionally, nonlinear coupling has been proposed as a quantum non-demolition scheme to probe mechanical resonators in their quantum ground state [19] and as a way of generating entanglement between different mechanical modes [20]. Furthermore, recent theoretical work suggests that the interaction between mechanical resonances could be responsible for the spectral broadening in carbon nanotubes, thus limiting their Q-factor at room temperature [21]. Despite the interest aroused by the modal interaction in nanotube resonators recently, experimental studies in this field are scarce.

Here, we study the nonlinear interaction between two different eigenmodes of a freely suspended carbon nanotube resonators at low temperatures, using a quantum dot embedded in the nanotube as a detector. We find that, for nanotube resonators in the Coulomb blockade regime, the nonlinear modal interaction is dominated by single-electron-tunneling processes, as opposed to displacement-induced tension. A strongly enhanced mode coupling is observed in the Coulomb-blockade regime, which is orders of magnitude larger than in conventional microresonators. Furthermore, in the Coulomb-blockade regime, the mode-coupling parameter can be tuned by adjusting the gate voltage, oscillating in sign over a gate range of only a few millivolts. This allows both mode softening and mode stiffening behavior, in contrast to the case of tension-induced mechanical coupling in strings, where the coupling parameter is positive and gives rise to a stiffening of the mode.

5.1 DETECTION AND MECHANICAL CHARACTERISTICS

The device consists of a single-wall carbon nanotube suspended across a trench, bridging two metal electrodes (Fig. 5.1a). Electrons are confined in the nanotube by Schottky barriers at the metal contacts, forming a quantum dot in the suspended segment. The nanotube is grown in the last step of the fabrication process, yielding ultraclean devices which can have large quality factors. We perform all measurements in a dilution fridge at 20 mK. The carbon nanotube is actuated with a nearby antenna (separated about 2 cm from the sample). The detection of the resonator motion is carried out by monitoring the DC current while the nanotube is driven by the antenna. When the carbon nanotube is driven at resonance, its oscillation changes the capacitance between the nanotube and the gate, leading to an effective oscillating gate voltage which smears out the Coulomb peaks and thus yields a change in the DC current through the nanotube. More details concerning this oscillation amplitude readout method, referred to here as the rectification method, can be found in Chapter 2.

Figures 5.1b and 5.1c show two peaks in the DC current through the carbon nanotube that occur when the nearby antenna is driven at frequencies that match the mechanical resonances of the carbon nanotube (hereafter labeled mode A and mode B, respectively). The resonance frequencies of a clamped-clamped beam are calculated by Euler-Bernoulli theory as $f_n = \frac{\beta_n r}{4\pi}\sqrt{\frac{E}{\rho}}$, with $\beta_n \cdot L$ =4.73, 7.85, 11.00, etc. Taking the Young's modulus $E = 1.3$ TPa, the tube radius $r = 1$ nm, the length of the suspended part of the tube $L = 600$ nm and its mass density $\rho = 1400\,\mathrm{kg/m^3}$, the resonance frequencies of the lowest three modes are $f_1 = 151$ MHz, $f_2 = 415$ MHz and $f_3 = 814$ MHz. These values correspond well with the measured resonance frequencies, $f_A = 175$ MHz and $f_B = 957$ MHz, indicating that the restoring force is dominated by the nanotube bending rigidity in this regime [22]. Note that even modes have a displacement that on average gives no change in capacitance during the oscillation. Because of this, the motion of even modes is not strongly excited by the antenna, nor is their motion strongly detected by the current through the nanotube. From a fit of the frequency responses shown in Figures 5.1b and 5.1c, we extract a quality factor of $Q \sim 15000$ for the first mode and $Q \sim 5000$ for the sec-

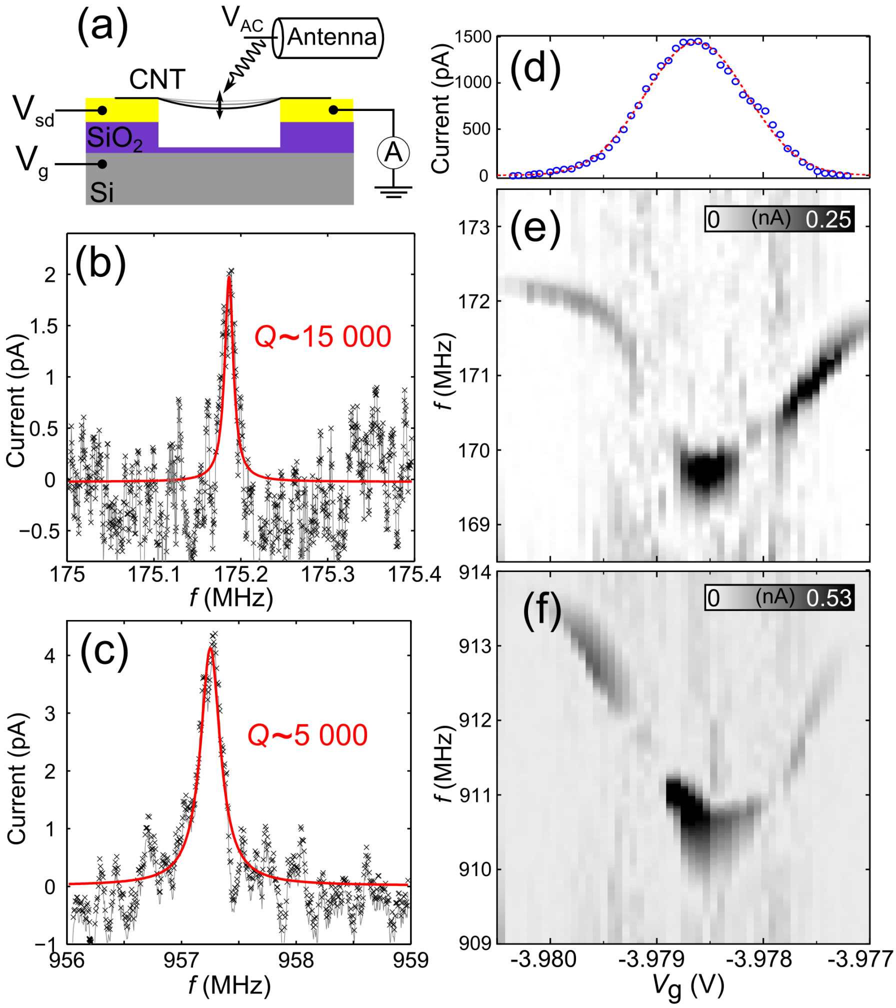

FIGURE 5.1: (a) Schematic diagram of the carbon nanotube device, freely suspended over a trench between drain and source electrodes. The Si substrate is employed as a backgate. (b) and (c) Resonance spectra measured by means of the rectification method at fixed gate voltage and low excitation power for two mechanical eigenmodes of the carbon nanotube. The quality factor is obtained by fitting the measured spectra to the response of a damped driven harmonic oscillator (solid red lines, see Eq. 4.11). (d) DC current through the nanotube versus gate voltage showing single-electron tunneling and Coulomb blockade electronic behaviour. (e) and (f) Color map showing the absolute value of the rectified current through the nanotube as a function of the RF frequency and gate voltage ($V_{sd} = 200\ \mu$V). The tuned mechanical resonance shows up as the gray/black curve with a dip at the Coulomb peak.

ond mode. This quality factor is lower than the highest values reported previously. We attribute the smaller Q-factor to damping from single-electron tunneling, as was reported in earlier devices (see Chs. 3 and 4). In the device studied here, the quantum dot is less strongly tunnel-coupled to the source and drain, preventing us from measuring the mechanical resonance deep in the Coulomb valleys, where the previously reported high quality-factors were measured.

The mechanical origin of the resonance peaks observed in Figure 5.1b and 5.1c is confirmed by studying the gate tunability of the resonance frequencies. This is done by modifying the tension in the nanotube, changing the applied gate voltage, which gives a tuning of 22 MHz/V and 38 MHz/V for the mode A and B respectively (not shown) [10]. Additionally, in the Coulomb blockade regime, the mechanical resonance frequencies experience a dip (down to 3 MHz approx.) when the applied gate voltage is swept across a Coulomb peak (see Figures 5.1e and 5.1f, and also Chs. 3 and 4). This is due to the electrostatic force on the nanotube, which depends on the average charge on the quantum dot. Across a Coulomb peak, the average charge increases monotonically from N to N+1 electrons in a small gate voltage range [23–25]. When the nanotube is closer to the gate, the gate voltage is effectively larger, increasing the average charge on the carbon nanotube and causing a force towards the gate. This anti-restoring force softens the carbon nanotube spring and results in a decrease of the mechanical resonance frequency.

5.2 SINGLE-ELECTRON MODE COUPLING

To excite two mechanical resonances of the nanotube at the same time, the antenna is driven by the combined voltage of two RF signal generators. This allows one to study the interaction between mechanical modes in carbon nanotubes using a multifrequency experimental scheme, sweeping two frequencies at the same time. The frequency of the first signal generator is swept around the resonance frequency of mode A (fast axis sweep). Every time the frequency of the generator matches the resonance frequency of mode A, the DC current through the nanotube experiences a sudden change due to the above described rectification mechanism (see [4] and Ch. 2). After each sweep of the first generator, the frequency of the second generator is incremented and another sweep around the resonance of mode A is carried out with the first generator. This process is repeated until a sweep around the resonance frequency of mode B is accomplished (slow axis sweep). When the frequency of the second RF-generator is off-resonance with mode B, the oscillation amplitude of mode B is negligible and thus there is no appreciable coupling between modes A and B. On the other hand, when the frequency of the second generator approaches the resonance frequency of mode B, the oscillation amplitude of the carbon nanotube in mode B becomes appreciable and the resonance

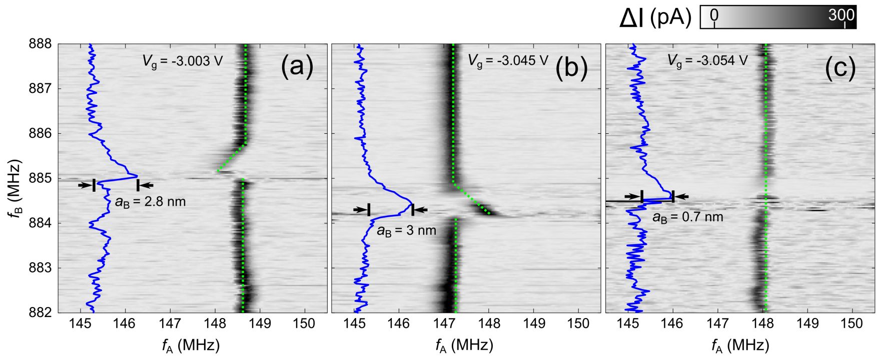

FIGURE 5.2: (color scale) DC rectified current through the nanotube as a function of the RF frequency of the two signal generators connected to the antenna (V_{sd} = 200 μV). When the mechanical resonance of the mode A mode is excited, the current shows a sudden change. The resonance of mode A is marked by a drop in the rectified current (shown in black in the colormaps). (a) The resonance frequency of mode A shifts to lower frequency when the RF signal of the second generator hits the resonance frequency of the mode B ($V_g = -3.003$ V). (b)-(c) Same as (a) but with a V_g value of -3.0045 V and -3.0054 V respectively, showing mode stiffening (b) and negligible coupling (c). The green dotted lines are a guide to the eye. The blue line profiles inserted in (a)-(c) show the oscillation amplitude of the mode B (calculated from the measured change in the DC current through the nanotube using an electrostatic model and assuming that the mode shape resembles that of the third bending mode of a doubly-clamped beam) as a function of the (slowly incremented) frequency of the second generator.

frequency of mode A may be modified by the motion of mode B. Mode B is driven at a much larger RF power (-5 dBm) than mode A (-20 dBm), to limit the backaction exerted by mode A on mode B.

From these measurements, the DC current through the nanotube as a function of the two driving frequencies is obtained. The data can be conveniently represented in a (3-dimensional representation) color map form as shown in Figure 5.2, with a fast axis (frequency sweep around the resonance of mode A) and a slow axis (frequency sweep around the resonance of mode B). In the colorscale data, we have subtracted off the background signal from the mechanical resonance corresponding to the slow sweep direction. This background signal, which contains information about the response of mode B, is shown as a blue line profile overlayed on top of the colorscale data. The blue line profile indicates the horizontal position at which the frequency of the second generator hits the resonance of mode B. These profiles show that the mechanical resonance of mode B presents a clear sharkfin shape, a characteristic of the Duffing-like nonlinear resonance, indicating that mode B vibrates in the nonlinear regime.

Figure 5.2a demonstrates that the resonance frequency of mode A decreases when mode B is driven at resonance. This change in the resonance frequency of mode A, while the oscillation amplitude of mode B increases, indicates the interaction between the two vibration modes of the carbon nanotube. Interestingly, the interaction changes qualitatively when adjusting the gate voltage: when this measurement is repeated for slightly different gate voltages, the effect of this modal interaction is dramatically different. In Figure 5.2a to 5.2c we present three different situations: (a) the modal interaction reduces the resonance frequency of mode A (mode softening), (b) the modal interaction increases the resonance frequency of mode A (mode stiffening) and (c) the effect of the modal interaction is negligible (modal interaction suppression). A similar mode coupling behavior has been observed in two other carbon nanotube devices with slightly different geometries.

The (scaled) equation describing the motion of mode i taking into account the coupling between the modes can be written as:

$$u_i + \eta_i u_i + \omega_i^2 u_i + \sum_{j,k,l} \alpha_{ijkl} u_j u_k u_i = f_i \cos(\omega_d t), \tag{5.1}$$

where η_i denotes the damping, ω_i the resonance frequency and f_i the driving force of mode i, and the indices j, k, l run over the number of modes considered. For a single mode (i = j = k = l), this yields the Duffing equation of a nonlinear resonator. A detailed theoretical investigation can be found in subsection 4.6.2. In a previous work on micromechanical resonators [18], the α terms were shown to be due to displacement-induced tension. For carbon nanotube quantum dots, however, it is established that the nonlinear α terms, responsible of the Duffing nonlinearity, are strongly influenced by the single-electron tunnelling processes in the suspended carbon nanotube (see Ch. 6). This yields interesting phenomena such as the gate tunability of the α terms in carbon nanotubes from positive to negative values in response to a small change in gate voltage.

5.3 GATE-TUNABLE MODE COUPLING

To verify that the observed modal interaction is dominated by single-electron tunneling processes, we have measured the frequency tuning by the modal interactions as a function of the gate voltage. Figure 5.3a shows the maximum change in the resonance frequency of mode A (due to the interaction with mode B) at different gate voltages across a Coulomb peak, showing a continuous transition from stiffening to softening behaviour. The observed change in sign of the modal interaction (i.e. stiffening vs. softening behavior) is directly related to the sign of the nonlinear spring constant α of the carbon nanotube, which can be obtained from the curvature of the f_A vs V_g trace ($\partial^2 f_A / \partial V_g^2$) shown in Figure 5.3b (see Ch. 6), indicating that the mechanism behind this gate dependence is the time-varying

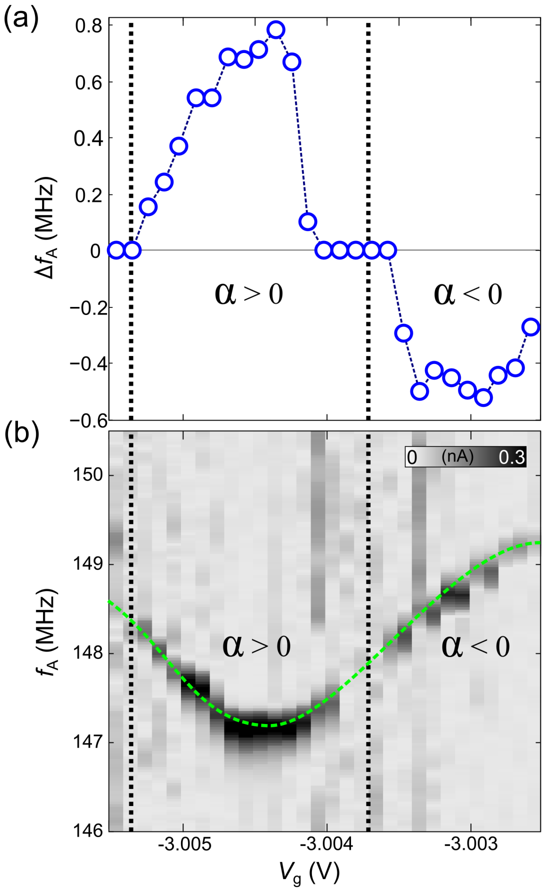

FIGURE 5.3: (a) maximum change in the resonance frequency of the mode A as a function of the gate voltage. The resonance frequency of mode A increases with gate voltages when the nonlinear spring constant is positive (i.e. for the gate voltages at which Coulomb peaks occur). On the other hand, the resonance frequency of mode A decreases for the gate voltages when the nonlinear spring constant is negative. (b) frequency dip of mode A when the gate voltage is swept across a Coulomb peak. The sign of the nonlinear spring constant α can be determined by the sign of the curvature of the frequency vs. gate voltage trace.

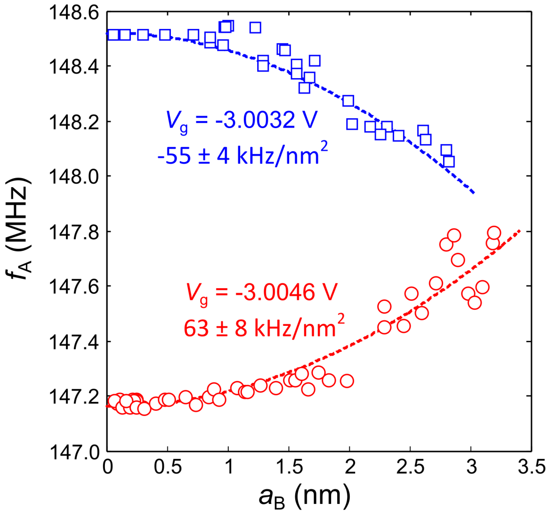

FIGURE 5.4: Resonance frequency shift of the mode A as a function of the oscillation amplitude of the mode B for two different gate voltages, showing softening (blue squares) and stiffening (red circles) behaviour. The modal coupling strength can be determined from the quadratic dependence of the frequency shift with the oscillation amplitude (dashed lines).

electrostatic force induced by the charge fluctuation in the quantum dot formed by the suspended carbon nanotube.

Figure 5.4 shows the resonance frequency of mode A as a function of the oscillation amplitude of mode B. The resonance frequency shift shows a quadratic dependence with the oscillation amplitude of mode B, similar to the one observed in Ref. [18] for a micromechanical resonator. The modal interaction strength is given by the change in the resonance frequency as a function of the oscillation amplitude of mode B squared. The oscillation amplitude has been calculated from the measured change in the DC current through the nanotube using an electrostatic model and assuming that the mode shape resembles that of the third bending mode of a doubly-clamped beam. We find that the modal interaction strength can continuously be tuned from 63 ± 8 kHz/nm^2 (stiffening) to -55 ± 4 kHz/nm^2 (softening). This modal interaction is not only highly tunable, with a fairly low change in the gate voltage, but it is also remarkably strong: six orders of magnitude larger that the coupling strength measured in micromechanical resonators (about 0.025 Hz/nm^2) [18].

5.4 OUTLOOK AND CONCLUSIONS

An interesting consequence of the strong mode coupling observed in suspended carbon nanotubes in the Coulomb blockade regime is that it could potentially provide an ultimate limit to the linewidth of the frequency response, and therefore also the quality factor of the resonator. At finite temperature, for example, the thermal motion of one mode will result in spectral broadening of the other mode. The third bending mode of the carbon nanotube device presented here at a temperature of 4.2 K would exhibit a Brownian motion of 50 pm, leading to a broadening of the mechanical linewidth of the fundamental mode of 170 Hz. Thus, the mode coupling observed here would limit the quality factor to a maximum value of 106, although this maximum quality factor could be even lower if the interaction with other modes is taken into account. Such a spectral broadening is present even at zero temperature due to the zero point fluctuations: the expected zero point motion of 14 pm for the third eigenmode would yield a dispersive coupling of 12 Hz , and places a limit on the quality factor of $1.5\cdot 10^7$. The observed quality factors in this device, however, are lower than these theoretical limits.

From a different point of view, the mode coupling observed here can be thought of as a nonlinear coupling between two phonon cavities. In this case, the spectral broadening of 12 Hz calculated above using the zero-point fluctuations of the third mode would represent the strength of the dispersive coupling g between the two cavities in their ground state. For our device, the coupling rate is smaller than the decoherence rates of the modes ($\Gamma_{A,B} = f_{A,B}/Q_{A.B} \approx 10 - 200$ kHz), placing the present experiment in the weak coupling limit. The strong coupling limit ($g > \Gamma_{A,B}$) could potentially be reached in devices with larger Q factors and sharper Coulomb peaks.

In conclusion, we have studied the nonlinear interaction between two different eigenmodes in freely suspended carbon nanotube resonators. In the Coulomb blockade regime, the mode coupling in suspended carbon nanotubes is dominated by single-electron-tunneling processes. In contrast to purely mechanical mode coupling, in this regime both the strength and the sign of the coupling can be tuned by changing an external gate voltage. The modal interaction strength in carbon nanotubes is remarkably strong, about six orders of magnitude larger than that of previously studied micromechanical resonators.

ACKNOWLEDGMENT This work was supported by FOM and the European Union (FP7) through the programs QNEMS and RODIN.

REFERENCES

[1] A. Castellanos-Gomez, H. B. Meerwaldt, W. J. Venstra, H. S. J. van der Zant, and G. A. Steele, *Strong and tunable mode coupling in carbon nanotube reso-*

nators, Physical Review B **86**, 041402 (2012).

[2] A. M. Fennimore, T. D. Yuzvinsky, W. Q. Han, M. S. Fuhrer, J. Cumings, and A. Zettl, *Rotational actuators based on carbon nanotubes*, Nature **424**, 408 (2003).

[3] P. Poncharal, Z. L. Wang, D. Ugarte, and W. A. de Heer, *Electrostatic deflections and electromechanical resonances of carbon nanotubes*, Science **283**, 1513 (1999).

[4] A. K. Hüttel, G. A. Steele, B. Witkamp, M. Poot, L. P. Kouwenhoven, and H. S. J. van der Zant, *Carbon Nanotubes as Ultrahigh Quality Factor Mechanical Resonators*, Nano Letters **9**, 2547 (2009).

[5] E. A. Laird, F. Pei, W. Tang, G. A. Steele, and L. P. Kouwenhoven, *A High Quality Factor Carbon Nanotube Mechanical Resonator at 39 GHz*, Nano Letters **12**, 193 (2011).

[6] J. Chaste, M. Sledzinska, M. Zdrojek, J. Moser, and A. Bachtold, *High-frequency nanotube mechanical resonators*, Applied Physics Letters **99**, 213502 (2011).

[7] J. Chaste, A. Eichler, J. Moser, G. Ceballos, R. Rurali, and A. Bachtold, *A nanomechanical mass sensor with yoctogram resolution*, Nature Nanotechnology **7**, 301 (2012).

[8] H.-Y. Chiu, P. Hung, H. W. C. Postma, and M. Bockrath, *Atomic-Scale Mass Sensing Using Carbon Nanotube Resonators*, Nano Letters **8**, 4342 (2008).

[9] K. Jensen, K. Kim, and A. Zettl, *An atomic-resolution nanomechanical mass sensor*, Nature Nanotechnology **3**, 533 (2008).

[10] V. Sazonova, Y. Yaish, H. Ustunel, D. Roundy, T. A. Arias, and P. L. McEuen, *A tunable carbon nanotube electromechanical oscillator*, Nature **431**, 284 (2004).

[11] H. W. C. Postma, I. Kozinsky, A. Husain, and M. L. Roukes, *Dynamic range of nanotube- and nanowire-based electromechanical systems*, Applied Physics Letters **86**, 223105 (2005).

[12] B. Lassagne, Y. Tarakanov, J. Kinaret, D. Garcia-Sanchez, and A. Bachtold, *Coupling Mechanics to Charge Transport in Carbon Nanotube Mechanical Resonators*, Science **325**, 1107 (2009).

[13] W. J. Venstra, H. J. R. Westra, and H. S. J. van der Zant, *Q-factor control of a microcantilever by mechanical sideband excitation*, Applied Physics Letters **99**, 151904 (2011).

[14] T. Faust, J. Rieger, M. J. Seitner, P. Krenn, J. P. Kotthaus, and E. M. Weig, *Nonadiabatic Dynamics of Two Strongly Coupled Nanomechanical Resonator Modes*, Physical Review Letters **109**, 37205 (2012).

[15] K. J. Lulla, R. B. Cousins, A. Venkatesan, M. J. Patton, A. C. Armour, C. J. Mellor, and J. R. Owers-Bradley, *Nonlinear modal coupling in a high-stress doubly-clamped nanomechanical resonator* (2012), URL `http://arxiv.org/abs/1204.4487`.

[16] I. Mahboob, K. Nishiguchi, H. Okamoto, and H. Yamaguchi, *Phonon-cavity electromechanics*, Nature Physics **8**, 387 (2012).

[17] H. J. R. Westra, D. M. Karabacak, S. H. Brongersma, M. Crego-Calama, H. S. J. Van der Zant, and W. J. Venstra, *Interactions between directly-and parametrically-driven vibration modes in a micromechanical resonator*, Physical Review B **84**, 134305 (2011).

[18] H. J. R. Westra, M. Poot, H. S. J. van der Zant, and W. J. Venstra, *Nonlinear modal interactions in clamped-clamped mechanical resonators.*, Physical Review Letters **105**, 117205 (2010).

[19] D. H. Santamore, A. C. Doherty, and M. C. Cross, *Quantum nondemolition measurement of fock states of mesoscopic mechanical oscillators*, Physical Review B **70**, 144301 (2004).

[20] S. Kumar and D. P. DiVincenzo, *Exploiting Kerr cross nonlinearity in circuit quantum electrodynamics for nondemolition measurements*, Physical Review B **82**, 014512 (2010).

[21] A. W. Barnard, V. Sazonova, A. M. van der Zande, and P. L. McEuen, *Fluctuation broadening in carbon nanotube resonators*, Proceedings of the National Academy of Sciences **109**, 19093 (2012).

[22] D. Garcia-Sanchez, A. S. Paulo, M. J. Esplandiu, F. Perez-Murano, L. Forro, A. Aguasca, and A. Bachtold, *Mechanical detection of carbon nanotube resonator vibrations*, Physical Review Letters **99**, 085501 (2007).

[23] A. Naik, O. Buu, M. D. LaHaye, A. D. Armour, A. A. Clerk, M. P. Blencowe, and K. C. Schwab, *Cooling a nanomechanical resonator with quantum back-action*, Nature **443**, 193 (2006).

[24] A. D. Armour, M. P. Blencowe, and Y. Zhang, *Classical dynamics of a nanomechanical resonator coupled to a single-electron transistor*, Physical Review B **69**, 125313 (2004).

[25] M. Poot and H. S. J. van der Zant, *Mechanical systems in the quantum regime*, Physics Reports-Review Section of Physics Letters **511**, 273 (2012).

6

CARBON NANOTUBES: NONLINEAR HIGH-Q RESONATORS WITH STRONG COUPLING TO SINGLE-ELECTRON TUNNELING

Carbon nanotubes (CNTs) are nonlinear high-Q resonators with strong coupling to single-electron tunneling. We discuss four different contributions to the nonlinear oscillation of a CNT resonator: beam-like mechanical nonlinearity, nonlinearity due to gate-induced mechanical tension, electrostatic nonlinearity, and nonlinearity due to single-electron tunneling, and provide quantitative estimates of their strengths. Finally, we show how the large response of the resonance frequency of a CNT resonator to a change in gate voltage or tension makes CNT resonators ideally suited for parametric excitation and for studying the coupling between different mechanical modes.

Parts of this Chapter have been published in "Fluctuating nonlinear oscillators" (Oxford University Press, 2012), ed. Mark Dykman [1].

6.1 CARBON NANOTUBE RESONATORS IN THE NONLINEAR REGIME

Hooke's Law states that, when an elastic object is brought out of its equilibrium position, the restoring force is linearly dependent on the displacement. As the applied force and resulting displacement increase, Hooke's Law is no longer valid and nonlinear effects become important. The first correction to Hooke's Law is made by adding a restoring force term that is quadratic in displacement. The quadratic term leads to a renormalization of the cubic term [2]. In many cases, this renormalization is a small effect, and hence we have neglected it in this analysis (see also subsection 4.6.1). In this section we focus on the next term of the restoring force, which is cubic in displacement. The cubic term is called the Duffing term, and the resulting equation of motion the Duffing equation (see also [2]). The restoring force is now given by $F_r = -k_0 u - m\alpha u^3$, were α is the nonlinearity or Duffing parameter with units of $\mathrm{N/(kg\,m^3)}$. The nonlinearity can also be seen as a correction to the spring constant. Writing the restoring force as $F_r = -ku = -(k_0 + m\alpha u^2)u$, the nonlinearity parameter is given by:

$$\alpha = \frac{1}{2m}\frac{d^2k}{du^2}. \tag{6.1}$$

When α is positive, the Duffing term causes, as drive force is increased, the resonance peak to tilt towards higher frequencies, resulting in a stiffening-spring behaviour. Conversely, when α is negative and the resonance peak tilts towards lower frequencies, it results in a softening-spring behaviour. As the applied force is increased further, the tilting of the peak causes bistability: for one drive frequency there are two metastable states of oscillation, one with a low amplitude and the other with a high amplitude of oscillation [3].

In this section, we first describe how the measured lineshape changes as the drive power is increased and at what power the lineshape becomes nonlinear. Next, we describe three causes for nonlinearity in CNT mechanical resonators: geometric nonlinearity caused by mechanical tension, electrostatic nonlinearity, and nonlinearity due to single-electron tunneling. We calculate the corresponding α values for the example CNT described in Table 6.2 in the appendix to this Chapter.

6.1.1 NONLINEAR RESPONSE OF CARBON NANOTUBE RESONATORS

Figure 6.1 shows a measurement of the lineshape of a 600 nm long CNT resonator detected by using the rectification technique (see subsection 2.1.2). At a low power of -43 dBm, the CNT is driven to oscillate at a small amplitude and the noise is too high to observe the motion. As the drive power is increased to -40 dBm, a Lorentzian lineshape appears in the current when the drive frequency is near the mechanical resonance frequency of the CNT. At this drive power, the restoring force is given by Hooke's Law and can be approximated to be linear with displacement. When the drive power is increased further to -38 dBm, the restoring force is nonlinear with respect to displacement but the amplitude is still single-valued, resulting in a sharkfin-like appearance of the lineshape. At a higher power of -35 dBm in Figure 6.1, bistability and hysteresis occur. Bistability appears as for certain frequencies there is both a low- and a high-amplitude state in which the resonator can oscillate. The amplitude of the motion depends on the direction in which the drive frequency is changed, displaying a hysteretic behaviour when the drive frequency is swept from high to low, or from low to high. The bottom two panels of Figure 6.1 show nonlinearity in the form of a Duffing sharkfin-like lineshape. The sharkfin lineshape points towards higher frequency, indicating a stiffening spring behaviour.

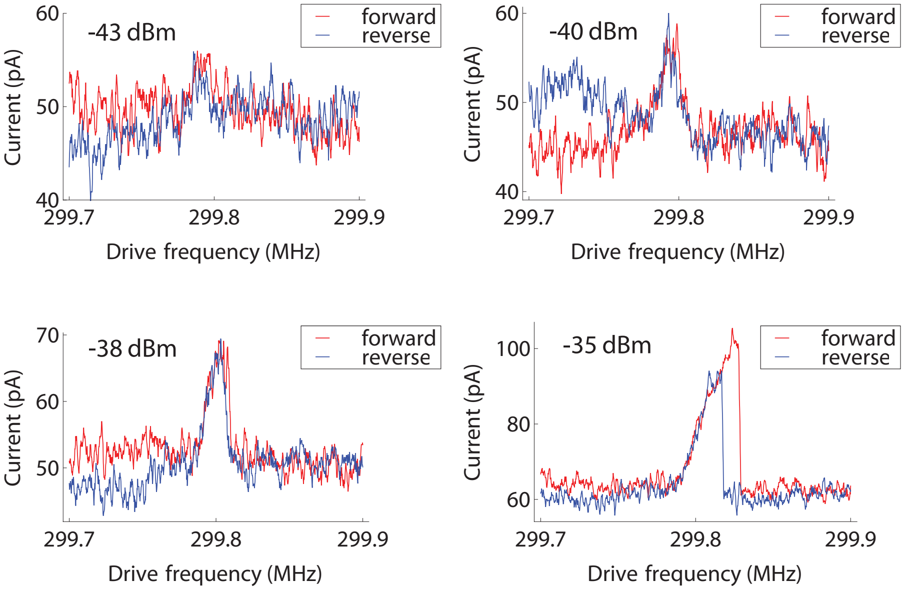

FIGURE 6.1: Frequency responses of the rectified current (see subsection 2.1.2) showing the mechanical signal drowned in noise (-43 dBm), a linear response with a Lorentzian lineshape (-40 dBm), the onset of nonlinearity (-38 dBm), and nonlinearity with bistability and hysteresis (-35 dBm), of a CNT across a 600 nm wide trench, 285 nm above a gate, measured at 20 mK.

In many applications [4, 5], the range of powers over which the mechanical resonance displays a detectable linear response is an important parameter. This range of powers is often referred to as the “dynamic range” of the mechanical oscillator. The smallest useful drive power is the one for which the measured signal matches the measured noise, and the largest useful drive power is the one at the onset of nonlinearity.

To estimate an upper bound for the dynamic range, we follow the analysis of [6] and only consider the thermomechanical contribution to the noise, leaving out other intrinsic and extrinsic sources of noise. The spectral density of displacement noise at the resonance frequency is:

$$S_u = \frac{4k_b T Q}{m\omega_0^3}, \tag{6.2}$$

where k_b is Boltzmann’s constant, T is temperature of the resonator, Q is the quality factor, m is the total mass of the resonator, and ω_0 is the resonance frequency. For the example CNT in Table 6.2 this gives a displacement noise of $\sqrt{S_u} = 0.15\ \mathrm{pm}/\sqrt{\mathrm{Hz}}$. The root-mean-square amplitude of oscillation at which nonlinearity sets in, $\mathscr{A}_c$, is the amplitude at the lowest drive power at which an infinitesimal change in frequency results in an infinite change in amplitude. The analysis of nonlinear response curves and the onset of nonlinearity can be found in [7]. According to [8] the critical amplitude, which is not at the resonance frequency, is given by:

$$\mathscr{A}_c = \frac{2\cdot 0.83}{3}\omega_0\sqrt{\frac{2\sqrt{3}}{\alpha Q}}, \tag{6.3}$$

where α is the nonlinearity parameter which will be discussed in the next section.

The dynamic range is defined as the ratio of the 1 dB compression point to the noise amplitude at the resonance frequency:

$$\begin{aligned} DR(\mathrm{dB}) &= 20\log\left(\frac{0.745\mathscr{A}_c}{\sqrt{S_u\Delta f}}\right) \\ &= 20\log\left(\frac{0.745\cdot 0.83\,\omega_0^2}{3Q}\sqrt{\frac{2\sqrt{3}m\omega_0}{k_b T\alpha\Delta f}}\right), \end{aligned} \tag{6.4}$$

where Δf is the measurement bandwidth. The 1 dB compression point occurs when the peak amplitude is 1 dB lower than what would be expected for a purely linearly response and has a value of $0.745\mathscr{A}_c$. Eq. 6.4 shows that the low mass and the high nonlinearity parameter for CNT resonators give rise to a small dynamic range compared to top-down fabricated nanomechanical resonators.

6.1.2 GEOMETRIC NONLINEARITY

In this subsection, it is described how geometric nonlinearities in the motion of CNT resonators arise. When the amplitude of oscillation becomes larger, the CNT experiences significantly more tension at the extremal points of oscillation than at the equilibrium position. This tension thus depends on displacement and is one contribution to the geometric nonlinearity. Furthermore, the force induced by the gate voltage causes tension in the CNT, which again depends on displacement, being another contribution to the geometric nonlinearity.

To derive the expressions describing geometric nonlinearity we start with the theoretical framework for a driven damped beam [9]. The Euler-Bernoulli beam theory describes the motion of continuous bodies subjected to external forces. Even though the diameter of a CNT consists of only around 10 atoms, continuum mechanics is nonetheless a good description of the mechanical properties of a CNT resonator [10]. We take the coordinate system as shown in Figure 6.2: The CNT axis is positioned in the z-direction and the oscillation takes (at least for now) place in the x-direction.

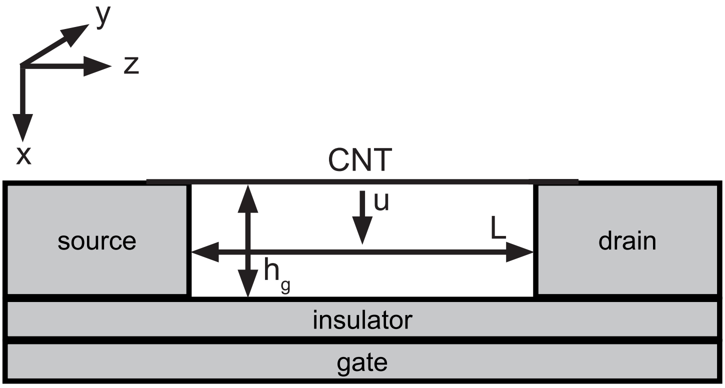

FIGURE 6.2: Coordinate axes: the CNT resonator of length L is suspended between the source and drain electrodes at a distance of h_g above the gate. The CNT is aligned in the z-direction. The displacement u takes place in the x-direction.

The displacement u of the CNT resonator as a function of time is governed by the following equation of motion:

$$\rho A \frac{\partial^2 u}{\partial t^2} + \eta \frac{\partial u}{\partial t} + D \frac{\partial^4 u}{\partial z^4} - T \frac{\partial^2 u}{\partial z^2} = f. \tag{6.5}$$

The first term describes inertia, with ρ being the density and A the area of the cross section. The second term describes damping with $\eta = \rho A \omega_0 / Q$ the damping rate per unit of length. The third term is the restoring force due to the bending rigidity $D = EI/(1-\nu^2)$, with $E = 1.3$ TPa [11] and $\nu = 0.2$ [12] the Young's modulus and Poisson's ratio respectively, and the second (bending) moment of inertia I. The CNT's Poisson's ratio is neglected and the denominator is set to unity. We approximate the CNT resonator as a solid cylinder with a second moment of inertia $I = \pi r^4/4$. The fourth term describes the restoring force due to the tension T and f describes an external force per unit length.

There are four boundary conditions determining the modeshapes $u(z)$. The CNT is doubly clamped, leading to $u(0) = 0$ and $u(L) = 0$. Furthermore, the bending rigidity of the CNT prescribes the slope of the CNT to be continuous at the clamping points, as the CNT goes from lying on the contact to being suspended, resulting in $\partial u/\partial z(0) = 0$ and $\partial u/\partial z(L) = 0$.

To solve Eq. 6.5, we first separate all contributions into a static/dc and a dynamic/ac component. For the position-dependent displacement of the CNT, $u(z)$, and for the gate voltage, $V_g(z)$, this gives:

$$u(z) = u_{dc}(z) + u_{ac}(z)\cos(\omega_d t), \tag{6.6}$$

$$V_g(z) = V_g^{dc}(z) + V_g^{ac}(z)\cos(\omega_d t). \tag{6.7}$$

The tension felt by the CNT is then given by:

$$\begin{aligned} T(z) &= T_0 + \frac{EA}{2L}\int_0^L \left(\frac{\partial u}{\partial z}\right)^2 dz \\ &= T_0 + \frac{EA}{2L}\int_0^L \left(\frac{\partial u_{dc}}{\partial z}\right)^2 dz + \frac{EA}{L}\left(\int_0^L \frac{\partial u_{dc}}{\partial z}\frac{\partial u_{ac}}{\partial z} dz\right)\cos(\omega_d t) \\ &= T_{dc} + T_{ac}\cos(\omega_d t), \end{aligned} \tag{6.8}$$

with T_0 the residual tension present at zero gate voltage. The uniform force per unit length on the CNT due to the gate voltage is:

$$\begin{aligned} f(z) &= \frac{1}{2}\frac{dc_g}{du}V_g^2 \\ &= \frac{1}{2}\frac{dc_g}{du}(V_g^{dc})^2 + \frac{dc_g}{du}V_g^{dc}V_g^{ac}\cos(\omega_d t) \\ &= f_{dc}(z) + f_{ac}(z)\cos(\omega_d t). \end{aligned} \tag{6.9}$$

Here dc_g/du is the derivative of the capacitance per unit length with respect to displacement (see Eq. 1.18). We arrive at two equations; one for the static and one for the dynamic displacement:

$$D\frac{\partial^4 u_{dc}}{\partial z^4} - T_{dc}\frac{\partial^2 u_{dc}}{\partial z^2} = f_{dc}, \tag{6.10}$$

$$-\omega_d^2 \rho A u_{ac} + i\omega_d \eta u_{ac} + D\frac{\partial^4 u_{ac}}{\partial z^4} - T_{dc}\frac{\partial^2 u_{ac}}{\partial z^2} - T_{ac}\frac{\partial^2 u_{dc}}{\partial z^2} = f_{ac}. \tag{6.11}$$

It is useful to introduce scaled variables denoted with primes:

$$\begin{array}{lll} u'_{dc,ac} = \frac{u_{dc,ac}}{r}, & z' = \frac{z}{L}, & T'_{dc,ac} = \frac{T_{dc,ac}L^2}{D}, \\ L'_{dc,ac} = \frac{L_{dc,ac}}{r} = \frac{L^4 f_{dc,ac}}{Dr}, & t' = t\Omega, & \omega' = \frac{\omega}{\Omega}, \\ \eta' = \frac{\eta L^4 \Omega}{D}, & \Omega = \frac{1}{L^2}\sqrt{\frac{D}{\rho A}}. & \end{array} \tag{6.12}$$

The equation for the dynamic displacement now becomes:

$$-\omega_d'^2 u'_{ac} + i\omega'_d \eta' u'_{ac} + D\frac{\partial^4 u'_{ac}}{\partial z'^4} - T'_{dc}\frac{\partial^2 u'_{ac}}{\partial z'^2} - T'_{ac}\frac{\partial^2 u'_{dc}}{\partial z'^2} = L'_{ac}. \tag{6.13}$$

The ac displacement is separated into an amplitude $\mathscr{A}(t)$ changing slowly with respect to the oscillation, and a spatial part $\xi(z)$:

$$u_{ac}(z,t) = \mathscr{A}_n(t)\xi_n(z), \tag{6.14}$$

where the subscript n denotes the mode of oscillation. The eigenfunctions of the spatial part of Eq. 6.13 give the modeshapes:

$$\mathscr{L}\xi_n(z') = \left(D\frac{\partial^4}{\partial z'^4} - T'_{dc}\frac{\partial^2}{\partial z'^2}\right)\xi_n - T'_{ac}[\xi_n]\frac{\partial^2 u'_{dc}}{\partial z'^2} = \omega_n'^2(T'_{dc}, u'_{dc})\cdot\xi_n(z'), \tag{6.15}$$

where the eigenfrequencies are given by:

$$\omega'_n = \beta_n^2\sqrt{1 + \frac{T'_{dc}}{\beta_n^2}}, \tag{6.16}$$

with β_n a numerical factor. The first four β_n are found to be 4.73004, 7.8532, 10.9956, and 14.1372. Like a guitar string, the resonance frequency of the CNT increases with increased tension. Also, as tension is increased the resonance frequencies converge towards a harmonic spectrum.

In order to make the amplitude $\mathscr{A}_n(t)$ of the symmetric, odd modes correspond to the root-mean-square displacement over the length of the CNT (not in time) as:

$$\mathscr{A}_n(t) = \sqrt{\frac{\int_0^L u_{ac}^2 dz}{L}}, \tag{6.17}$$

the eigenfunctions $\xi_n(x')$ have the following orthonormalization:

$$\int_0^1 \xi_m(z')\xi_n(z')dz' = \delta_{mn}. \tag{6.18}$$

Inserting expression 6.17 into Eq. 6.13, multiplying by $\xi_n(z')$, integrating over the length, and unscaling gives:

$$\left(\omega_n^2 - \omega_d^2 + i\frac{\omega_d\omega_n}{Q}\right)\mathscr{A}_n = \frac{f_{ac}}{\rho A}a_n, \tag{6.19}$$

where $a_n = \int_0^1 \xi_n(z')dz'$. The first four a_n are: 0.83, 0, 0.36, 0. In the ideal case, even modes have a displacement that on average gives no change in capacitance and are therefore often not visible in experiments.

Up to this point, a linear system was described. We now introduce nonlinearity, looking at two different contributions to the geometric nonlinearity of a CNT resonator. For the first contribution, the CNT is described as a beam [13, 14], with no dc displacement or tension $u_{dc}, T_{dc} = 0$. For the second contribution, the two regimes from [15], i.e. the weak-bending regime and the strong-bending regime, are used to account for the dc displacement a CNT possesses and the tension it acquires from applying a gate voltage.

Modeling the CNT as a beam, we see that when the amplitude of oscillation becomes larger, it is significantly longer at the extremal points of oscillation than at its equilibrium position. A segment that used to be of length $dL = dz$ now has a length of $dL = \sqrt{dz^2 + du^2} \approx dz + \frac{1}{2}(\frac{\partial u}{\partial z})^2 dz$. The CNT becomes longer by an amount ΔL and this causes a change in tension of $EA\Delta L/L$. The associated added tension T'^*_{ac} is:

$$\begin{aligned} T'^*_{ac} &= 2\int_0^1 \left(\frac{\partial u'_{ac}}{\partial z'}\right)^2 dz' \\ &= 2\frac{\mathscr{A}_n^2}{r^2}b_n, \end{aligned} \tag{6.20}$$

where $b_n = \int_0^1 (\frac{\partial \xi_n(z')}{\partial z'})^2 dz'$, with the first four b_n calculated to be 12.3, 46.1, 98.9, and 171.6. The scaled restoring force per unit length due to the tension T'^*_{ac} is given by:

$$-f'^*_r = -T'^*_{ac}\frac{\partial^2 u'_{ac}}{\partial z'^2}, \tag{6.21}$$

which we add to Eq. 6.13. Multiplying the augmented equation by $\xi_n(z')$, integrating over the length and unscaling, yields the well-known Duffing equation:

$$\frac{\partial^2 \mathscr{A}_n}{\partial t^2} + \frac{\omega_n}{Q}\frac{\partial \mathscr{A}_n}{\partial t} + \omega_n^2\mathscr{A}_n + \alpha_{beam}c_n\mathscr{A}_n^3 = \frac{f_{ac}}{\rho A}a_n, \tag{6.22}$$

with

$$\alpha_{beam} = \frac{b_n^2 E}{2L^4 \rho c_n}. \tag{6.23}$$

Here the identity $\int_0^1 \frac{\partial^2 \xi_n}{\partial z^2} \xi_n dz = -\int_0^1 (\frac{\partial \xi_n}{\partial z})^2 dz = -b_n$ is used. The factor $c_n = \int_0^1 \xi_n(z')^4 dz'$ arises from our definition of α: if the analysis had been started not with the unscaled version of Eq. 6.21 but with $f_r L = -m\alpha_{beam} u^3$ the Duffing term would have become $\alpha_{beam} \left(\int_0^1 \xi_n(z')^4 dz' \right) u^3$. The first four c_n values are 1.85, 1.69, 1.64, and 1.61.From Eq. 6.23, it is clear that, if the CNT resonator is modeled as a beam, the nonlinearity is positive and thus always gives a stiffening spring behaviour. For our example CNT in Table 6.2, it results in a nonlinearity for the fundamental mode of $9.6 \cdot 10^{34}$ N/(kg m^3).

Until now, we have assumed that the CNT acts as a beam with no static displacement and no static tension. In CNT devices, these assumptions are often not valid: by applying a dc voltage to a nearby gate, the CNT can acquire significant static displacements that can be larger than the CNT diameter. As described in [15], with no initial tension, there are two regimes describing the bending of the CNT: the weak-bending and the strong-bending regime. In the weak-bending regime, the CNT acts as a beam at low gate voltages, and both α_{beam} and α_{weak} contribute to the geometric nonlinearity. It undergoes a transition to string-like behaviour at larger gate voltages as the CNT becomes strongly bent by the force from the gate. The crossover from the weak-bending to the strong-bending regime occurs when the restoring force due to tension is equal to the restoring force due to bending rigidity, $T_{dc} = EI/L^2$, or equivalently, when the CNT displaces by a distance equal to its radius. At this point, the contribution α_{beam} to the geometric nonlinearity, arising from the tension induced by the oscillation of the CNT, can no longer be described by Eq. 6.23. This is because, at non-zero dc deflection in the strong-bending regime, the oscillation of the CNT does not lead to increased tension when moving away from the gate. The gate voltage V_g^* at which the crossover from the weak-bending regime to the strong-bending regime occurs is found from $l'_{dc} \approx 871$ and for the example CNT in Table 6.2 has a value of $V_g^* = 2.1$V.

At low gate voltages, the CNT is in the weak-bending regime with $T_{dc} \ll EI/L^2$. In this range of gate voltages, the restoring force is dominated by the bending rigidity, leading to mechanical modes with resonance frequencies at ratios close to that of an ideal beam. Starting from a straight CNT (i.e. no dc deflection at zero gate voltage), the tension induced by the gate is [15]:

$$T_{dc}^{weak} = \frac{L^4 A}{60480 EI^2} F_{dc}^2, \tag{6.24}$$

and the mechanical resonance frequency of the lowest mode is given by:

$$\begin{aligned}\omega_0^{weak} &= \sqrt{\frac{EI}{\rho A}\frac{\beta_0^2}{L^2} + 0.28\frac{T}{\sqrt{\rho AEI}}} \\ &= \sqrt{\frac{EI}{\rho A}\frac{\beta_0^2}{L^2} + 0.07\frac{L^4 A}{60480 EI^2\sqrt{\rho AEI}}\left(\frac{dC_g}{du}\right)^2 V_g^4}. \end{aligned} \tag{6.25}$$

For a CNT that begins with no deflection, the resonance frequency at low gate voltage in this beam-like, weak-bending regime scales with $\omega_0 \propto V_g^4$. Note that this quartic gate voltage dependence arises due to the fact that the electrostatic force from the gate is perpendicular to the axis of the CNT, and therefore does not begin to add tension until the CNT develops a static displacement. If the CNT already has a static displacement at zero gate voltage, due, for example, to buckling from compressive strain, or from a downwards curvature of the substrate at the edge of the trench, then the resonance frequency in the weak-bending regime shows a $\omega_0 \propto V_g^2$ gate dependence. From expression 6.25 for the resonance frequency, we obtain the gate voltage dependent spring constant:

$$k_{weak} = \frac{EI}{\rho A}\frac{\beta_0^4}{L^4} + 0.14\frac{L^3 A\beta_0^2}{60480 EI^2}\left(\frac{dC_g}{du}\right)^2 V_g^4. \tag{6.26}$$

We obtain the Duffing nonlinearity parameter by taking the second derivative of Eq. 6.26 with respect to displacement. We do this by using the fact that the displacement of the CNT resonator leads to a change in capacitance to the gate. This in turn is interpreted as an effective change in the gate voltage, since only the gate-induced charge $q_c = C_g V_g$ is relevant.

$$\begin{aligned}\alpha_{weak} &= \frac{1}{2m}\frac{d^2k}{du^2} = \frac{1}{2m}\left(\frac{V_g}{C_g}\frac{dC_g}{du}\right)^2 \frac{d^2k}{dV_g^2} \\ &= 0.84\frac{L^2\beta_0^2}{60480 EI^2 C_g^2\rho}\left(\frac{dC_g}{du}\right)^4 V_g^4. \end{aligned} \tag{6.27}$$

For the example CNT in Table 6.2, this results in a nonlinearity of $8.7\cdot10^{28}\cdot(V_g \text{ in Volt})^4$ N/(kg m^3). Note that this gate-induced contribution to the nonlinearity in the weak-bending regime is much smaller than the contribution from the intrinsic gate-voltage independent beam nonlinearity (Eq. 6.23), and thus the nonlinearity in the weak-bending regime is dominated by that described in Eq. 6.23.

As the gate voltage is increased further, the CNT enters the strong-bending regime, in which its static displacement exceeds its diameter, and the restoring force from the induced tension exceeds the bending rigidity. In this regime, the mechanical modes begin to behave as those of a string under tension, approaching a harmonic spectrum at large gate voltages. In this regime, the gate induced tension is given by [15]:

$$T_{dc}^{strong} = \left(\frac{EA}{24}\right)^{\frac{1}{3}} F_{dc}^{\frac{2}{3}}, \tag{6.28}$$

with a resonance frequency for the lowest mode given by:

$$\omega_0^{strong} = \frac{\pi}{L}\sqrt{\frac{T_{dc}^{strong}}{\rho A}} = \frac{\pi}{L\sqrt{\rho A}}\left(\sqrt{\frac{EA}{96}}\frac{dC_g}{du}\right)^{\frac{1}{3}} V_g^{\frac{2}{3}}. \tag{6.29}$$

In this strong-bending regime, the resonance frequency scales as $\omega_0 \propto V_g^{\frac{2}{3}}$. The gate voltage dependent spring constant is given by:

$$k_{strong} = \frac{\pi^2}{L}\left(\frac{EA}{96}\right)^{\frac{1}{3}}\left(\frac{dC_g}{du}\right)^{\frac{2}{3}} V_g^{\frac{4}{3}}, \tag{6.30}$$

and we obtain the following for the Duffing nonlinearity parameter:

$$\alpha_{strong} = \frac{2\pi^2}{9mLC_g^2}\left(\frac{dC_g}{du}\right)^{\frac{8}{3}}\left(\frac{EA}{96}\right)^{\frac{1}{3}} V_g^{\frac{4}{3}}. \tag{6.31}$$

For the example CNT in Table 6.2, this results in a nonlinearity of $1.9 \cdot 10^{28} \cdot (V_g \text{ in Volt})^{\frac{4}{3}}$ N/(kg m^3).

Until now, we have assumed that the CNT includes no initial tension, i.e. that its relaxed length is the same as the length of the trench. For positive initial tension, corresponding to a tensile stress, the CNT behaves already as a string at zero gate voltage, and shows a flat resonance frequency vs gate response. This flat gate response of the resonance frequency continues until the gate induced tension exceeds this initial tension and begins to tune the resonance frequency, as shown in Figure 6.3.

If the CNT relaxed length is longer than the distance across the trench, the CNT experiences a compressive force. For compressive forces below the Euler instability, this results in a reduction of the resonance frequency at low gate voltages. As the compressive force approaches the Euler instability, the resonance frequency at zero gate voltage vanishes, as shown in Figure 6.3. For compressive forces beyond the Euler instability, the CNT buckles and acquires a non-zero static displacement even at zero gate voltage. Beyond the buckling point, the resonance frequency becomes finite again, and the CNT exhibits bending-like modes around the buckled beam shape. In this case, the bending modes show an $\omega_0 \propto V_g^2$ gate dependence due to the non-zero initial displacement, as discussed above. The modes of such buckled beams can display peculiar mechanical modes similar to those of a hanging swinging chain. A complete analysis of the mechanical modes of strongly buckled CNTs can be found in [16].

In the strong bending regime, the gate voltage dependent spring constant given by Eq. 6.30 results in a significant quadratic contribution to the restoring force. This suggests that the quadratic renormalization of the cubic force coefficient may play an important role in this case, something that should be the subject of further investigation.

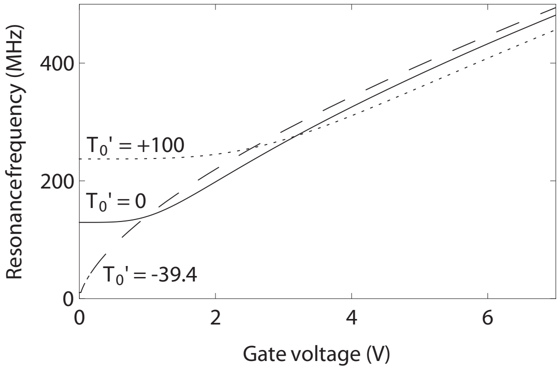

FIGURE 6.3: Simulation showing the resonance frequency as a function of gate voltage for three values of residual tension T_0'. At a high positive residual tension of $T_0' = 100$ (dotted line), the resonance frequency only starts to increase when the tension due to the gate voltage is similar to the residual tension. At zero residual tension $T_0' = 0$ (solid line), the tension due to the gate voltage first has to overcome the bending rigidity in the weak-bending regime with $\omega_0 \propto V_g^2$, and then the strong-bending regime with $\omega_0 \propto V_g^{\frac{2}{3}}$ is entered. At a negative residual tension $T_0' = -39.4$ signifying residual compression (dashed line), the resonance frequency increases significantly with gate voltage even at low gate voltages.

6.1.3 ELECTROSTATIC NONLINEARITY

A second origin of nonlinearity comes from the electrostatic interaction between the CNT and the gate electrode. If for a moment we consider the CNT not to experience Coulomb blockade, but to be a perfect conductor, then it screens the voltage applied to the gate. The electrostatic force between the CNT and the gate was already given in Eq. 6.10 as:

$$F_{ES} = -\frac{dU}{du} = \frac{1}{2}\frac{dC_g}{du}V_g^2. \tag{6.32}$$

In the case of a cylinder above a plate, the capacitance per unit length $c_g = C_g/L$ is given by [15]:

$$c_g(z) = \frac{2\pi\epsilon_0}{\operatorname{arccosh}\left(\frac{h_g - u(z)}{r}\right)}, \tag{6.33}$$

where h_g is the distance between the CNT and the gate. For the example CNT in Table 6.2, this gives values of $5.9\cdot10^{-21}$ F/nm, $3.5\cdot10^{-23}$ F/nm^2, and $2.9\cdot10^{-27}$ F/nm^4 for the first, second, and fourth derivative of the capacitance to gate with respect to displacement respectively. The force acting on the CNT due to electrostatics can be expanded as:

$$F_{ES} = -\Delta k_{ES} u = -\left(\Delta k_{ES,0} + m\alpha_{ES}u^2 + \mathcal{O}(u^4)\right)u, \tag{6.34}$$

and adds to the spring constant as:

$$\begin{aligned} \Delta k_{ES} &= -\frac{dF_{ES}}{du} \\ &= -\frac{1}{2}\frac{d^2C_g}{du^2}V_g^2. \end{aligned} \tag{6.35}$$

The electrostatic force thus gives a contribution to the spring constant that is opposite in sign to the contribution from the restoring force due to bending rigidity and tension. Note, in particular, that the electrostatic forces do *not* act like a restoring force: for example, if the CNT is displaced away from its equilibrium position towards the gate, the electrostatic force pulling it towards the gate *increases*. This has the effect of an “anti”-restoring force. In the case that this electrostatic “anti”-restoring force is larger than the restoring force from the mechanical deformation, the system can even become unstable, leading to a phenomenon of electrostatic “snap in”, in which the device is pulled uncontrollably towards the gate until it makes physical contact.

In the case that the restoring force from mechanical deformation dominates, the system is stable, but the effective spring constant is reduced by the electrostatic interaction. The reduction in the spring constant leads to a decrease in resonance frequency with gate voltage. When the CNT is close enough to the gate so that d^2C_g/du^2 is large, this decrease in resonance frequency is larger than the increase in resonance frequency with gate voltage due to increased tension.

The nonlinearity parameter due to the electrostatic force is:

$$\begin{aligned}\alpha_{ES} &= -\frac{1}{6m}\frac{d^3F_{ES}}{du^3}\\ &= -\frac{1}{12m}\frac{d^4C_g}{du^4}V_g^2.\end{aligned} \tag{6.36}$$

The electrostatic nonlinearity parameter is negative and always gives rise to a softening spring nonlinearity. For the example CNT in Table 6.2, the nonlinearity due to electrostatics is $-3.2\cdot 10^{28}\cdot(V_g \text{ in Volt})^2$ N/(kg m^3). This is of the same order of magnitude as the geometric nonlinearities α_{weak} and α_{strong}, but has an opposite sign.

6.1.4 NONLINEARITY DUE TO SINGLE-ELECTRON TUNNELING

In subsection 4.4.2, we developed a model describing how single-electron tunneling causes a softening spring nonlinearity. Here, we describe how it is also an additional source of nonlinearity. Writing the force on the CNT due to single electron tunneling as:

$$F_{SET} = -\Delta k_{SET}u = -\left(\Delta k_{SET,0} + m\alpha_{SET}u^2 + \mathcal{O}(u^4)\right)u, \tag{6.37}$$

where Δk_{SET} is obtained by combining Eqs. 4.7 and 4.9, gives for the nonlinearity due to single-electron tunneling:

$$\alpha_{SET} = \frac{1}{6m}\frac{d^3F_{SET}}{du^3} = \frac{1}{2m}\frac{d^2\Delta k_{SET}}{du^2} = \frac{1}{2m}\left(\frac{V_g}{C_g}\frac{dC_g}{du}\right)^2\frac{d^2\Delta k_{SET}}{dV_g^2}. \tag{6.38}$$

We now use the expression for Δk_{SET} and insert it into Eq. 6.38. Assuming that the gate voltage difference in which the charge transition occurs is much smaller than the gate voltage, and neglecting terms of d^2C_g/du^2, we arrive at:

$$\alpha_{SET} = -\frac{e}{2m}\frac{V_g^3(V_g - V_{CNT})}{C_g^3C_{tot}}\left(\frac{dC_g}{du}\right)^4\frac{d^3\langle N\rangle}{dV_g^3}. \tag{6.39}$$

Eq. 6.38 shows that the nonlinearity parameter is proportional to the curvature of the change in spring constant and consequently to the curvature of the change in resonance frequency. Figure 6.4 illustrates how the sign of α_{SET} changes with gate voltage: in the middle of the frequency dip caused by single-electron tunneling, the curvature of the change in resonance frequency is positive, leading to a positive nonlinearity, whereas on the left and right side of the frequency dip, both the curvature and the nonlinearity are negative.

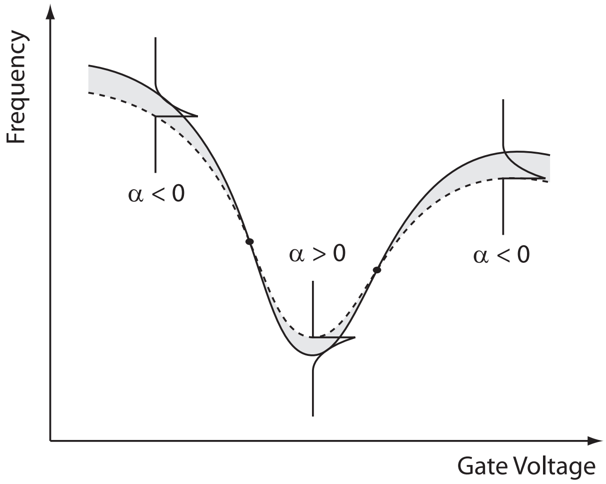

FIGURE 6.4: Comparison of two effects caused by single-electron tunneling: dips in the mechanical frequency and mechanical nonlinearity. When the curvature of the change in resonance frequency is negative, so is the nonlinearity parameter. A positive curvature of the change in resonance frequency leads to a positive nonlinearity parameter.

According to Eq. 6.39, the nonlinearity parameter depends on the third derivative of the average occupancy with respect to gate voltage. Figure 6.5 shows, using the values from the example CNT in Table 6.2, how by changing the gate voltage a few mV, the nonlinearity parameter changes dramatically and even changes sign. For $V_{CNT} \ll V_g$ and a charge transition that occurs in $\Delta V_g = 10$ mV, the example CNT has a minimum (i.e. most negative) nonlinearity due to single-electron tunneling of $\alpha_{SET} = -2.7 \cdot 10^{31} \cdot (V_g \text{ in Volt})^4 \text{N}/(\text{kg m}^3)$. The maximum (i.e. most positive) nonlinearity is $\alpha_{SET} = +8.0 \cdot 10^{31} \cdot (V_g \text{ in Volt})^4\ \text{N}/(\text{kg m}^3)$. At the inflection point of the frequency dip, the cubic, Duffing nonlinearity due to single-electron tunneling vanishes. At this point other nonlinearities, such as the quadratic nonlinearity, will dominate the nonlinear dynamics. Further theoretical investigation of this regime can be found in subsection 4.6.1.

In Table 6.1, the magnitude of the four different contributions to the nonlinearity parameter for the example CNT in Table 6.2 is depicted. The table demonstrates that the nonlinearity due to single-electron tunneling, α_{SET}, is similar in size to the beam-like geometric nonlinearity, α_{beam}. Which nonlinearity dominates depends on the gate voltage and the gate voltage range over which the charge transition occurs. The nonlinearities due to weak-bending and strong-bending and the electrostatic nonlinearity have almost the same value, but opposite sign, and can be

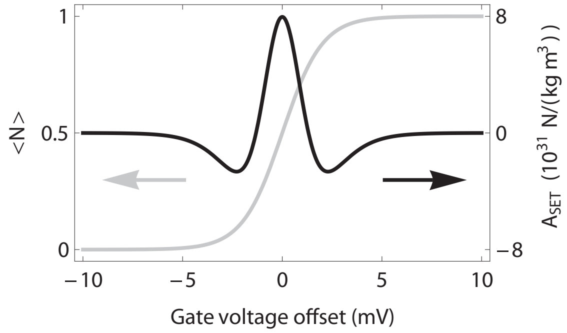

FIGURE 6.5: Calculated average occupancy (left axis) and the nonlinearity parameter α_{SET} due to single-electron tunneling (right axis): α_{SET} depends on the third derivative of the average occupancy with respect to gate voltage, thus going from negative to positive to negative again in only a few mV.

neglected for a quantum dot CNT resonator.

Nonlinearity (N/(kg m^3))	$V_g = 1$ V	$V_g = V_g^* = 2.1$ V	$V_g = 5$ V
$\alpha_{SET,max}$ ($\Delta V_g = 10$ mV)	$8.0 \cdot 10^{31}$	$1.5 \cdot 10^{33}$	$5.0 \cdot 10^{34}$
$\alpha_{SET,min}$ ($\Delta V_g = 10$ mV)	$-2.7 \cdot 10^{31}$	$-5.2 \cdot 10^{32}$	$-1.7 \cdot 10^{34}$
$\alpha_{SET,max}$ ($\Delta V_g = 1$ mV)	$8.0 \cdot 10^{34}$	$1.5 \cdot 10^{36}$	$5.0 \cdot 10^{37}$
$\alpha_{SET,min}$ ($\Delta V_g = 1$ mV)	$-2.7 \cdot 10^{34}$	$-5.2 \cdot 10^{35}$	$-1.7 \cdot 10^{37}$
α_{ES}	$-3.2 \cdot 10^{28}$	$-1.4 \cdot 10^{29}$	$-7.9 \cdot 10^{29}$
α_{weak}	$8.7 \cdot 10^{28}$	$1.7 \cdot 10^{30}$	-
α_{strong}	-	$5.0 \cdot 10^{28}$	$1.6 \cdot 10^{29}$
α_{beam}	$9.6 \cdot 10^{34}$	$9.6 \cdot 10^{34}$	-

TABLE 6.1: Comparison of the magnitude of the parameters for the four contributions to the nonlinearity parameter for the example CNT in Table 6.2. For the nonlinearities due to single-electron tunneling, the gate voltage range ΔV_g over which the charge transition occurs is indicated. The nonlinearities in the weak-bending or beam-like (strong-bending) regime are not calculated above (below) the crossover voltage V_g^*.

6.2 PARAMETRIC EXCITATION AND MODE COUPLING IN CARBON NANOTUBE RESONATORS

The previous section showed how geometry, electrostatics, and single-electron tunneling give rise to a Duffing-type nonlinearity. In addition to a nonlinear response to large powers at the resonance frequency, nonlinear effects can also be observed when driving the resonator at frequencies different from its resonance frequency.

In the next subsection, we look at how nonlinearities in CNTs can result in parametric driving and amplification. In subsection 6.2.2, we consider other modes of oscillation, either in another dimension of oscillation, giving rise to nonplanar motion, or as higher order modes in the same direction. Through the nonlinear behaviour of the device, these other modes become coupled to the fundamental mode. As we will see, driving these other modes can generate, for example, extra tension in the device, which can then shift the frequency of the fundamental mode.

6.2.1 PARAMETRIC EXCITATION

A resonator is parametrically excited when, besides a driving force around ω_0, there is also a change in one of its parameters around $2\omega_0$. A well-known example entails a child on a swing, which alters its center of mass during swinging. In this analysis we only consider a modulation of the spring constant, so that $k = k_0 + k_p \cos(\omega_p t)$.

The pumping of energy into the motion through parametric excitation is maximum when done at twice the resonance frequency, but can be done at any frequency for which $\omega_p = \frac{2}{n}\omega_0$, becoming less effective for larger n. The equation of motion describing parametric excitation is:

$$\frac{\partial^2 u}{\partial t^2} + \frac{\omega_0}{Q}\frac{\partial u}{\partial t} + \frac{1}{m}\left(k_0 + k_p \cos(\omega_p t)\right) u = \frac{F_{ac}}{m}\cos(\omega_d t). \tag{6.40}$$

In the case of capacitive driving at ω_p, the change in the spring constant can be described as:

$$\begin{aligned} \Delta k = -\frac{dF}{du} &= \frac{1}{2}\frac{d^2 C_g}{du^2}\left((V_g^{dc})^2 + 2V_g^{dc}V_g^{ac} cos(\omega_p t) + (V_g^{ac})^2\cos(2\omega_p t)\right) \\ &= \Delta k_0 + k_p \cos(\omega_p t) + k_p' \cos(2\omega_p t), \end{aligned} \tag{6.41}$$

yielding an extra modulation of the spring constant k_p' at $2\omega_p$. For low drive powers, $V_g^{ac} \ll V_g^{dc}$, so that $k_p' \ll k_p$, and k_p' can be neglected. The most effective parametric excitation can then be achieved by driving at $\omega_p = 2\omega_0$.

Recently, parametric excitation has been applied to a CNT resonator [17]. A CNT resonator is especially suited for parametric excitation because the change in spring constant with drive voltage, dk/dV_g, is large (see Eqs. 6.26 and 6.30).

6.2.2 MODE COUPLING

Until now we have only considered oscillations of the fundamental mode taking place in the x-direction. In this section we discuss coupling between the fundamental mode in the x-direction to the fundamental mode in the y-direction [18–20] and between the fundamental mode in the x-direction and higher modes in the x-direction [21]. Both types of mode coupling can generically be described by the following two coupled equations:

$$\rho A \frac{\partial^2 u}{\partial t^2} + \eta \frac{\partial u}{\partial t} + D \frac{\partial^4 u}{\partial z^4} - (T_{dc} + T_u + T_v) \frac{\partial^2 u}{\partial z^2} = f_u, \tag{6.42}$$

$$\rho A \frac{\partial^2 v}{\partial t^2} + \eta \frac{\partial v}{\partial t} + D \frac{\partial^4 v}{\partial z^4} - (T_{dc} + T_u + T_v) \frac{\partial^2 v}{\partial z^2} = f_v. \tag{6.43}$$

Analogously to Eq. 6.14, the displacement of the other mode is denoted by:

$$v_{ac} = \mathscr{B}(t)\psi(z). \tag{6.44}$$

Here, $\mathscr{B}(t)$ is the slowly varying amplitude of the other mode, root-mean-squared along the CNT, and $\psi(z)$ depicts the modeshape.

The different parts of the tension on the CNT by the oscillations u and v are given by:

$$T_u = \frac{EA}{2L} \int_0^L \left(\frac{\partial u_{ac}}{\partial z} \cos(\omega_u t) \right)^2 dz, \tag{6.45}$$

$$T_v = \frac{EA}{2L} \int_0^L \left(\frac{\partial v_{ac}}{\partial z} \cos(\omega_v t) \right)^2 dz. \tag{6.46}$$

Here T_u causes the nonlinearity for a beam as described in section 6.1.

The tension arising from the oscillation of v is:

$$\begin{aligned} T_v &= \frac{EA}{2L} \mathscr{B}^2 \left(\frac{1}{2} + \frac{1}{2}\cos(2\omega_v t) \right) \int_0^L \left(\frac{\partial \psi}{\partial z} \right)^2 dz \\ &= \frac{EAb_n^v}{4L^2} \mathscr{B}^2 + \frac{EAb_n^v}{4L^2} \mathscr{B}^2 \cos(2\omega_v t), \end{aligned} \tag{6.47}$$

remembering $\int_0^L \left(\frac{\partial \psi}{\partial z} \right)^2 dz = b_n^v / L$. This means that there is both a contribution to the dc tension and there is a change in the ac tension at $2\omega_v$.

Let us first look at the contribution to the dc tension in the weak-bending limit. Using Eq. 6.25 and 6.47 in the limit of $T_v \ll EI/L^2$, the change in resonance frequency due to mode coupling is:

$$\Delta\omega_0^{weak} = \sqrt{\frac{EA}{\rho I}} \frac{b_n^v}{8L^2} \mathscr{B}^2. \tag{6.48}$$

For CNTs, the high Young's modulus, low mass density, high ratio of $A/I = 4/r^2$, and small length cause a large change in resonance frequency due to nonplanar motion. For the example CNT from Table 6.2, this gives a tuning of 16 MHz/nm^2 when the other mode is the fundamental mode in the y-direction. For the third mode the tuning of the fundamental mode for the example CNT is 127 MHz/nm^2, arising from a higher b_n^v.

In the strong-bending limit with $T_v \ll T_{dc}^{strong}$, using Eq. 6.29 leads to the change in resonance frequency due to mode coupling:

$$\begin{aligned}\Delta\omega_0^{strong} &= \frac{\pi}{2L\sqrt{\rho A}}\frac{T_v}{\sqrt{T_{dc}^{strong}}}\\ &= \frac{\pi (EA)^{\frac{5}{6}} b_n^v}{4\cdot 2^{\frac{1}{6}} L^3}\left(\frac{dC_g}{du}\right)^{-\frac{1}{3}} V_g^{-\frac{2}{3}}\mathscr{B}^2. \qquad (6.49)\end{aligned}$$

As the tension due to the gate electrode increases, the added tension from mode coupling is less important. At $V_g = 5$V the tuning of the fundamental mode of the example CNT due to another fundamental mode and due to a third mode is reduced to 3.3 MHz/nm^2 and 26 MHz/nm^2 respectively.

6.3 CONCLUSIONS

Carbon nanotubes display a rich variety in nonlinear effects. In the first section of this Chapter, we covered the four different contributions to the nonlinear oscillation of a CNT resonator: the beam-like nonlinearity, the nonlinearity due to gate-induced tension, the electrostatic nonlinearity, and the nonlinearity due to single-electron tunneling, the combination of which is unique to CNT resonators. In the second section, we show how the large response of the resonance frequency of a CNT resonator to a change in gate voltage or tension makes CNT resonators ideally suited for parametric excitation and mode coupling.

Acknowledgments: We thank Hidde Westra, Giorgi Labadze, Yaroslav Blanter, and Menno Poot for fruitful discussions and we acknowledge the financial support of the Future and Emerging Technologies programme of the European Commission, under the FET-Open project QNEMS (233992).

6.4 APPENDIX

Table 6.2 gives an overview of the symbols used in this chapter for variables and constants along with typical values and example device parameters.

General properties of single-walled CNTs

E	Young's modulus	1.3 TPa
ρ	mass density	1350 $\mathrm{kg/m^3}$

Example CNT

L	length	800 nm
r	radius	1.5 nm
h_g	distance to gate	230 nm
C_g	capacitance to gate	10 aF
C_{tot}	total capacitance	20 aF
Q	quality factor	100,000
$\omega_0/2\pi$	resonance frequency	140 MHz
I	second moment of inertia	4.0 $\mathrm{nm^4}$
A	cross-sectional area	7.1 $\mathrm{nm^2}$

Variables

$u(z,t)$	displacement	-
$\mathscr{A}(t)$	slowly-changing amplitude	-
$\xi(z)$	mode shape	-

TABLE 6.2: General properties of a single-walled CNT, device parameters for a CNT used as an example in the previous sections, and variables.

REFERENCES

[1] H. B. Meerwaldt, G. A. Steele, and H. S. J. van der Zant, *Fluctuating Nonlinear Oscillators* (Oxford University Press, 2012), chap. Carbon nanotubes: Nonlinear high-Q resonators with strong coupling to single-electron tunneling, pp. 312–340, URL `http://arxiv.org/abs/1205.4921`.

[2] R. Lifshitz and M. C. Cross, *Review of nonlinear dynamics and complexity* (John Wiley and Sons, New York,, 2008), chap. Nonlinear dynamics of nanomechanical and micromechanical resonators, URL `http://bitly.com/ZdtfxJ`.

[3] M. I. Dykman and V. N. Smelyansky, *Quantum-Theory Of Transitions Between*

Stable States Of A Nonlinear Oscillator Interacting With The Medium In A Resonant Field, Zhurnal Eksperimentalnoi I Teoreticheskoi Fiziki **94**, 61 (1988), URL `http://bitly.com/WUhZrh`.

[4] H. G. Craighead, *Nanoelectromechanical systems*, Science **290**, 1532 (2000).

[5] K. L. Ekinci and M. L. Roukes, *Nanoelectromechanical systems*, Review of Scientific Instruments **76**, 061101 (2005).

[6] H. W. C. Postma, I. Kozinsky, A. Husain, and M. L. Roukes, *Dynamic range of nanotube- and nanowire-based electromechanical systems*, Applied Physics Letters **86**, 223105 (2005).

[7] L. Landau and E. Lifshitz, *Mechanics*, vol. 1 of *Course of theoretical physics* (Pergamon Press Ltd, Oxford, 1960).

[8] B. Yurke, D. S. Greywall, A. N. Pargellis, and P. A. Busch, *Theory Of Amplifier-Noise Evasion In An Oscillator Employing A Nonlinear Resonator*, Physical Review A **51**, 4211 (1995).

[9] M. Poot and H. S. J. van der Zant, *Mechanical systems in the quantum regime*, Physics Reports-Review Section of Physics Letters **511**, 273 (2012).

[10] M. Dequesnes, S. V. Rotkin, and N. R. Aluru, *Calculation of pull-in voltages for carbon-nanotube-based nanoelectromechanical switches*, Nanotechnology **13**, 120 (2002).

[11] A. Krishnan, E. Dujardin, T. W. Ebbesen, P. N. Yianilos, and M. M. J. Treacy, *Young's modulus of single-walled nanotubes*, Physical Review B **58**, 14013 (1998).

[12] V. N. Popov, V. E. Van Doren, and M. Balkanski, *Elastic properties of single-walled carbon nanotubes*, Physical Review B **61**, 3078 (2000).

[13] A. N. Cleland, *Foundations of Nanomechanics: from solid-state theory to device applications* (Springer-Verlag, Berlin, 2003).

[14] A. Nayfeh, *Nonlinear interactions: analytical, computational, and experimental methods* (Wiley-Interscience, New York, 2000).

[15] S. Sapmaz, Y. M. Blanter, L. Gurevich, and H. S. J. van der Zant, *Carbon nanotubes as nanoelectromechanical systems*, Physical Review B **67**, 235414 (2003).

[16] H. Üstünel, D. Roundy, and T. A. Arias, *Modeling a suspended nanotube oscillator*, Nano Letters **5**, 523 (2005).

[17] A. Eichler, J. Chaste, J. Moser, and A. Bachtold, *Parametric Amplification and Self-Oscillation in a Nanotube Mechanical Resonator*, Nano Letters **11**, 2699 (2011).

[18] C. H. Ho, R. A. Scott, and J. G. Eisley, *Non-planar, non-linear oscillations of a beam - 1 Forced motions*, International Journal of Non-Linear Mechanics **10**, 113 (1975).

[19] W. G. Conley, A. Raman, C. M. Krousgrill, and S. Mohammadi, *Nonlinear and nonplanar dynamics of suspended nanotube and nanowire resonators*, Nano Letters **8**, 1590 (2008).

[20] S. Perisanu, T. Barois, A. Ayari, P. Poncharal, M. Choueib, S. T. Purcell, and P. Vincent, *Beyond the linear and Duffing regimes in nanomechanics: Circularly polarized mechanical resonances of nanocantilevers*, Physical Review B **81**, 165440 (2010).

[21] H. J. R. Westra, M. Poot, H. S. J. van der Zant, and W. J. Venstra, *Nonlinear modal interactions in clamped-clamped mechanical resonators.*, Physical Review Letters **105**, 117205 (2010).

7

HIGH-BANDWIDTH READOUT OF CARBON NANOTUBE MECHANICAL MOTION

> *With your consent,*
> *I can experiment*
> *further still.*
>
> Genesis - Entangled

In this chapter, we discuss the use of a high-bandwidth readout scheme for the detection of the mechanical motion of a carbon nanotube. Section 7.1 motivates the high-bandwidth readout scheme by describing several physical phenomena which can be observed by using the readout scheme. High-bandwidth readout entails either direct readout at the mechanical resonance frequency or the use of a mixing technique with a sufficiently high intermediate frequency, $\Delta\omega$. In section 7.2, it is explained why the experiments to observe these phenomena are not possible with current methods. Section 7.3 deals with the experimental challenges facing the high-bandwidth readout, such as the use of a high-impedance amplifier and minimization of the crosstalk from drive signals. Section 7.4 lays out the experimental results obtained with the measurement technique. The appendix in section 7.5 deals with the practical details such as the fabrication of local-gate devices and the custom design of a printed circuit board that is compatible with high-bandwidth readout.

7.1 MOTIVATION

The motivation for the development of the high-bandwidth readout scheme can be divided into three aspects. The first aspect is to detect the decay of the amplitude of the mechanical resonator at a timescale of Q/ω_0, allowing the investigation of energy relaxation and quantum nonlinearity. The second aspect is to determine the resonance frequency at a fast timescale, allowing time-resolved measurements of adsorption and desorption of atoms and molecules. The third aspect is to detect undriven motion in the form of thermal motion, zero-point motion, and self-sustained oscillation.

Energy relaxation of the mechanical motion of a CNT resonator can be investigated with the high-bandwidth readout scheme by looking at the transient response. Until now, the quality factor, quantifying energy relaxation, has only been obtained by looking at the full width at half maximum, f_{FWHM}, of the driven amplitude response, $Q = f_0/f_{FWHM}$. However, broadening of the resonance peak comes about through two contributions: energy relaxation and frequency instability (phase noise). Experimental observations of quality factors at room temperature [1–3] have given values significantly lower than might be expected. It has been proposed [4] that frequency instability arises from the thermal motion of other modes, coupled through tension. Extracting the quality factor from the transient response through the decay time, $\tau = 2Q/\omega_0$, allows us to distinguish between energy relaxation and frequency instability.

A second motivation for the detection of transient motion of a CNT resonator is related to quantum nonlinearity. Classically, strongly driven resonators exhibit bistability, giving rise to a small amplitude and a large amplitude metastable state. By applying noise, switching occurs between the two metastable states [5, 6]. Also, experiments on micromechanical beams [7] have shown that it is possible to kick the resonator out of its metastable state by applying an excitation pulse. As the amplitude of the resonator decays, it then ends up in either one of the two states, depending on the amplitude and duration of the excitation pulse in a deterministic way. At millikelvin temperatures, $\hbar\omega_0 > k_b T$, and quantum mechanical effects become important, giving rise to quantum dynamics with a different path in phase space through the attractor. Investigation of quantum nonlinearity [8] could lead to insights into phenomena such as tunneling [9, 10] and quantum activation [11] between the two metastable states of oscillation and the occupation of states that are classically not available [12]. In order to study these effects, the motion of the CNT must be monitored on timescales faster than $2Q/\omega_0$.

Mass sensing experiments using CNT mechanical resonators have an extraordinary mass resolution of a yoctogram [13]. In these experiments, a small number of particles are evaporated into the vacuum chamber. A shift in the resonance frequency demonstrates the absorption of a single particle or many particles at once. High-bandwidth readout could allow measuring the resonance frequency at a timescale that is fast enough to observe the individual particles adsorb onto and desorb from the CNT at high evaporation rates [14].

High-bandwidth readout of a CNT resonator is a useful technique for observing its undriven motion in the form of thermal motion, zero-point motion, or when it exhibits a self-sustained oscillation. The investigation of undriven motion is interesting as a stepping stone towards quantum mechanical effects such as the superposition of a macroscopic object and coherent coupling of a mechanical element to a qubit [15–17]. CNTs are viable test objects for this, because they reach the ground state readily at millikelvin temperatures, when the energy of a single phonon exceeds the thermal energy ($\hbar\omega_0 \gg k_B T$).

Self-sustained oscillation occurs when the resonator has a finite amplitude of motion, but no dynamic excitation has been supplied. In an active feedback scheme [18], the signal arising from the thermal motion is fed back into the system as an excitation, after its phase has been altered to give optimal gain. In CNT quantum dot resonators, single-electron tunneling is experimentally found (cf. Chapter 3) to cause a self-sustained oscillation. This is predicted [19] to occur in the regime where the average charge on the CNT decreases instead of increases as the CNT approaches the gate electrode. In that case, any present motion (e.g. thermal motion) is amplified as the tunneling electrons pump energy into the CNT resonator. In order to discern self-sustained oscillation, high-bandwidth readout is useful, allowing the determination of the frequency of the self-oscillation.

7.2 COMPARISON TO CURRENT METHODS

In this section, we discuss the shortcomings of current electronic measurement techniques for performing the experiments outlined in the previous section, by examining if they fulfill the following three criteria:

1. Can undriven motion be detected?
2. How fast can an amplitude response be measured?
3. What is the bandwidth of the technique compared to the rate of change of the phenomenon under investigation?

Current electronic CNT measurement techniques can be divided into what we label low-frequency mixing techniques and the rectification technique. These are described in detail in Chapter 2. Both two-source mixing and frequency-modulation (FM) mixing supply a signal at the source of the CNT, at a frequency of $\Delta\omega$ away from the drive frequency. The probe signal causes a voltage difference between the CNT and the gate. For low-frequency mixing with $\Delta\omega < \omega/Q$, the probe signal now also drives the resonator, as illustrated in Fig. 7.1. The first criterion fails, as motion cannot be probed without driving it.

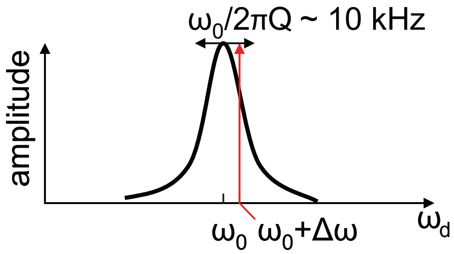

FIGURE 7.1: Low frequency mixing: a signal provided at the source electrode at $\omega_d + \Delta\omega$ excites the mechanical resonator, when the mechanical resonance is broad ($\omega_{FWHM} = \omega_0/Q$) compared to the mixing difference frequency $\Delta\omega$.

Related to the second and third criterion, the low-frequency signal, detected at $\Delta\omega/2\pi \approx 10$ kHz, is accompanied by significant $1/f$ noise. This makes it necessary to average with a lock-in amplifier using a timeconstant of 100-300 ms. An amplitude response takes several seconds to be performed. Also, the decay of a CNT mechanical resonator, occurring at timescales of $2Q/\omega$ corresponding to microseconds, gets smeared out. For the reasons mentioned above, low-frequency mixing techniques are unsuitable for detecting undriven motion, acquiring fast amplitude responses, or detecting the transient response.

The same conclusion can be drawn for the rectification technique. The mechanical motion is now detected as a change in the dc current flowing through the CNT quantum dot at a certain drive frequency; no information is obtained about the frequency at which the CNT is resonating. When no drive is supplied, undriven motion leads to a change in the dc current, but this change is difficult to distinguish from other effects, such as thermal broadening, and, again, gives no information on the resonance frequency. The bandwidth of the technique is limited by the low-pass RC-filter originating from the large resistance of the CNT, combined with the large capacitance of the dc wire connected to the drain. The cut-off frequency of this low-pass filter is of the order of kHz. This causes the measurement time to be too slow to acquire fast amplitude responses and makes it impossible to measure transient motion.

7.3 EXPERIMENTAL CHALLENGES

7.3.1 A CLOSE-PROXIMITY HIGH-IMPEDANCE AMPLIFIER

In this subsection, we discuss the use of a high electron mobility transistor (HEMT) amplifier to achieve a high signal and a high bandwidth with which to detect the CNT's mechanical motion. We focus on two main characteristics: a high input impedance and the close proximity to the device. We show how this technique solves the issues that arise from using either the low-frequency mixing techniques or the rectification technique.

The difficulty of measuring the high-frequency motion of a CNT mechanical resonator lies mainly in its high resistance. The information about its mechanics is found in the current flowing through the CNT. Characteristics of the circuit, such as gain and cut-off frequency, are determined by the value of the resistor over which this current is measured, $R_{readout}$, relative to the CNT's resistance, R_{CNT}. The voltage, V_{out}, resulting from this voltage divider of the CNT's resistance and the readout resistance, is given by:

$$V_{out} = V_{in} \frac{R_{readout}}{R_{readout} + R_{CNT}}. \tag{7.1}$$

If a small value is chosen for the readout resistance, a large part of the signal is lost, proportional to $R_{readout}/R_{CNT}$. If too large a value for the readout resistance is chosen, $R_{readout} \gg R_{CNT}$, the output voltage becomes independent of the resistance of the CNT, and the information about the mechanics is lost. A prudent choice is a readout resistance at around the CNT's resistance. The result of using a readout resistance as large as the CNT's resistance, is that the impedance to ground due to the capacitance of the wires, $C_{readout}$, becomes important (see Figure 7.2). The output voltage, with this capacitance taken into account, reads:

$$V_{out}(\omega) = V_{in} \frac{1}{1 + R_{CNT}/R_{readout} + i\omega R_{CNT} C_{readout}}. \tag{7.2}$$

This reduces to Equation 7.1 for negligible capacitances. The output voltage is frequency-dependent, where the cut-off frequency is given by $f_c = 1/2\pi R_{par} C_{readout}$, with $R_{par} = 1/(1/R_{CNT} + 1/R_{readout})$ the parallel resistance of the CNT and the readout resistor. To maximize the output voltage and minimize the cut-off frequency, the capacitance can be lowered by measuring the voltage as closely as possible to the drain of the CNT. For these reasons, we use a close-proximity, high-impedance HEMT amplifier, which is only several millimeters away from the drain of the CNT. The gate of the amplifier, which is shorted to ground through the readout resistor of 5.6 kΩ, is connected by a wire-bond to the drain of the CNT. The design of the printed circuit board, on which the HEMT amplifier is placed, is described in section 7.5.1.

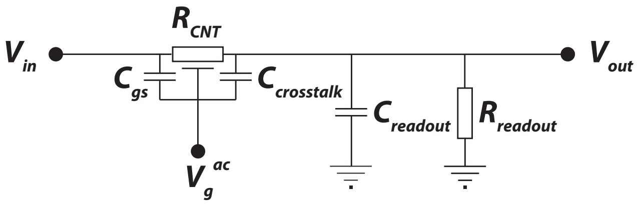

FIGURE 7.2: Simplified electrical circuit diagram of the CNT three terminal device: Voltages V_{in} and V_g^{ac} are applied to the source and gate of the CNT device respectively. The voltage divider of the readout resistance and capacitance, $R_{readout}$ and $C_{readout}$ respectively, combined with the CNT's resistance, R_{CNT}, determine the measured output voltage, V_{out}. The input voltage leaks to the gate for a high value of the gate-source capacitance, C_{gs}. Crosstalk arises due the capacitance, $C_{crosstalk}$, between the gate and the drain of the CNT, as an ac gate voltage, V_g^{ac}, is applied.

7.3.2 MINIMIZING THE CAPACITIVE CROSSTALK

To drive and read out the CNT mechanical resonator, a nearby gate electrode is needed. Close proximity of the electrode is important, so that the capacitance between the CNT and the gate electrode is large. In that case, only a small voltage is needed on the gate to induce a charge on the CNT or to excite it into motion. Furthermore, the close proximity gives rise to a large change in capacitance when the CNT moves, making the mechanical motion more easily detectable.

In contrast, the capacitance between the gate electrode and the source and drain electrodes should be as small as possible for three reasons (see Figure 7.2). First, when the capacitance between source and gate is large, the ac probe signal applied to the source leaks away to ground through the gate and does not pass through the CNT. Secondly, when the capacitance between drain and gate is large, the drive signal applied to the gate leaks to the drain. This is a problem when the mechanical signal to be detected is at the same frequency as the drive signal. For direct readout, it is therefore important to minimize this capacitance [20, 21]. This issue can, however, be avoided by mixing the mechanical output signal away from the drive frequency. The contribution of the crosstalk signal to the output signal, ΔV_{out}, occurring at ω_d, is given by:

$$\Delta V_{out}(\omega_d) = V_g^{ac}\left(1+\frac{1}{i\omega_d R_{par} C_{crosstalk}}+\frac{C_{readout}}{C_{crosstalk}}\right)^{-1}. \tag{7.3}$$

Thirdly, a large capacitance between drain and gate increases $C_{readout}$, reducing the cut-off frequency of the system and decreasing the signal at high frequencies.

The requirements of large coupling to the CNT and small crosstalk capacitances to the source and drain are aided by employing a local-gate geometry. The traditional use of a global back gate causes a large capacitance between the gate and the source and drain electrodes at the bondpads. To decrease this, the p++-doped silicon wafer, acting as a back gate, is replaced by a wafer made from highly resistive intrinsic silicon. The gate electrode is then only fabricated locally at the trench between the source and drain electrode, far away from the bondpads. The fabrication of the local-gate CNT devices is described in the appendix in section 7.5.2.

7.4 EXPERIMENTAL RESULTS

To perform the high-bandwidth readout of the CNT mechanical resonator, a two-source mixing measurement scheme is used, as shown in Figure 7.3. Excitation and measurement is performed using a Zurich Instruments HF2LI high-frequency lock-in amplifier and a signal generator. The ac gate voltage at ω_d is supplied by the signal generator. The ac source voltage at $\omega_d \pm \Delta\omega$ is generated by mixing the signal generator's output with the reference signal of the lock-in amplifier at $\Delta\omega$. The ac voltages at the source and gate are mixed by the CNT, both mechanically and electrically, to a mixing current at $\Delta\omega$. The gate of the HEMT amplifier is wire-bonded to the drain of the CNT. The mixing current flowing through the CNT is measured at the CNT's drain, as it generates a voltage over the 5.6 kΩ readout resistor. This voltage on the gate of the HEMT amplifier modulates the current supplied by V_{dd}, which is subsequently amplified and measured by the lock-in amplifier. The voltage difference between the gate and the source of the HEMT amplifier is tuned through a resistor, R_{tune}.

We now characterize the electrical and mechanical properties of the CNT device. Figure 7.4a shows the conductance through the CNT resonator at room temperature as a function of gate voltage. The conductance is measured by applying a dc bias voltage of 10 mV and measuring the current. The v-shaped conductance signifies an ultraclean small-bandgap CNT. Figure 7.4b shows the Y-component of the mixing voltage as a function of gate voltage and drive frequency, measured by the lock-in amplifier at an intermediate frequency (IF) of $\Delta\omega/2\pi = 6$ MHz and a time constant, τ, of 1 μs. The Y-quadrature of the lockin signal is plotted as it shows the highest contrast. For clarity, the background current for each drive frequency is subtracted. Figure 7.4b shows the fundamental resonance, which is tunable by the gate voltage. Two faint lines at higher frequency correspond to higher modes. The figure demonstrates, for the first time, readout of CNT mechanical motion with a timeconstant of 1 μs.

To determine the bandwidth of the HEMT amplifier, a vector network analyzer measurement is performed at zero gate voltage. Figure 7.5a shows the gain of the circuit. The 24 dB amplification of the second amplifier, and the attenuation due to the voltage divider of the CNT's resistance with the readout resistance are ac-

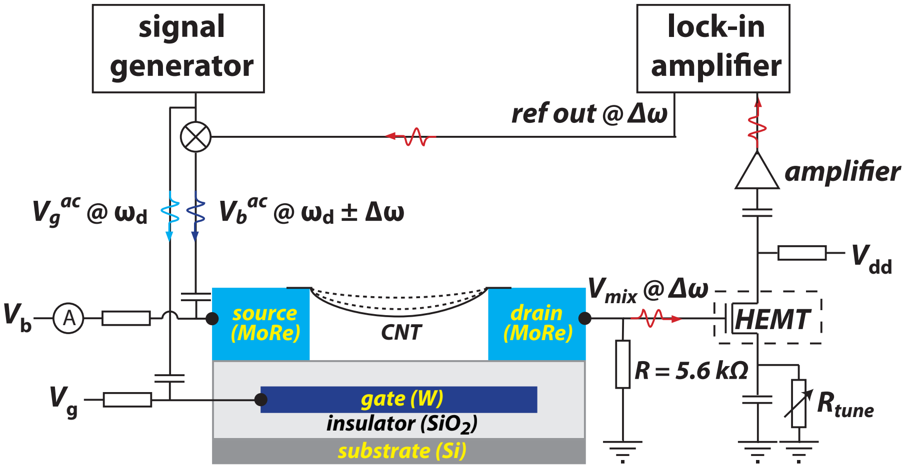

FIGURE 7.3: The measurement setup can be divided into three parts. i) Excitation is performed using a signal generator, a lock-in amplifier, and a mixer, supplying signals at ω_d and $\omega_d \pm \Delta\omega$. ii) The device consists of a CNT suspended between two MoRe electrodes and a tungsten local gate buried in SiO_2. The device mixes the two signals back to $\Delta\omega$, mechanically and electrically. iii) The HEMT circuit measures the mixing current, as it generates a voltage over the 5.6 kΩ resistor. This voltage on the gate of the HEMT amplifier modulates the current supplied by V_{dd}, which is subsequently amplified and measured by the lock-in amplifier.

counted for. At frequencies below 24 MHz, the gain is not completely flat. Above 24 MHz, a gain of 9.3 dB is visible and a bandwidth of $f_{3dB} = 62$ MHz is determined. Qualitatively, the behavior of the gain can be understood using a first-order RC model of the CNT resistor and the drain's parasitic capacitance, which causes the roll-off above f_{3dB}. The parasitic capacitance, which arises from the input capacitance of the HEMT amplifier and the capacitance of the drain bondpad, is calculated to be as low as 0.5 pF. The capacitance of the drain bondpad to ground is estimated to take up 0.4 pF, but the accompanying impedance is significantly increased due to the intrinsic silicon substrate, which is still highly resistive at room temperature. Figure 7.5b shows the power of the mixing voltage at $\Delta\omega/2\pi = 6$ MHz, clearly above the noise that decreases with frequency.

Figure 7.5c shows a frequency trace at a gate voltage of $V_g^{dc} = 4.95$ V. At an intermediate frequency of $\Delta\omega/2\pi = 6$ MHz, and a lockin timeconstant of $\tau = 780$ ns, the mechanical resonance is clearly visible as a dip of $V_Y^{mech} = 330\ \mu$V. The amplitude of the mechanical oscillation is estimated by comparing the mechanical contribution of the mixing signal, V_Y^{mech}, to the electrical contribution, $V_Y^{elec} = 5$ mV [3]:

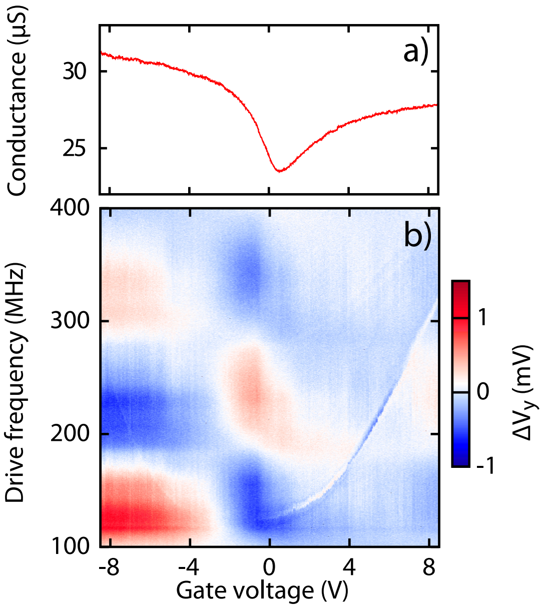

FIGURE 7.4: A carbon nanotube electromechanical resonator: a) Conductance of the CNT in series with two 5.6 kΩ resistors as a function of gate voltage, showing an ultraclean small-bandgap CNT. b) Resonances of three mechanical modes, tunable with gate voltage, measured as the Y-component of the mixing voltage at $\Delta\omega/2\pi = 6$ MHz and $\tau = 1$ μs.

$$u = \frac{V_Y^{mech}}{V_Y^{elec}} \frac{V_g^{ac}}{V_g^{dc}} h_0 \ln(2h_0/r). \tag{7.4}$$

Using the distance between CNT and gate h_0 = 200 nm, a typical single-walled CNT's radius r = 1.5 nm, and the excitation voltage on the gate V_g^{ac} = 100 mV, the amplitude of motion is estimated at 1.5 nm. The lineshape of the mechanical resonance depends on the phase difference between the mechanical and the electrical mixing current. The sharp edge in Fig. 7.4c suggests nonlinear oscillation, which can be expected at an amplitude comparable to the CNT's radius. With a lockin settling time of 7.8 μs, this measurement can in principle be performed in 1.4 ms, allowing determination of the resonance frequency with a millisecond time resolution.

Transients of the electrical and mechanical mixing currents are investigated by pulsing the drive signal with a radio-frequency switch and by reading the Y-component of the mixing signal, as measured by the lockin amplifier, with an oscilloscope. Figure 7.5d shows a single-shot measurement of the exponential decay of the off-resonance mixing signal at a timeconstant of 10 μs (blue) and 780 ns (dashed red). The figure demonstrates that, up until a timeconstant of 780 ns, the decay of the mixing current is dominated by the lockin amplifier's timeconstant and not the bandwidth of the CNT-HEMT circuit. The green line displays the on-resonance signal at τ = 780 ns, which is clearly distinguishable from the electrical signal. The mechanical signal, as the difference of the on-resonance and off-resonance signal, decays faster than 780 ns. This is also found at other gate voltages (not shown), which gives the room-temperature quality factor an upper bound due to energy relaxation of $Q < \omega_0\tau/2 = 490$.

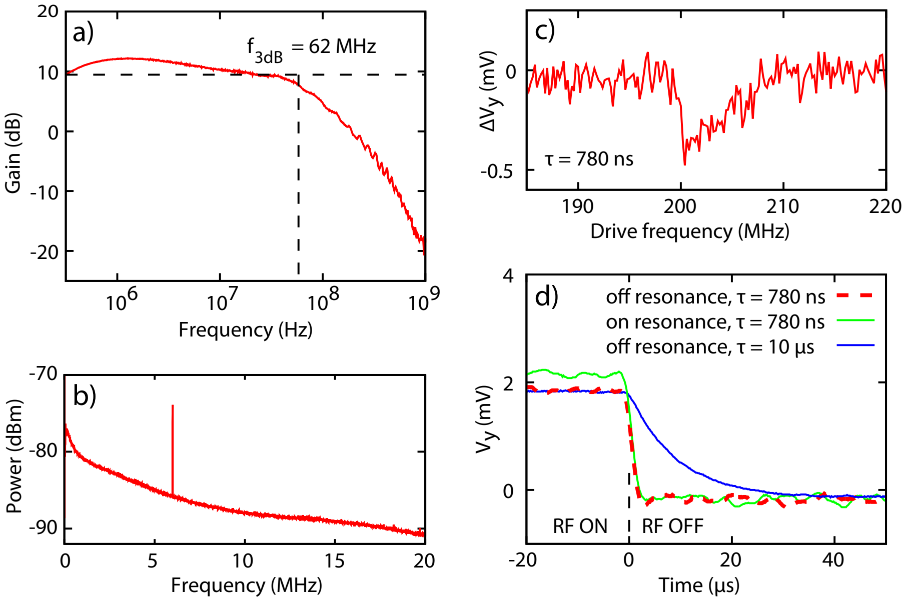

FIGURE 7.5: High-bandwidth readout: a) Gain of the HEMT amplifier, showing a bandwidth of f_{3dB} = 62 MHz. b) Spectrum of the output signal, showing the mixing voltage as a peak at $\Delta\omega/2\pi$ = 6 MHz. c) Mechanical resonance at V_g = 4.95 V, measured with $\Delta\omega/2\pi$ = 6 MHz and τ = 780 ns. d) Single-shot measurement of the decay of the Y-component of the electrical mixing signal at $\Delta\omega/2\pi$ = 6 MHz, showing the off-resonance decay at a timeconstant of τ = 10 μs (blue), and 780 ns (red dashed), and the decay at the mechanical resonance at τ = 780 ns (green).

The high-bandwidth readout described in this Chapter can be used to investigate the unexpected low quality factor of pristine CNT resonators at room temperature, as determined through driven spectral measurements. At a cryogenic quality factor of 10,000, the mechanical decay time of $2Q/\omega_0$ = 16 μs allows distinguishing between spectral broadening [4] and energy relaxation. When the mechanical resonator is driven to large amplitudes, nonlinear dynamics can be observed while the resonator decays into one of the two bistable states [22], potentially in the quantum regime [9, 12]. The high-bandwidth readout allows measuring with a large $\Delta\omega$, outside of the mechanical bandwidth. Undriven motion such as thermal motion [23], zero-point motion, and self-sustained oscillation through single-electron tunneling (see [19] and Ch. 3) can be investigated, because the mechanical motion is now probed without driving it. Mass sensing experiments [13] can be performed with a significantly faster time resolution.

In summary, we have performed high-frequency mixing of a CNT mechanical resonator using a close-proximity high-impedance HEMT amplifier. The CNT-HEMT system has a bandwidth of 62 MHz. We show a mechanical resonance at a $\Delta\omega/2\pi$ of 6 MHz and a timeconstant of 780 ns, up to five orders of magnitudes faster than reported previously, allowing the determination of the CNT's resonance frequency with millisecond time resolution. The transient response of the mechanical signal gives an upper bound to the room-temperature quality factor due to energy relaxation of $Q < 490$.

Acknowledgements: We would like to thank Raymond Schouten for help on the PCB design, Ben Schneider for assistance on fabrication, and Vibhor Singh for fruitful discussions. We acknowledge the financial support of the Future and Emerging Technologies programme of the European Commission, under the FET-Open project QNEMS (233992).

7.5 APPENDIX: PRACTICAL CONSIDERATIONS

This section deals with the practical considerations of the high-bandwidth readout scheme using a close-proximity, high-impedance amplifier. We start with describing our custom design for the printed circuit board, which is used to get the amplifier as close as possible to the device and minimize the readout capacitance. Then, we discuss the fabrication of local-gate devices, which have the goal of minimizing the crosstalk capacitance between the gate and source, and the gate and drain.

7.5.1 PRINTED CIRCUIT BOARD DESIGN

The custom high-bandwidth printed-circuit board (PCB) is shown as a topview in Fig. 7.6a. It consists of four conducting layers of copper interspersed with an insulator made of a material called prepreg, shown as a sideview in Figure 7.6b. The conducting layers are patterned and, at some places, are connected all four at once through vias. Before going into detail, the layers can be described briefly as follows. The top layer contains the CNT sample, the dc connections and the ac drive connections. The second layer is a ground layer, while the third layer holds both the ac drive and readout lines. The bottom layer holds the HEMT amplifier readout stage.

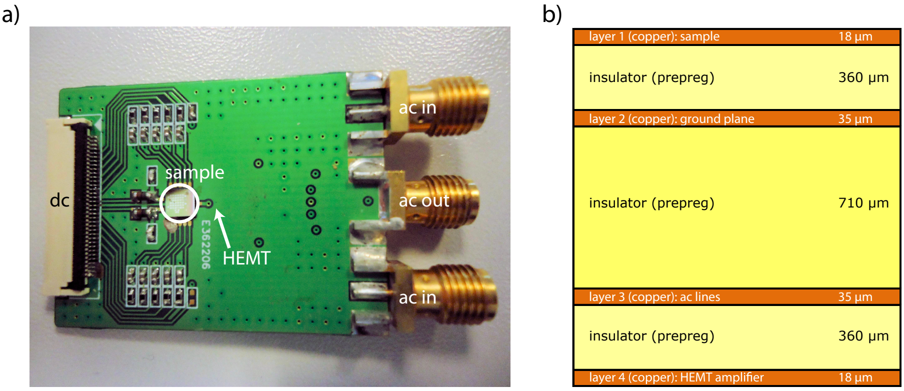

FIGURE 7.6: The custom-designed high-bandwidth printed circuit board, as a) a topview, showing the sample at millimeters from the gate of the HEMT, a dc connector, and three ac connectors, and b) a sideview, showing 4 copper layers containing the sample, a ground plane, the ac lines, and the HEMT amplifier, interspersed with prepreg insulating layers.

We start the detailed description of the PCB with the CNT sample, which can be glued upon a 3 by 3 mm insulating square on the top layer, shown in Figure 7.7. The insulating square is surrounded by thirteen gold bondpads, of which ten for dc connections, two for ac drive, and one for ac readout, that can be connected to the sample through wire-bonds. The dc connections are low-pass filtered through a 10kΩ resistor in series and a 470 pF shunt capacitor to ground, and can be connected to an outside ribbon cable through a 35-pin flexible printed circuitboard (FPC) connector. The two ac drive bondpads are connected to 5.6 kΩ, 100 pF bias-tees, where the dc part goes to the FPC connector and the ac part goes to the third PCB layer through a via. The ac readout bondpad is connected straight away to the readout stage on the bottom PCB layer through a via. This is important to minimize the capacitance to ground and to the drive in order to avoid leakage of the signal and crosstalk, respectively.

The second PCB layer, shown in Figure 7.8, consists of a single ground plane, except for the locations where the vias make connections between the different layers. This ground plane shields the ac readout bondpad on the top layer from the drive signal, minimizing crosstalk.

Figure 7.9 illustrates the third PCB layer, holding the drive and the readout signals as they pass through the PCB. To minimize reflections, the lines are designed with a characteristic impedance of 50 Ω. For simplicity, a model for a wide, off-center stripline is chosen for the design of the lines, instead of a coplanar waveguide. This means that the distances between the center line on the one hand and the top and bottom ground planes on the other hand are unequal, comparable to the width of the stripline, and small compared to the distance to the same-layer ground plane [24]. From the PCB specifications, shown in Figure 7.6b, and a relative dielectric constant of the prepreg of 4, a center line width of 430 μm is found to arrive at a characteristic impedance of 50 Ω. Vias connect the drive and readout lines to three sma launchers at the side of the top or bottom layer of the PCB, which can be accessed with sma coaxial cables. To minimize crosstalk, the top layer holds the drive signal center line and the bottom layer the readout signal center line.

Figure 7.10 shows the readout stage of the PCB, containing an Avago ATF-35143 HEMT amplifier. It is located on the bottom PCB layer, to separate readout and drive as much as possible. The gate of the HEMT amplifier is connected to the ac readout bondpad on the top layer through a via, and grounded through the 5.6 kΩ readout resistor. The current flowing through the CNT and the readout resistor, containing the mechanical signal, changes the voltage on the gate of the HEMT amplifier, modulating its conductance. The source of the HEMT amplifier is ac grounded through six 100 pF and two 47 nF capacitors. By using several capacitors instead of a single one, the accompanying inductance is reduced. At dc, the source of the HEMT amplifier is grounded through a tunable resistor outside of the PCB, through the FPC connector. The drain of the HEMT amplifier is connected through a via, the third layer strip line, and another via to the readout sma launcher. Outside of the PCB, a bias-tee separates the dc and ac components connected to the drain of the HEMT amplifier.

Tuning of the HEMT amplifier occurs in a somewhat unconventional way. Traditionally, the channel of a transistor-based amplifier is pinched off by applying a voltage to its gate. In our system, the gate of the HEMT amplifier is connected to the drain of the CNT device, making it inconvenient to apply more than ∼100 mV, while avoiding damage to the device. To overcome this, the voltage difference between the gate and the source of the HEMT amplifier, needed to pinch off the channel, has to be generated by applying a voltage to the drain of the HEMT amplifier. The setpoint of the HEMT amplifier for optimal gain can be found by tuning the voltage applied to the drain, V_{dd}, and the tunable resistor R_{tune} grounding the source. The voltage oscillations at the gate of the HEMT amplifier by the mechanical signal, modulates the conductance of the HEMT amplifier channel. The ac signal due to this modulation leaves the drain of the HEMT through the bias-tee outside of the PCB and can be post-amplified and then measured with a lock-in amplifier or a spectrum analyser.

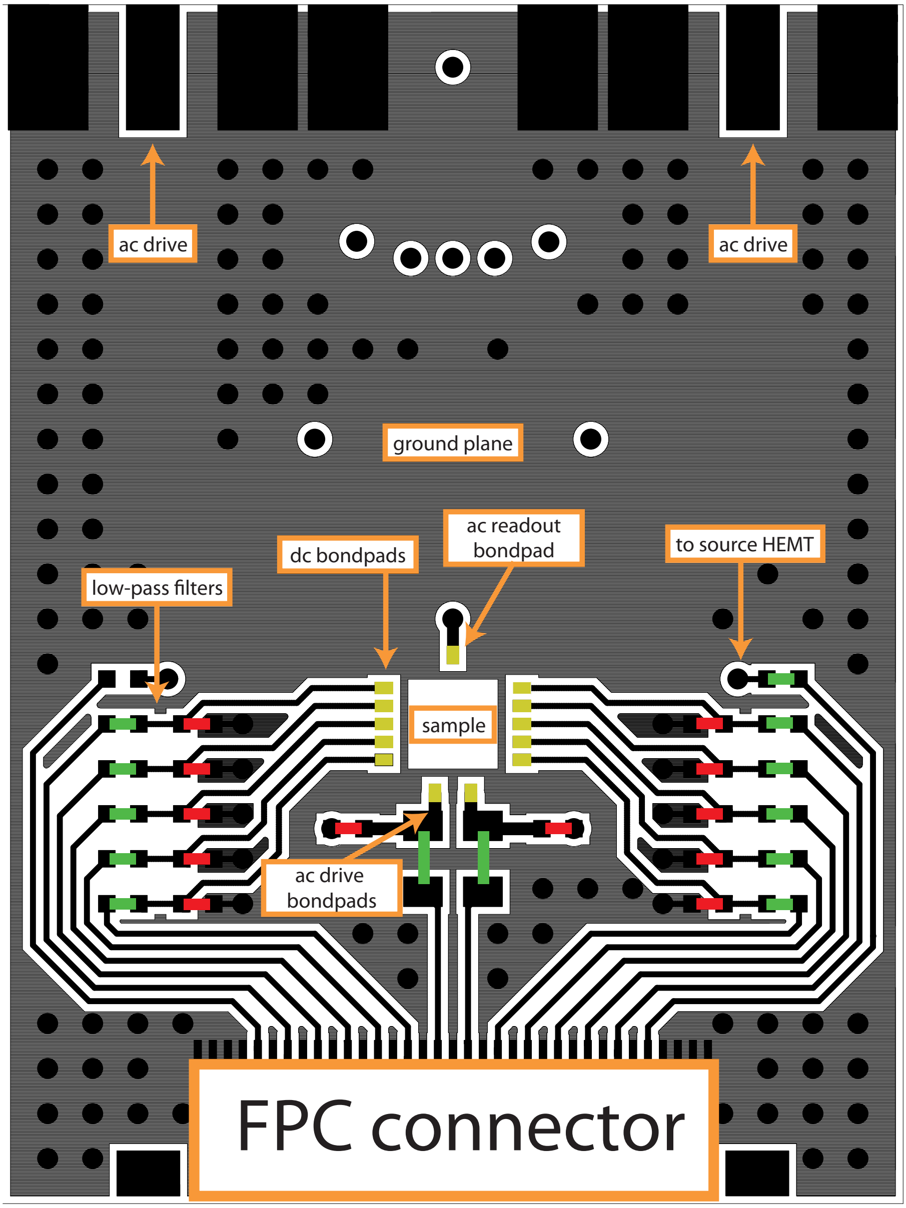

FIGURE 7.7: Layer 1 of the 4-layer printed circuit board of 3 cm by 3.9 cm, containing the sample. Everything that is black or grey is connected. White is absence of a conductor. Filled circles are vias, connecting all four layers. Green blocks are resistors, red blocks are capacitors, and gold blocks are bondpads. A detailed description can be found in the text.

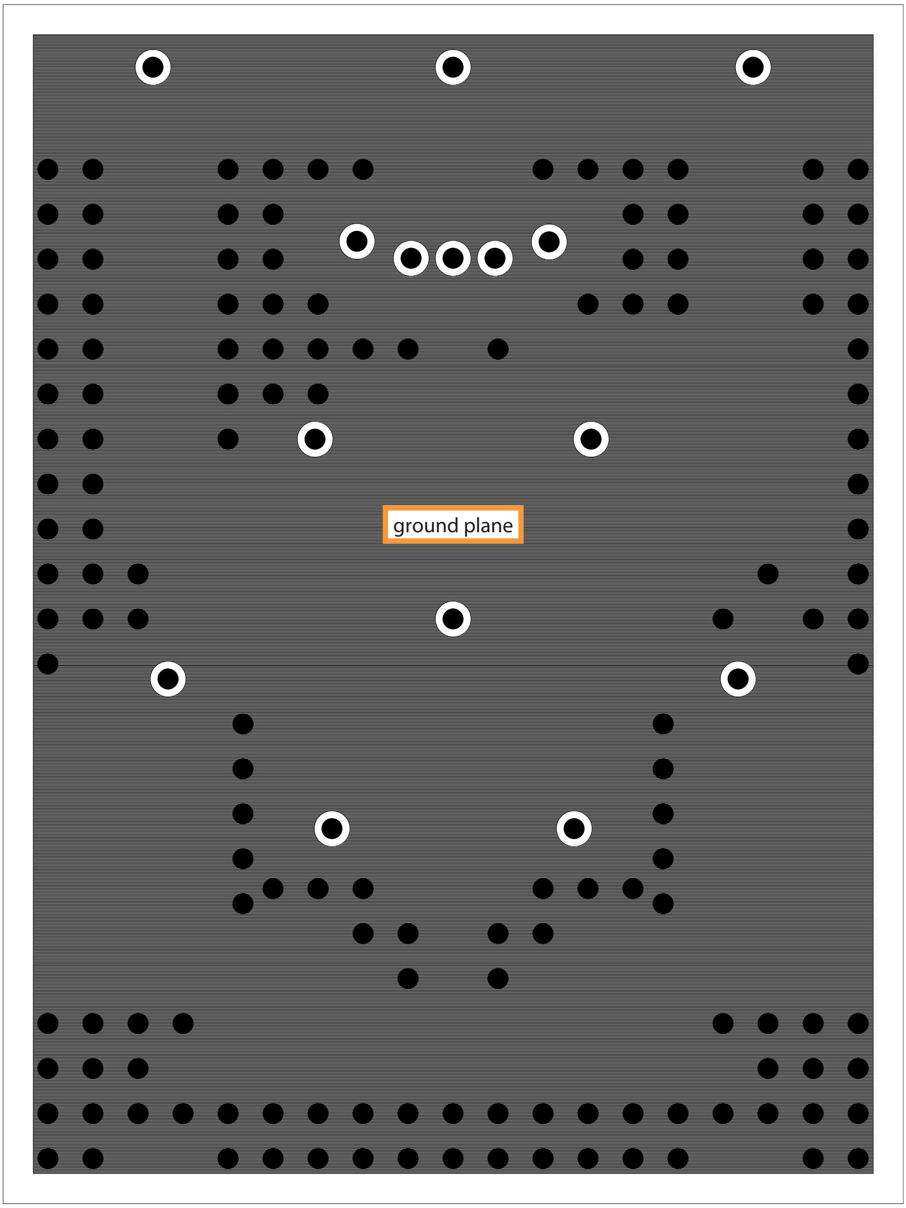

FIGURE 7.8: Layer 2 of the 4-layer printed circuit board, containing a ground plane. A detailed description can be found in the text.

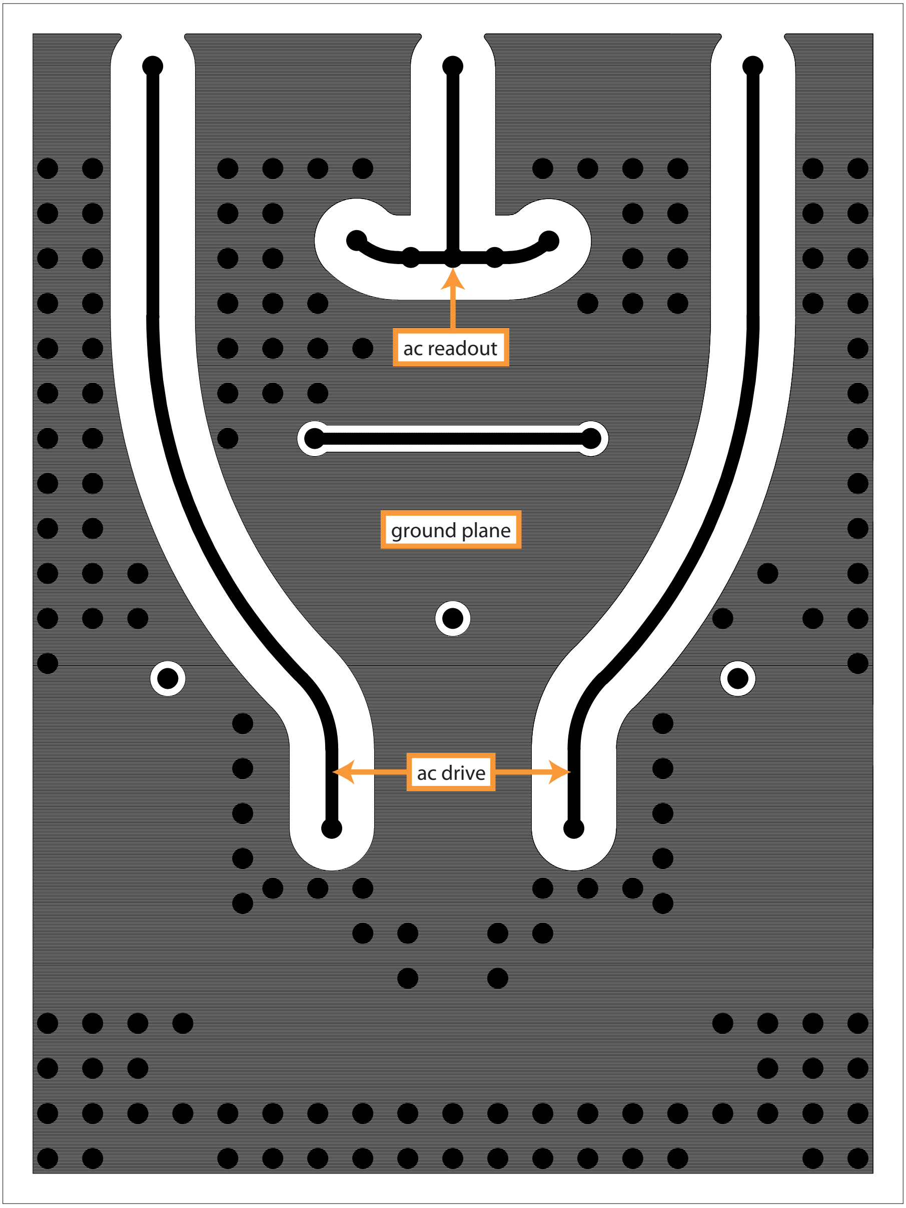

FIGURE 7.9: Layer 3 of the 4-layer printed circuit board, containing the ac lines. A detailed description can be found in the text.

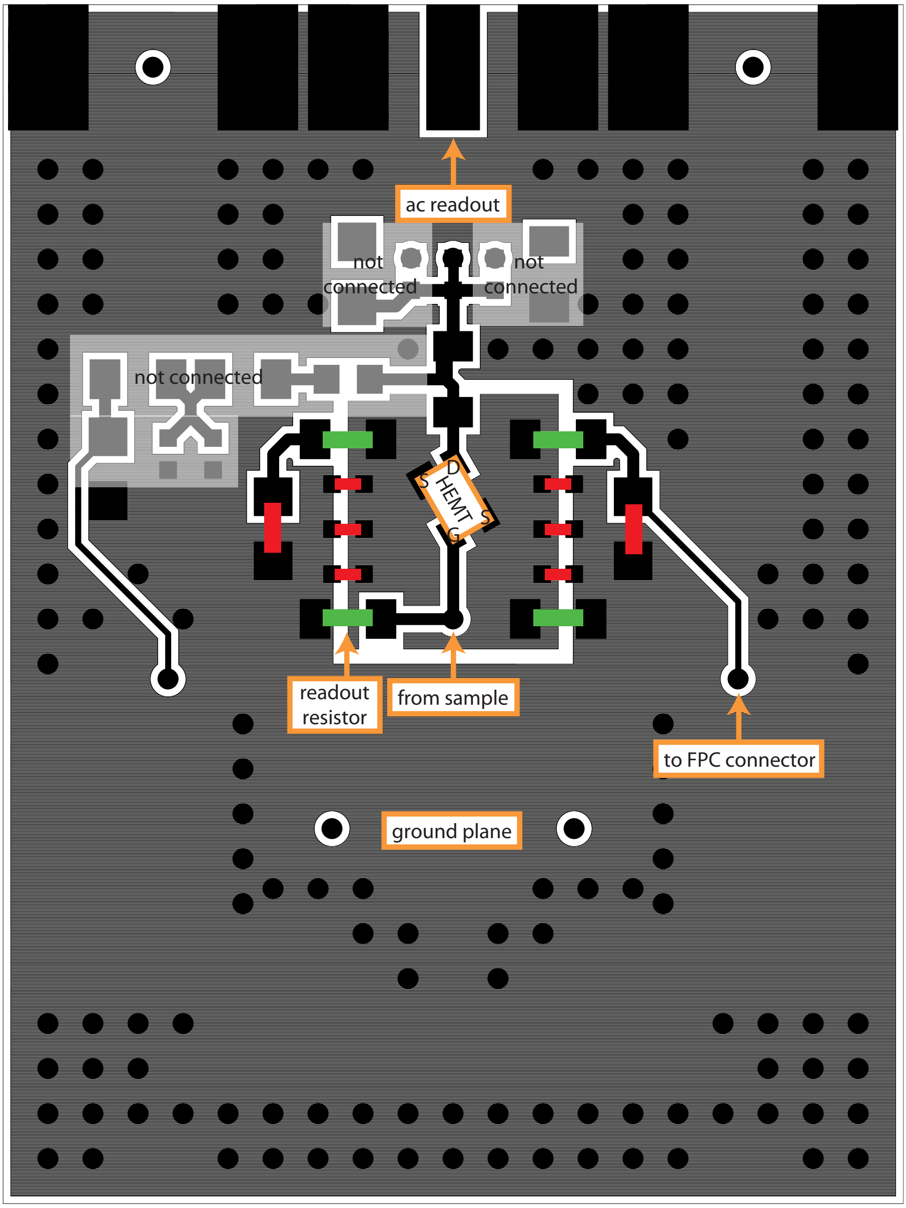

FIGURE 7.10: Layer 4 of the 4-layer printed circuit board, containing the HEMT amplifier with its gate (G), source (S) and drain (D). The two sources are connected underneath the HEMT amplifier. A detailed description can be found in the text.

7.5.2 FABRICATION OF LOCAL-GATE DEVICES

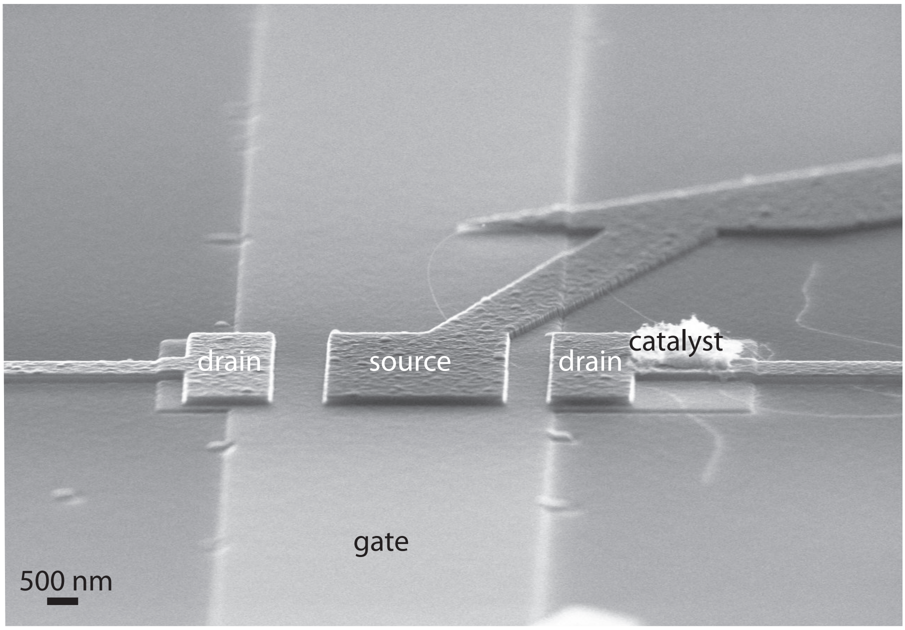

FIGURE 7.11: Scanning electron micrograph of a local-gate CNT device, showing the local gate, the source, two drains, and the catalyst.

To minimize the capacitance between the gate and source electrodes, and the gate and drain electrodes, CNT devices with a local gate have been fabricated. Figure 7.11 shows a scanning electron micrograph of the resulting device. The fabrication process can be divided into four patterning steps: for the local gates, the electrodes, the bondpads, and the CNT catalyst sites.

The fabrication process, depicted in Figure 7.12, starts with an intrinsic silicon wafer covered with 200 nm of thermal oxide. Intrinsic silicon is chosen because of its high resistivity, minimizing its capacitance to the source and drain. However, at room temperature it is still conducting. A 50 nm layer of tungsten is sputtered onto the thermal oxide, that serves as the local gate. After electron beam lithography on spin-coated NEB22, a negative electron beam resist, the local-gates structure is patterned onto the tungsten with a reactive ion etch of SF_6/He, with the NEB22 acting as an etch mask. Subsequently, the tungsten local gate is buried under a 200 nm layer of PECVD (plasma enhanced chemical vapour deposition) silicon oxide, followed by a sputtered layer of 35 nm of rhenium and 35 nm of molybdenum, which act as the electrodes.

The second patterning step involves defining electrodes and trenches in the underlying PECVD silicon oxide, in order to have suspended CNTs in the end. For this, a four-layer etch mask is used, consisting of PMMA on the bottom, then S1813, tungsten, and NEB22 on top. The main reason for this elaborate etch mask is to use the optical resist S1813, since that has a sufficiently high etch selectivity against MoRe and silicon oxide. However, electron beam lithography cannot be used to pattern the optical resist, hence a layer of tungsten and NEB22 is put on top. Furthermore, the standard way to remove S1813 is with nitric acid, but this affects the MoRe. To resolve this issue, a layer of PMMA is put on before the S1813, which then allows the removal of the S1813 with lift-off in acetone. The dry etching of the trenches is performed as follows. After the NEB22 has been patterned with electron beam lithography, a combination of SF_6 and helium plasma is used to etch through the tungsten. Next, oxygen plasma is used to etch through the S1813 and PMMA, followed by again an SF_6/He etch of the MoRe and the silicon oxide. A trench of ~150 nm is now created between two MoRe electrodes. This permits a layer of ~50 nm of silicon oxide to cover the tungsten local gates and prevent electrical shorts between the gate and the electrodes through stray CNTs.

At this point, the local gates are buried underneath PECVD silicon oxide. In the third patterning step, the previously patterned bondpads for the local gates are accessed. To achieve this, electron-beam patterned PMMA is used as an etch mask, after which buffered HF is used to remove the silicon oxide and uncover the local-gate bondpads. To improve wire-bonding, 5 nm of chromium and 25 nm of platinum is evaporated on the local-gate bondpads, followed by a 10 nm layer of sputtered silicon. After this, lift-off is performed.

In the final patterning step, the CNT catalyst sites are patterned into PMMA. The catalyst particles, which are dissolved in methanol, are deposited on the sample, remaining on the specified sites after lift-off of the PMMA. Using a quartz tube oven, CNTs grow out of the catalyst particles at a temperature of 900 °C in a mixture of hydrogen and methane. The CNTs grow in random directions, with a probability of ~30% of crossing a trench and forming a device.

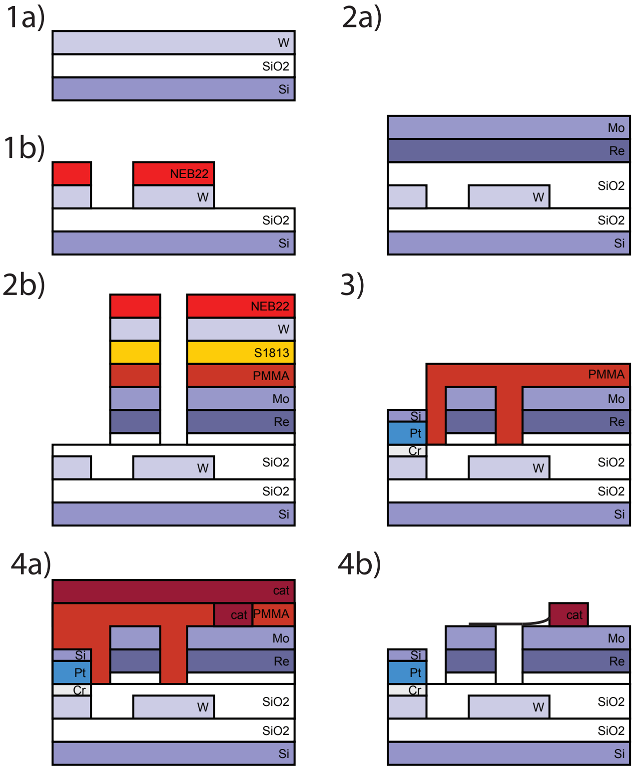

FIGURE 7.12: Fabrication of local-gate CNT devices in four patterning steps: 1a) An intrinsic silicon substrate with thermal SiO_2 is sputtered with tungsten. 1b) The tungsten local gates are patterned with electron beam lithography, with NEB as resist. 2a) The local gates are buried in PECVD SiO_2, after which rhenium and molybdenum are sputtered. 2b) The MoRe electrodes and the trench are patterned using a 4-layer etch mask. 3) The local gates are contacted with BHF wet-etching, evaporated with chromium and platinum, and sputtered with silicon. 4a) Catalyst is drop-cast on electron-beam patterned PMMA resist, after which lift-off is performed. 4b) The final device, after CNT growth.

REFERENCES

[1] V. Sazonova, Y. Yaish, H. Ustunel, D. Roundy, T. A. Arias, and P. L. McEuen, *A tunable carbon nanotube electromechanical oscillator*, Nature **431**, 284 (2004).

[2] H. B. Peng, C. W. Chang, S. Aloni, T. D. Yuzvinsky, and A. Zettl, *Ultrahigh frequency nanotube resonators.*, Physical Review Letters **97**, 087203 (2006).

[3] B. Witkamp, M. Poot, and H. S. J. van der Zant, *Bending-mode vibration of a suspended nanotube resonator*, Nano Letters **6**, 2904 (2006).

[4] A. W. Barnard, V. Sazonova, A. M. van der Zande, and P. L. McEuen, *Fluctuation broadening in carbon nanotube resonators*, Proceedings of the National Academy of Sciences **109**, 19093 (2012).

[5] J. S. Aldridge and A. N. Cleland, *Noise-enabled precision measurements of a Duffing nanomechanical resonator*, Physical Review Letters **94**, 156403 (2005).

[6] C. Stambaugh and H. B. Chan, *Noise-activated switching in a driven nonlinear micromechanical oscillator*, Physical Review B **73**, 172302 (2006).

[7] Q. P. Unterreithmeier, T. Faust, and J. P. Kotthaus, *Nonlinear switching dynamics in a nanomechanical resonator*, Physical Review B **81**, 241405 (2010).

[8] V. Peano and M. Thorwart, *Nonlinear response of a driven vibrating nanobeam in the quantum regime*, New Journal of Physics **8**, 21 (2006).

[9] M. I. Dykman and V. N. Smelyansky, *Quantum-Theory Of Transitions Between Stable States Of A Nonlinear Oscillator Interacting With The Medium In A Resonant Field*, Zhurnal Eksperimentalnoi I Teoreticheskoi Fiziki **94**, 61 (1988), URL `http://bitly.com/WUhZrh`.

[10] I. Serban and F. K. Wilhelm, *Dynamical tunneling in macroscopic systems*, Physical Review Letters **99**, 137001 (2007).

[11] M. Marthaler and M. I. Dykman, *Switching via quantum activation: A parametrically modulated oscillator*, Physical Review A **73**, 042108 (2006).

[12] I. Katz, A. Retzker, R. Straub, and R. Lifshitz, *Signatures for a classical to quantum transition of a driven nonlinear nanomechanical resonator*, Physical Review Letters **99**, 40404 (2007).

[13] J. Chaste, A. Eichler, J. Moser, G. Ceballos, R. Rurali, and A. Bachtold, *A nanomechanical mass sensor with yoctogram resolution*, Nature Nanotechnology **7**, 301 (2012).

[14] A. N. Cleland and M. L. Roukes, *Noise processes in nanomechanical resonators*, Journal of Applied Physics **92**, 2758 (2002).

[15] A. D. O'Connell, M. Hofheinz, M. Ansmann, R. C. Bialczak, M. Lenander, E. Lucero, M. Neeley, D. Sank, H. Wang, M. Weides, et al., *Quantum ground state and single-phonon control of a mechanical resonator*, Nature **464**, 697 (2010).

[16] J. D. Teufel, T. Donner, D. Li, J. W. Harlow, M. S. Allman, K. Cicak, A. J. Sirois, J. D. Whittaker, K. W. Lehnert, and R. W. Simmonds, *Sideband cooling of micromechanical motion to the quantum ground state*, Nature **475**, 359 (2011).

[17] J. Chan, T. P. Mayer Alegre, A. H. Safavi-Naeini, J. T. Hill, A. Krause, S. Groeblacher, M. Aspelmeyer, and O. Painter, *Laser cooling of a nanomechanical oscillator into its quantum ground state*, Nature **478**, 89 (2011).

[18] X. L. Feng, C. J. White, A. Hajimiri, and M. L. Roukes, *A self-sustaining ultrahigh-frequency nanoelectromechanical oscillator*, Nature Nanotechnology **3**, 342 (2008).

[19] O. Usmani, Y. M. Blanter, and Y. V. Nazarov, *Strong feedback and current noise in nanoelectromechanical systems*, Physical Review B **75**, 195312 (2007).

[20] Y. Xu, C. Chen, V. V. Deshpande, F. A. DiRenno, A. Gondarenko, D. B. Heinz, S. Liu, P. Kim, and J. Hone, *Radio frequency electrical transduction of graphene mechanical resonators*, Applied Physics Letters **97**, 243111 (2010).

[21] T. S. Abhilash, J. P. Mathew, S. Sengupta, M. Gokhale, A. Bhattacharya, and M. M. Deshmukh, *Wide Bandwidth Nanowire Electromechanics on Insulating Substrates at Room Temperature*, Nano Letters **12**, 6432 (2012).

[22] Q. P. Unterreithmeier, T. Faust, and J. P. Kotthaus, *Damping of nanomechanical resonators*, Physical Review Letters **105**, 27205 (2010).

[23] S. Stapfner, L. Ost, D. Hunger, E. M. Weig, J. Reichel, and I. Favero, *Cavity-enhanced optical detection of carbon nanotube Brownian motion* (2012), URL `http://arxiv.org/abs/1211.1608`.

[24] B. Wadell, *Transmission line design handbook* (Artech House Boston (Ma), 1991).

SUMMARY

In this Thesis, carbon nanotubes (CNTs) are studied as electromechanical resonators. It is shown experimentally and theoretically that their mechanical motion couples strongly to single-electron tunneling, as CNTs become quantum dots at cryogenic temperatures. Also, because of their high aspect ratio, CNTs can easily be perturbed into the nonlinear regime. To read out their mechanical motion at high frequencies, a novel high-bandwidth readout scheme is developed and discussed.

Chapter 1 gives an introduction to the theoretical background needed to describe a CNT as a quantum dot resonator. First, the model of a damped driven harmonic oscillator is discussed to describe a resonator. Second, the phenomena of single-electron tunneling and quantum dots are introduced. Third, properties that are specific to CNT electromechanical resonators are laid out, i.e. a low mass density, a high Young's modulus, a high aspect ratio, a large change in capacitance with displacement, and a large tensile strength. The Chapter ends with an overview of experiments in CNT resonators, related to strong electron-vibron coupling, damping, and nonlinearity.

Chapter 2 describes several detection methods that have been used for reading out the mechanical motion of a carbon nanotube. Because of its small cross-section, it is difficult (but not impossible) to detect a CNT with optical methods. Microscopy methods include the imaging of the CNT's motion with an atomic force microscope, a transmission electron microscope and through the use of field electron emission. Electrical methods include mechanically mixing and rectifying the current through the CNT, and the use of a superconducting quantum interference device. The different components to the mechanically and electrically induced currents are discussed in depth.

The strong electron-vibron coupling, which couples the CNT's mechanical motion to the electrons tunneling through it, can be explained by looking at the average charge on the CNT quantum dot. As the CNT resonates, the average charge is mechanically modulated, leading to a single-electron force. **Chapter 3** shows experimentally how this anti-restoring, out-of-phase, and displacement-dependent single-electron force leads to resonance frequency dips, damping, and nonlinearity, respectively. Also, in the regime when the average charge decreases while approaching the gate electrode, single-electron tunneling is shown to excite the CNT resonator into motion without external excitation.

In **Chapter 4**, a quantitative model is established and compared to experiments, verifying mechanical modulation of the average charge as the cause for spring softening and damping. At high bias voltage, this leads to a double dip in frequency and quality factor as a function of gate voltage. Although more electrons tunnel at high bias voltages, damping is explained to decrease. In a theoretical description, the change in average charge with gate voltage also accounts for single-electron Duffing nonlinearity, and single-electron mode coupling. By tuning the tunnel barriers through magnetic field, the average charge can experimentally be made to increase more sharply with gate voltage, causing larger frequency dips and increased damping. An electronic excited state leads to an increase in the average charge, and is shown experimentally to cause a frequency dip. In the Fabry-Pérot regime, the average charge increases smoothly, and no spring softening is visible.

Chapter 5 deals with coupling between different modes of the CNT quantum dot resonator through the single-electron force. By driving the CNT around two resonance frequencies at the same time, shifts of one resonance frequency because of increased amplitude from the other resonance is discerned. Within several millivolts of gate voltage, the single-electron force leads to mode-coupling-induced spring softening, spring stiffening or the suppression of modal interaction. The tunability of one mode with the other is found to be ~60 $\mathrm{kHz/nm^2}$, which is six orders of magnitude larger than that in micromechanical beams.

Chapter 6 gives a theoretical description of different types of nonlinearity that occur in CNT resonators. Geometric nonlinearity comes about as the length of the resonator increases at high amplitudes, capacitive nonlinearity arises from the proximity of a (gate) electrode, and single-electron nonlinearity occurs when the CNT becomes a quantum dot at cryogenic temperatures. Because of the large tunability of the resonance frequency with gate voltage, CNTs are shown to be excellent subjects for parametric actuation. Also, tension-induced mode coupling in CNT resonators is discussed.

Because of their high resistance, CNT resonators are difficult to read out at high frequencies. For this reason, down-mixing and rectification have been used until now. **Chapter 7** describes the use of a close-proximity high-impedance HEMT amplifier for high-bandwidth readout. With this technique, high-frequency mixing was performed at a frequency of 6 MHz, 3 orders of magnitude faster than previously. The time-constant for these measurements is as low as 780 ns, 5 orders of magnitude faster than before. Using the decay of the electrical mixing current passing through the CNT, energy relaxation of the mechanical motion could be determined to have an upper bound of $Q = 490$ at room temperature.

SAMENVATTING

In dit proefschrift worden koolstof nanobuizen (KNBs) bestudeerd in de vorm van electromechanische resonatoren. Het wordt experimenteel en theoretisch aangetoond dat hun mechanische beweging sterke interactie vertoond met het tunnelen van enkele elektronen, wanneer KNBs quantum dots worden bij cryogene temperaturen. Bovendien kunnen KNBs eenvoudig aangeslagen worden naar het nonlineaire regime vanwege hun hoge lengte-breedteverhouding. Om hun mechanische beweging uit te lezen is er een nieuwe breedbandige uitleesmethode ontwikkeld en behandeld.

Hoofdstuk 1 geeft een inleiding van de theoretische achtergrond die nodig is om een KNB te beschrijven als een quantum dot resonator. Allereerst wordt het model van een gedempte aangedreven harmonische oscillator behandeld om een resonator te beschrijven. Als tweede wordt het verschijnsel van het tunnelen van enkele elektronen en dat van quantum dots geïntroduceerd. Ten derde worden eigenschappen die in het bijzonder voor KNBs gelden behandeld. Het Hoofdstuk eindigt met een overzicht van experimenten naar KNB resonatoren, gerelateerd aan sterke elektron-vibroninteractie, demping en nonlineariteit.

Hoofdstuk 2 beschrijft verschillende detectiemethoden die zijn gebruikt om de mechanische beweging van een koolstof nanobuis uit te lezen. Vanwege zijn kleine doorsnede is het moeilijk (maar niet onmogelijk) om de KNB te detecteren met optische methoden. Onder microscopiemethoden vallen het in beeld brengen van de beweging van de KNB met een atoomkrachtmicroscoop, een transmissie-elektronenmicroscoop en door het uitzenden van elektronen. Elektrische methoden zijn o.a. het mechanisch mixen en rectificeren van de stroom die door de KNB loopt en het gebruik van een supergeleidend quantum interferentie device. De verschillende bijdragen aan de mechanisch en elektrisch opgewekte stromen worden uitgebreid besproken.

De sterke elektron-vibroninteractie, die de mechanische beweging van de KNB in interactie brengt met de elektronen die erdoorheen tunnelen, kan worden uitgelegd aan de hand van de gemiddelde lading op de KNB quantum dot. Wanneer de KNB resoneert, wordt de gemiddelde lading mechanisch gemoduleerd, wat leidt tot een enkele-elektronkracht. **Hoofdstuk 3** laat experimenteel zien hoe deze anti-herstellende, tegenfasige en uitwijkingsafhankelijke enkele-elektronkracht leidt tot dips in de resonantiefrequentie, tot demping en tot nonlineariteit, respectievelijk.

Bovendien wordt getoond hoe het tunnelen van enkele elektronen kan leiden tot beweging van de KNB zonder externe aandrijving.

In **Hoofdstuk 4** wordt een kwantitatief model opgezet en vergeleken met experimenten, wat bewijst dat de mechanische modulatie van de gemiddelde lading de oorzaak is van veerverzachting en demping. Bij een hoge voorkeursspanning leidt dit tot een dubbele dip in frequentie en kwaliteitsfactor als functie van poortspanning. Gebruik makend van een theoretische beschrijving zorgt de verandering in de gemiddelde lading met poortspanning ook voor enkele-elektron nonlineariteit en enkele-elektron modusinteractie. Door de tunnelbarrières te veranderen met behulp van een magnetisch veld wordt de gemiddelde lading experimenteel scherper met poortspanning vergroot, wat leidt tot grotere frequentiedips en een toename in de demping. Een elektronische aangeslagen toestand leidt ook tot een frequentiedip. In het Fabry-Pérot regime neemt de gemiddelde lading gestaag toe en is er geen veerverzachting zichtbaar.

Hoofdstuk 5 gaat over de interactie tussen verschillende modi van de KNB quantum dot resonator vanwege de enkele-elektronkracht. Door de KNB tegelijkertijd rond twee resonantiefrequenties aan te drijven wordt een verschuiving van de resonantiefrequentie van de ene modus waargenomen vanwege de toegenomen amplitude van de andere resonantie. Binnen enkele millivolts van poortspanning leidt de enkele-elektronkracht tot veerverzachting en veerverharding vanwege modusinteractie en ook tot de onderdrukking van modusinteractie. De verandering in de resonantiefrequentie van een modus door de andere modus is bepaald op ca. 60 kHz/nm^2, zes ordegroottes groter dan micromechanische balken.

Hoofdstuk 6 geeft een theoretische omschrijving van verschillende typen nonlineariteit die voorkomen in KNB resonatoren. Geometrische nonlineariteit vindt plaats doordat de lengte van de resonator toeneemt bij hoge amplitude, capacitieve nonlineariteit komt voort uit de nabijheid van een (poort)elektrode en enkele-elektron nonlineariteit komt voor wanneer de KNB een quantum dot wordt bij lage temperaturen. Vanwege de grote verandering van de resonantiefrequentie met poortspanning wordt het aangetoond dat KNBs uitstekende onderwerpen zijn voor parametrische aandrijving. Ook wordt modusinteractie in KNB resonatoren vanwege trekspanning behandeld.

Vanwege hun hoge weerstand is het moeilijk KNB resonatoren uit te lezen bij hoge frequenties. **Hoofdstuk 7** beschrijft het gebruik van een nabije HEMT-versterker met een hoge weerstand om breedbandig uit te lezen. Met deze techniek is hoogfrequent mixen uitgevoerd bij een frequentie van 6 MHz, drie ordegroottes sneller dan voorheen. De tijdsconstante voor deze metingen is zo laag als 780 ns, vijf ordegroottes sneller dan voorheen. Door de afname van de elektrische mixstroom door de KNB te meten, kon worden bepaald dat de energieafname van de mechanische beweging een bovengrens van $Q = 490$ heeft bij kamertemperatuur.

Curriculum Vitæ

Harold Boudewijn Meerwaldt

19-05-1983	Born in Vlaardingen, the Netherlands
1995–2001	Secondary School (VWO) Stedelijk Gymnasium "Johan van Oldenbarnevelt", Amersfoort
2001–2007	Doctoraal (MSc.) Physics and Astronomy Utrecht University *Thesis:* Time reversal non-invariance in stochastic theories: Can GRW explain the irreversibility of macroscopic physics? *Supervisor:* Prof. Dr. J. B. M. Uffink
2005	Intern (3 months) Renewable Energy Systems Fraunhofer Institut SI, Karlsruhe, Germany
2007	Tutor (5 months) of English conversational skills La Universidad de Guadalajara, Guadalajara, Mexico
2007–2008	Researcher Hydrogen Transition and Infrastructure Energy research Centre of the Netherlands (ECN), Petten
2008–2009	Courses MSc Applied Physics, Track: Nanoscience Delft University of Technology
2009–2013	PhD Applied Physics Delft University of Technology *Thesis:* Carbon nanotubes as electromechanical resonators: single-electron tunneling, nonlinearity, and high-bandwidth readout *Promotor:* Prof. Dr. Ir. H. S. J. van der Zant *Copromotor:* Dr. G. A. Steele

LIST OF PUBLICATIONS

arXiv: `http://bitly.com/V4kTX9`
Google Scholar: `http://bitly.com/W43wsm`

7. H. B. Meerwaldt, S. R. Johnston, H. S. J. van der Zant, and G. A. Steele
Submicrosecond-timescale readout of carbon nanotube mechanical motion
In preparation

6. G. A. Steele, F. Pei, E. A. Laird, J. M. Jol, H. B. Meerwaldt, and L. P. Kouwenhoven
Large spin-orbit coupling in carbon nanotubes
Accepted in Nat. Comm.

5. H. B. Meerwaldt, G. Labadze, B. H. Schneider, A. Taspinar, H. S. J. van der Zant, and G. A. Steele
Probing the charge of a quantum dot with a nanomechanical resonator
Phys. Rev. B **86**, 115454 (2012)
Editor's Suggestion

4. A. Castellanos-Gomez, H. B. Meerwaldt, W. J. Venstra, H. S. J. van der Zant, and G. A. Steele
Strong and tunable mode coupling in carbon nanotube resonators
Phys. Rev. B **86**, 041402 (2012)
Editor's Suggestion

3. H. B. Meerwaldt, G. A. Steele, and H. S. J. van der Zant
Carbon nanotubes: Nonlinear high-Q resonators with strong coupling to single-electron tunneling
Book chapter in "Fluctuating nonlinear oscillators" (Oxford University Press, 2012).

2. A. K. Hüttel, H. B. Meerwaldt, G. A. Steele, M. Poot, B. Witkamp, L. P. Kouwenhoven, H. S. J. van der Zant
Single electron tunnelling through high-Q single-wall carbon nanotube NEMS resonators
Phys. Stat. Sol. (b) **247**, 2974–2979 (2010)

1. G. A. Steele, A. K. Hüttel, B. Witkamp, M. Poot, H. B. Meerwaldt, L. P. Kouwenhoven, and H. S. J. van der Zant
Strong coupling between single-electron tunneling and nanomechanical motion
Science **325**, 1103–1107 (2009)

ACKNOWLEDGEMENTS

Delft $\neq$ Utrecht. I won't go into the differences in the rich social and cultural life between the two cities (ahem...), but I'll tell a bit about my time studying in Utrecht before I came here. During my Bachelor's, after a couple of cookbook-style "experiments" in my first years, I decided that experimental physics was not for me. I found it frustrating and not very challenging or creative. I didn't know what to do, so I switched direction every single year: I did astrophysics, theoretical physics, computational physics, innovation management, teaching, and finally ended up with a master thesis in foundations of quantum mechanics. After getting my doctorandus' (no not ingenieur's!) degree, I spent a couple of months researching the infrastructure for hydrogen cars, but for some strange reason experimental physics started to appeal to me again. I went to Delft and did half a year of Applied Physics courses in the Nanoscience track.

It was then when I met Herre. Impressed by his easy style of teaching in the Mesoscopic Physics course, I decided to do a master's project at the Molecular Electronics and Devices group. Herre, I remember our meeting to discuss this (you definitively did not like it that I called you "u"!); you suggested carbon nanotubes, and I, having no idea whatsoever, agreed. As I became increasingly less stubborn over the years, I have learned/am learning a lot from you: how to write so that people actually understand what I mean (with sentences that should be a lot shorter than this one), how to come to the essence of what is important (in my research), and of course, how to work in parallel and focus at the same time. Although daily supervision moved away from you as the years passed, I really appreciate you keeping an eye out to my progress and development. Sincerely thank you.

During my master's project, I was supervised by Benoit. You introduced me to something in LabView that is supposed to be a program, and to practical stuff I hadn't done in years, such as soldering and using a wrench. I really admire your hands-on mentality.

Since I already had a degree, the master's project was soon upgraded to doing a PhD. I became a full part of the group and shared an office with Ferry. We enjoyed your music a lot and I remember asking for the name of the bands you were playing and then forgetting and asking again. Another great presence in the group was of course Edgar. Playing tennis with you meant being prepared, at all times, especially when I thought I had the point, to sprint to the net and return one of your amazing drop shots. At least you were not scaring me with the dessicator...Menno, thanks for all your help, Chapter 6 definitively has plenty of your spirit (oh, by the way, I didn't read the book in the end). There was a nice atmosphere in the group with Anne, Alexander, Abdulaziz, Bo, Gijs and many others.

Slowly, the old gang moved on and we come to the people whom I spent most of my PhD with. Ben! We started together almost at the same time on almost the same subject and we had a lot of international fun because of my European project that you excellently benefited from. Thanks for helping me grow tubes (or as Edgar would say...) Hidde, it was always relaxing to chat with you in the hallway and, indeed, put the science into perspective. Samir, thanks for helping me out at many occasions with cryogenics and dc electronics, and for just being a fun guy to be around. I really enjoyed walking through Paris with you and visiting the 15-minute-15-euros jazz session. Whatever job (postdoc?) you end up getting, I know you'll do great. Venkatesh, us living across from each other meant we've had nice little talks in the street, you either walking towards or from the university, and this could also be Saturday evening or Sunday morning. Now that you have your first couple of articles published, I hope you can relax a bit more. Jos, thank you for allowing me to bug you about single-electron tunneling, thesis-related stuff, and job hunting. I know you'll find a great job, who knows at the same company? Warner, I really admire your enthusiasm, and the couple of spritz's we had in Trieste made for some great conversations.

More than half of my PhD I was supervised by my now-copromotor. Gary, thank you for everything. You have helped me enormously with your crystal-clear vision and your great ideas. It took me some getting used to, going from Herre's Pirates-of-the-Caribbean laissez-faire style of supervision to your more focused style of management (at the nanoscale? ;)), but I think it made all the difference, and I benefited a lot from the combination of you two. Normally, telling a student to "expose himself" is a dubious thing, but I think it was the best advice you have given me. You have a great subgroup, ehm I mean Lab, and I'm sure you'll accomplish your crazy idea of a graphene sheet on a qubit on a cavity. (You can't cross a chasm in two small steps...)

During my PhD, I got help from a lot of people inside and outside the group. Mascha, thank you very much for helping me out with the clogged Frosti, all the pumps, and saving me each time I spent several frustrating hours behind the machine that shall not be named. Ron, thanks for the cheap-and-still-nicely-working feedthrough. Maria, Irma, and Dorine, thank you for distracting the rest of us from physics during breaks, for doing all those orders of mine, and helping me with the defence details. The people from NAF: Emile, Marc, Marco, Anja, Ewan, Arnold, Roel, thanks for keeping the machines working so smoothly. The helium people:

Remco, Bram, yes I'd like my beer warm! The people from the service point and the magazijn: thanks for helping me out; it always feels good to spend Herre's money. The DEMO guys: Jack, Ruud, and especially Rogier, thanks for helping me with the pcb and all the little things I needed. Raymond, thanks for your great help with designing the pcb. I had great bachelor students: Alcuin, Adem, of course Stanley (almost lost my faith in electrons because of you ;)), and Scott (thanks for finding the nice suspended tubes!), and great master students: David (hope you're doing great in Grenoble) and Tatek. The tube people: Fei, Maria, Han, Edward, Gilles, Feng, Rik, thanks for sharing all the recipes and keeping a working oven. And on the theory side: Yaroslav, thanks for your patient explanations, and Giorgi, sometimes it took us some time to translate between the "experiment" and "theory" languages, but we've had great discussions, resulting in Chapter 4, and I very much enjoyed the time we spent across Europe and especially Israel.

There have been many nice people added to the group: An-na (it was great to see your nice Italian spirit come more and more alive, it has been awesome to have you as an office mate), Ben B, Ronald, Max, the "new" PI's: Sander, Andrea, and Peter (great to have you in my committee), Carlos (really envious of your New York adventure!), Enrique, Joshua (what's happening, dude?), Mickael, Riccardo (with your name spelled correctly for the first time after two theses), Katsu (thanks for the nice food and good luck here in Delft), the new guys: Julien and Wiel, and the two guys that have to execute the crazy idea: Vibhor, I really admire your calm, open, and knowledgeable way of working, and Sal, you're slowly finding out that a PhD is a marathon, and not a sprint, but I'm sure you'll keep up your passionate and creative way of looking at things (and if I ever become a CEO, I'll let you know!). And now Andres, what to say about you, you picked a dangerous time to mess with my nice diagrams!!! First of all, thanks for speeding up the mode coupling business, but mainly thanks for your significant contribution to the open and lively atmosphere in the group. And then we come to Michele, or Buscema Buscema, or known to the Dutch people on the phone as Michelle Buskema. I really enjoyed the time I spent with you in the office, listening (and singing) to our huge repertoire of music, consisting of Our house, Skyfall, and the same three songs on Arrow Jazz Smooth Sublime FM. You will get even more work done when I leave! It was great to go to the pool and watch Andres swim twice as fast as us. I will always remember the beers we had in my apartment in the Hague. Thanks, man!

Before I arrive at the end, I want to thank my family and friends. Mom and dad, I am really grateful to know that you are always there to help me. Little sis, great that you're going to be my paranimf, I picked you because I know you can defend me when needed (and Michele too)! Ruub and Sabje, I'm so glad to call you my friends, I don't know what these four years would have been like without you two. Guen, simply thank you. And then I want to thank all the people who unknowingly lured me out of PhD-tunnel-vision now and then with some great, fun times: Marcel, Jeroen, Wendy, Nico, the guys from the band (who knows what our name will be when this gets printed!): Ernst, Bas, Klaus, and Leo, my Clara room mates, and all the people from the Bagijnhof.

My dad always likes to tease me that I should've studied in Delft, not Utrecht, and become a proper ingenieur (as he did, of course). Well, it's turning out to be a Delft PhD and I have to say: I could not be more happy to have done this. Experimental physics is challenging and creative (and of course still frustrating at times). I have learned more things than I could've imagined: cryogenics, nanofabrication, doing experiments, theory, and modeling (bonus points if you thought about a runway here, but no, not that kind of modeling), writing, making figures with thick enough lines, giving presentations, managing my own project, supervising students, and withstanding loud noises for extended periods of time. I'm definitely glad that I ended up in this awesome university with these nice people. And the culture stuff, it only distracts from research, right?

So, after four years of PhD, one question remains...

...

Who is going to write my song?

Harold Meerwaldt
Delft, February 2013